EUROPEAN ORGANIZATION FOR NUCLEAR RESEARCH

HIGH-ENERGY NEUTRINO EXPERIMENTS

F. Dydak

CERN, Geneva, Switzerland

and

Institut für Hochenergiephysik der Universität,
Heidelberg, Germany

Lectures presented at the
17th Internationale Universitätswochen für Kernphysik,
Schladming, Austria, 21 February-3 March 1978

Geneva - 20 April 1978

CONTENTS

1. INTRODUCTION

Neutrino physics has entered a new era with the advent of intense, high-energy neutrino beams, and with the advent of large-scale neutrino detectors. Now neutrino experimentation gets used to large numbers of events, and systematic errors start to dominate statistical ones. Precise experimental results are possible, and they are gradually replacing the less accurate and more qualitative earlier statements. However, faced with the impressive results which have emerged from past neutrino experiments, we can only hope that the forthcoming results, accessible only in high-precision experiments, will be of a similarly incisive character.

In these lectures I have tried to summarize the experimental work in high-energy neutrino scattering. Strong emphasis is put on recent results rather than on earlier ones since these are covered in a number of reviews[1]. The primary aim of these lectures is to present our current physics picture. This is done by discussing selected experimental material taken usually from those experiments which have presented the most complete and precise information, wherever experimental results do not contradict each other. Otherwise, comparisons between results of different experiments are made where relevant. Thus these lectures are not intended to give a balanced survey of all experiments which have contributed to the field, but are concerned rather with a description of the main conclusions which have emerged from the experimental work.

2. BEAMS AND DETECTORS

2.1 Neutrino beams

Two radically different beam types have been used so far in neutrino experimentation: the narrow-band beam (NBB) and the wide-band beam (WBB). Figure 1 illustrates the principle of the two beam types.

The basic idea of the NBB is the sign and momentum selection of secondary hadrons, i.e. π's and K's. A fraction of these subsequently decay via the two-body decay channels $\pi \to \mu\nu$ and $K \to \mu\nu$ in an evacuated decay tunnel. The resulting

μ's and the remaining hadrons are absorbed in a sufficiently long shield. The decay angle θ in the laboratory frame, measured experimentally by the radial distance of the event vertex to the beam centre, determines the energy of the neutrino apart from the ambiguity of whether a π or a K was the parent particle ("dichromacy" for fixed θ):

$$E_\nu \simeq \frac{2\gamma E^*_\nu}{1 + \gamma^2\theta^2} ,$$

where E^*_ν denotes the neutrino energy in the rest frame of the parent particle, and $\gamma = E_{\pi,K}/m_{\pi,K}$. The maximum neutrino energy is achieved in the forward direction ($\theta = 0$), and it drops by a factor of 2 for an angle $\theta = 1/\gamma$, which corresponds to an emission of the neutrino at $\theta^* = 90°$ in the rest frame of the parent particle. Integrated over all angles θ, the neutrino energy spectrum is flat between zero and the maximum energy, since the two-body decay is isotropic, i.e. flat in $\cos\theta^*$:

$$E_\nu \simeq \gamma E^*_\nu(\cos\theta^* + 1) .$$

In practice, the finite radius of a neutrino detector provides an angle cut-off and thereby a cut-off at low energies.

The resolution in the reconstructed neutrino energy is determined by the parent momentum [200 ± 10 (r.m.s.) GeV/c], the divergence of the parent beam (σ = 0.2 mrad), the uncertainty of the decay point along the tunnel (σ = 87 m), and the resolution in the measurement of the radial distance. The quoted numbers refer to the CERN NBB. The resulting over-all resolution is $\sigma(E) \sim 40\%$ for ν_π and $\sigma(E) \sim 15\%$ for ν_K. The resolution of the FNAL NBB is worse, mainly owing to a much larger parent momentum spread. However, the new FNAL NBB at present under construction will be of much better quality.

The decays of hadrons before sign and momentum selection give rise to a WBB background which peaks towards low energy. In order to minimize this unwanted background, the distance between the target and the beam-forming elements is kept

as short as possible. This WBB background is particularly important for neutral current studies, and for the study of "wrong-sign" events.

The determination of the absolute neutrino flux is done by monitoring

a) the total intensity of the sign and momentum-selected hadrons (π^+, K^+, and p in the positive beam, and π^- and K^- in the negative beam) by means of, for example, beam current transformers, and

b) the parent beam composition (π^+:K^+:p and π^-:K^- ratios) by means of a Čerenkov counter with variable threshold.

The WBB is the most intense neutrino beam. The basic focusing element is a horn, placed after the target. It focuses the hadrons with the "right" sign towards the detector, and defocuses the other sign. The focusing is achieved by a toroidal magnetic field produced by a pulsed strong current between an inner and an outer conductor. The focusing property is usually improved by a second horn ("reflector"). Since the horn focuses over a large momentum range, the resulting neutrino flux is high. However, the sign selection is poor compared to the NBB: at CERN the contamination of neutrinos from wrong-sign parents is about 3% in the ν beam and about 15% in the $\bar{\nu}$ beam. The flux monitoring at CERN is performed by means of a series of semiconductor detectors which are embedded in the muon shield. (They are also used for the NBB monitoring.) The neutrino flux can be inferred from the intensity and radial distribution of the muons at different depths.

At FNAL a variety of wide-band beams have been employed. In addition to a horn-focused WBB which peaks around 15 GeV, a quadrupole triplet beam and a sign-selected unfocused beam are also in operation. The quadrupole triplet beam has considerably less low-energy neutrinos compared to the horn-focused beam, but maintains the high-energy flux. While the hard spectrum is well-suited for counter experiments, the substantial mixture of both-sign neutrinos ($\nu + \frac{2}{3}\bar{\nu}$) is a disadvantage. The sign-selected unfocused beam has a lower flux than either the horn-focused or quadrupole triplet beam. A pair of dipole magnets serves to select the sign of the parent hadrons, thus producing relatively pure ν and $\bar{\nu}$ beams.

A comparison of the fluxes of the beams described is given in Fig. 2. A summary of the merits of the NBB and WBB is given in Table 1.

Table 1

Comparison of the main characteristics of NBB and horn-focused WBB

	Narrow-band beam	Horn-focused wide-band beam
Intensity	Low	High
Parent momentum	Fixed	All momenta
ν energy spectrum	Flat ("dichromatic" for fixed radius)	Falls steeply with energy
Knowledge of ν energy	Yes (apart from the π/K ambiguity)	No
$\nu/\bar{\nu}$ sign selection	Very good ($\sim 10^{-3}$-10^{-4} at high energies)	Reasonable (10^{-1}-10^{-2})
ν flux monitoring	Easy	Possible

2.2 Neutrino detectors

Because of the small neutrino cross-section, neutrino detectors need a very massive target. Bubble chambers are limited in their target mass to $\sim$ 10 tons, in contrast to electronic detectors which can afford target masses of up to $\sim$ 1000 tons.

Electronic detectors and bubble chambers are quite complementary. The main characteristics of both types of detectors are listed in Table 2.

Electronic detectors usually measure the total energy of the hadron shower cascade by means of scintillation counters. The resolution is, in general, bad at low energies, but improves with increasing energy. A typical figure is $\sigma \sim 10\%$ at a hadron shower energy of 100 GeV.

Full containment of the hadron cascade is of great importance since the shower development has large statistical fluctuations and makes corrections for leakage of shower energy difficult.

Table 2

Comparison of the main characteristics of electronic detectors and bubble chambers

Electronic detectors	Bubble chambers
Target mass up to $\sim$ 1000 tons	Target mass $\sim$ 10 tons
Excellent μ identification by range	μ identification with external muon identifier (EMI)
Neutral component of shower well measured	Neutral component of shower in part invisible
Blind to details of the shower	Very good for details of the shower (identification of electrons, V^0's...)

The muon momentum is determined by the bending in a magnetic field. The momentum resolution in electronic detectors is usually dominated by multiple scattering, and in bubble chambers by the precision of the muon track coordinates. In order to cover most of the kinematically accessible region, good acceptance up to very large muon scattering angles (several 100 mrad) is important.

Thus the measured quantities in electronic detectors are typically the total hadronic energy, the radial distance of the vertex to the beam centre, and the angles and momenta of outgoing muons (if any). Experiments now under construction at CERN and at FNAL aim also at a determination of the direction of the hadron shower, which is relevant to the kinematics of neutral current events where the outgoing neutrino is unobserved.

For illustration, Fig. 3 shows the electronic detectors of the Harvard-Pennsylvania-Wisconsin-Fermilab (HPWF) Collaboration, the CalTech-Fermilab (CITF) Collaboration, and the CERN-Dortmund-Heidelberg-Saclay (CDHS) Collaboration. The latter, contrary to the first two detectors, is a combined-function device in the sense that the functions of target, hadron calorimeter, and muon spectrometer are combined. The detectors are shown with their correct relative dimensions, together with the Big European Bubble Chamber (BEBC) as an example of a bubble chamber detector instrumented with an external muon identifier.

3. KINEMATICS, THE SCALING HYPOTHESIS, AND THE QUARK-PARTON MODEL

The best known process in neutrino scattering is the deep inelastic charged current (CC) reaction on nucleons (Fig. 4):

$$\nu + N \rightarrow \mu^- + X$$

and

$$\bar{\nu} + N \rightarrow \mu^+ + X$$

(ν without an index means a ν_μ throughout these notes). This process, as well as the neutral current (NC) reaction and the scattering of electrons and muons, is described by three independent variables:

$$s = (p + k)^2$$

$$Q^2 = -q^2 = -(k - k')^2 = 4E_\nu E' \sin^2 (\theta/2)$$

and

$$\nu = \frac{P \cdot q}{M} = E_\nu - E' = E_H - M$$

(for the notation, see Fig. 4). Instead of Q^2 and ν, one can use the dimensionless Bjorken scaling variables,

$$x = \frac{Q^2}{Q^2_{max}} = \frac{Q^2}{2M\nu} \quad \text{and} \quad y = \frac{\nu}{E_\nu} ,$$

where y denotes the fractional energy transfer to the nucleon system.

The double differential cross-section can be described in terms of three "structure functions", $F_i(x,Q^2)$, $1 \leq i \leq 3$, which describe the hadronic structure at the bottom vertex of Fig. 4. This double differential cross-section is then[2)]

$$\frac{d^2\sigma^{\nu,\bar{\nu}}}{dxdy} = \frac{G^2ME}{\pi}\left[\left(1 - y - xy\,\frac{M}{2E}\right) F_2^{\nu,\bar{\nu}}(x,Q^2) + \frac{y^2}{2}\, 2xF_1^{\nu,\bar{\nu}}(x,Q^2)\right.$$

$$\left. \pm \left(y - \frac{y^2}{2}\right) xF_3^{\nu,\bar{\nu}}(x,Q^2)\right] , \qquad (1)\ ^{*)}$$

where G is the Fermi constant, M the nucleon mass, and E the neutrino energy.

---

*) For reasons of convenience, F_3 is defined as a positive quantity.

We assume that the weak hadronic current is charge symmetric. This property holds at low energies, as tested experimentally in weak decays; it has also to be verified at high energies. If charge symmetry holds, it leads to the following relations between the structure functions for scattering off protons and neutrons:

$$\left.\begin{aligned} F_i^{\nu n} &= F_i^{\bar{\nu} p} \\ F_i^{\bar{\nu} n} &= F_i^{\nu p} \end{aligned}\right\} \quad 1 \leq i \leq 3 ,$$

neglecting the small contribution of strange quarks in the nucleon. On an isoscalar target, i.e. on a target with the same number of protons and neutrons, the ν and $\bar{\nu}$ structure functions become equal:

$$F_i^{\nu} = F_i^{\bar{\nu}} = F_i , \qquad 1 \leq i \leq 3 .$$

For an isoscalar target and with the assumption of charge symmetry, in the limit of high energies (E >> M) Eq. (1) reduces to

$$\frac{d^2\sigma^{\nu,\bar{\nu}}}{dxdy} = \frac{G^2ME}{\pi}\left[(1 - y)\, F_2(x,Q^2) + \frac{y^2}{2}\, 2xF_1(x,Q^2) \pm \left(y - \frac{y^2}{2}\right) xF_3(x,Q^2)\right] . \quad (2)$$

Integrating over x, we get in the limit $y \to 0$ the "small-y" cross-section, which should be equal for ν and $\bar{\nu}$:

$$\left.\frac{d\sigma^{\nu}}{dy}\right|_{y=0} = \left.\frac{d\sigma^{\bar{\nu}}}{dy}\right|_{y=0} = \frac{G^2ME}{\pi} \int_0^1 F_2(x,Q^2)\, dx . \quad (3)$$

The small-y cross-section should rise linearly with energy, independently of further assumptions, in particular of the assumption of scaling. It determines the integral of the structure function F_2 at small Q^2, since small y confines Q^2 to small values. The equality of the ν and $\bar{\nu}$ small-y cross-sections provides a very clean test of charge symmetry. Note further that the linearity with energy at small y is hardly affected by possible thresholds of new particle production since this is bound to the large-y region. In practice the linearity is somewhat spoiled by the contribution from quasi-elastic events, especially at low energies.

The y-dependence of Eq. (2) is not explicit since Q^2 depends on y. We can only go further if the structure functions are at least approximately independent of Q^2. This is the case in the Bjorken scaling limit[3]: for $Q^2, \nu \to \infty$ while $x = Q^2/2M\nu$ remains fixed, the structure functions become functions of the dimensionless scaling variable x only:

$$F_i(x,Q^2) \xrightarrow{\text{scaling limit}} F_i(x) \ , \qquad 1 \leq i \leq 3 \ .$$

The electron-scattering data exhibit approximate Bjorken scaling behaviour, and we know at present that also neutrino-scattering data show qualitatively the same features.

In the scaling limit, Eq. (2) reduces to

$$\frac{d^2\sigma^{\nu,\bar{\nu}}}{dxdy} = \frac{G^2ME}{\pi}\left[(1 - y)\, F_2(x) + \frac{y^2}{2}\, 2xF_1(x) \pm \left(y - \frac{y^2}{2}\right) xF_3(x)\right] , \qquad (4)$$

where the dependence on y is now explicit. Integration over x and y yields the total cross-section,

$$\sigma^{\nu,\bar{\nu}} = \frac{G^2ME}{\pi}\left[\frac{1}{2}\int F_2(x)\ dx + \frac{1}{6}\int 2xF_1(x) + \frac{1}{3}\int xF_3(x)\ dx\right] . \qquad (5)$$

Defining as usual the parameters

$$A = \frac{\int 2xF_1(x)dx}{\int F_2(x)dx} \quad \text{and} \quad B = \frac{\int xF_3(x)dx}{\int F_2(x)dx} \ ,$$

we get for the total cross-section,

$$\sigma^{\nu,\bar{\nu}} = \frac{G^2ME}{\pi}\int F_2(x)\ dx\left(\frac{1}{2} + \frac{1}{6}\, A \pm \frac{1}{3}\, B\right)$$

and

$$\sigma^{\bar{\nu}}/\sigma^{\nu} = (3 + A - 2B)/(3 + A + 2B) \ .$$

It should be stressed at this point that the parameters A and B are only useful in the scaling limit, where the structure functions are not (or are only slightly) dependent on Q^2.

The approximate validity of the scaling hypothesis in electron scattering data has inspired the parton model for the underlying structure of hadrons. It is assumed that hadrons are made up of point-like, spin-½ constituents called partons. It is further assumed that the partons interact freely and independently, without interference. After the scattering, the partons rearrange themselves to form the final-state hadrons. The total cross-section is the incoherent sum of the elementary parton cross-sections.

In the quark-parton model the partons are identified with the quarks. In this picture, the nucleons consist of three valence-quarks and a "sea" of quark-antiquark pairs. The valence-quarks of protons and neutrons are u- and d-quarks, whereas all quark flavours contribute to the sea. However, the small amounts of strange and charmed quarks in the sea are neglected here for reasons of simplicity.

The naive quark-parton model has exact Bjorken-scaling behaviour as a consequence. In this model, the Callan-Gross relation holds:

$$F_2(x) = 2xF_1(x) \ . \tag{6}$$

Neutrino-scattering data are often analysed under the assumption of Eq. (6) as an exact relation. By so doing, the double differential cross-section (4) can be rewritten in terms of two new structure functions $q(x)$ and $\bar{q}(x)$:

$$\begin{aligned} \frac{d^2\sigma^{\nu}}{dxdy} &= \frac{G^2ME}{\pi}\left[q(x) + \bar{q}(x)\ (1 - y)^2\right] \\ \frac{d^2\sigma^{\bar{\nu}}}{dxdy} &= \frac{G^2ME}{\pi}\left[q(x)\ (1 - y)^2 + \bar{q}(x)\right] , \end{aligned} \tag{7}$$

where the structure functions $q(x)$ and $\bar{q}(x)$ are related to $F_2(x)$ and $xF_3(x)$ as follows:

$$\begin{aligned} F_2(x) &= q(x) + \bar{q}(x) \\ xF_3(x) &= q(x) - \bar{q}(x) \end{aligned}$$

and

$$q(x) = \frac{1}{2}\left[F_2(x) + xF_3(x)\right]$$

$$\bar{q}(x) = \frac{1}{2}\left[F_2(x) - xF_3(x)\right] .$$

If we calculate the fraction of the nucleon momentum which is carried by the interacting quark, it turns out that this fraction is just x. Together with Eqs. (7), where one sees the decomposition of the cross-section into fermion-fermion (antifermion-antifermion) scattering with a flat y-distribution, and into fermion-antifermion scattering with a $(1 - y)^2$ distribution, q(x) is interpreted as the fractional momentum distribution of the quark content, and, analogously, $\bar{q}(x)$ as the fractional momentum distribution of the antiquark content of the nucleon.

Recalling the definition of the B parameter, we see that B is related to the fraction of antiquark momentum in the nucleon:

$$B = \frac{\int xF_3(x)dx}{\int F_2(x)dx} = \frac{\int[q(x) - \bar{q}(x)]dx}{\int[q(x) + \bar{q}(x)]dx} = \frac{Q - \bar{Q}}{Q + \bar{Q}} .$$

The relative fraction of antiquark momentum is

$$\frac{\bar{Q}}{Q + \bar{Q}} = \frac{1 - B}{2} ,$$

whereas the ratio of the antiquark to quark momentum, denoted by α throughout this report, is related to B by

$$\alpha = \frac{\bar{Q}}{Q} = \frac{1 - B}{1 + B} . \tag{8}$$

Using the parameter B, we can write the ν and $\bar{\nu}$ differential cross-sections as

$$\begin{aligned} \frac{d\sigma^{\nu}}{dy} &\propto \left[(1 + B) + (1 - B)(1 - y)^2\right] \\ \frac{d\sigma^{\bar{\nu}}}{dy} &\propto \left[(1 + B)(1 - y)^2 + (1 - B)\right] \end{aligned} \tag{9}$$

or using α:

$$\frac{d\sigma^{\nu}}{dy} \propto \left[1 + \alpha(1 - y)^2\right]$$

$$\frac{d\sigma^{\bar{\nu}}}{dy} \propto \left[(1 - y)^2 + \alpha\right] . \tag{10}$$

The Callan-Gross relation is likely to be only approximately valid. The finite transverse momentum of the quarks from gluon exchange and the binding energy of the quarks suggest a violation of the Callan-Gross relation. We can generalize the foregoing analysis by defining three new structure functions as follows:

$$q(x) = \frac{1}{2}\left[2xF_1(x) + xF_3(x)\right]$$

$$\bar{q}(x) = \frac{1}{2}\left[2xF_1(x) - xF_3(x)\right]$$

and

$$q_L(x) = F_2(x) - 2xF_1(x) .$$

Note that $q_L(x)$ is proportional to the Callan-Gross violation. We then get the double differential cross-section,

$$\frac{d^2\sigma^{\nu}}{dxdy} = \frac{G^2ME}{\pi}\left[q(x) + q_L(x)(1 - y) + \bar{q}(x)(1 - y)^2\right]$$

$$\frac{d^2\sigma^{\bar{\nu}}}{dxdy} = \frac{G^2ME}{\pi}\left[q(x)(1 - y)^2 + q_L(x)(1 - y) + \bar{q}(x)\right] . \tag{11}$$

The Callan-Gross violation gives rise to a term linear in y which shows up with the same sign and magnitude both in the ν and the $\bar{\nu}$ differential cross-sections. It is up to experimenters to measure its magnitude. The coefficient of the linear term in the y-distribution, normalized to the sum of the coefficients of the flat y and $(1 - y)^2$ components, is related to the previously defined parameter A as follows:

$$\frac{\int q_L(x)dx}{\int q(x)dx + \int \bar{q}(x)dx} = \frac{\int F_2(x)dx - \int 2xF_1(x)dx}{\int 2xF_1(x)dx} = \frac{1 - A}{A} . \tag{12}$$

Note, however, that this determination of A from the shape of the y-distribution is only valid in the scaling limit.

4. CHARGED CURRENT REACTIONS

4.1 Total cross-section

The standard local current-current weak interaction theory predicts that the cross-section of neutrino scattering off point-like spin-½ objects grows linearly with energy. At very high energies, a departure from linearity is expected owing to the propagator term from the W-boson exchange. On the other hand, the scaling hypothesis predicts the deep inelastic structure functions of the nucleon to scale in the dimensionless variable x. As a consequence, the neutrino-nucleon cross-section is expected to grow linearly with energy as well, if scaling works. The study of the ν and $\bar{\nu}$ total cross-sections on nucleons therefore provides a fundamental test both of the weak interaction theory and of the structure of nucleons.

Total cross-sections have first been obtained by the heavy-liquid bubble chamber Gargamelle (GGM) [4,5] in a low-energy WBB at the CERN Proton Synchrotron (PS) (the flux peaks around 2 GeV). The results are shown in Fig. 5 and are consistent with a linear rise, with slopes of

$$\sigma^{\nu}/E = (0.72 \pm 0.05) \times 10^{-38} \text{ cm}^2 \text{ GeV}^{-1} \text{ nucleon}^{-1}$$

and

$$\sigma^{\bar{\nu}}/E = (0.29 \pm 0.02) \times 10^{-38} \text{ cm}^2 \text{ GeV}^{-1} \text{ nucleon}^{-1} ,$$

and a ratio of $\bar{\nu}$ to ν total cross-sections

$$\sigma^{\bar{\nu}}/\sigma^{\nu} = 0.40 \pm 0.02 .$$

Surprisingly, the GGM data support the scaling hypothesis, although scaling is an asymptotic prediction and is not yet expected to work at such low energies and Q^2; this prompted the idea of "precocious scaling". The B parameter which can then be determined is

$$B = 0.86 \pm 0.04$$

or, alternatively,

$$\alpha = 0.075 \pm 0.023 ,$$

thus exhibiting an antiquark-to-quark ratio in the nucleon of (7.5 ± 2.3)% at low energies.

At higher energies (i.e. in the domain $30 < E_\nu < 200$ GeV, where data are available) it is *a priori* not clear whether scaling continues to describe the data, because of the possible onset of the production of new heavy particles and/or because the interaction between quarks may show up as Q^2-dependent non-scaling terms.

The small-y cross-section (see Section 3) is relatively insensitive to new hadronic thresholds. It tests the locality of the weak current-current coupling (via the predicted linearity with energy at y = 0, independent of the scaling hypothesis) and charge symmetry (via the equality between ν and $\bar{\nu}$ small-y cross-sections). Since the limiting case y = 0 is only accessible by extrapolation from small but finite y-values, corrections have to be applied. Quasi-elastic events are to be subtracted since their cross-section is energy-independent. Furthermore, small corrections for the effect of strange quarks (the neutrino couples both to d- and s-quarks; the antineutrino couples to u-quarks only; for antiquarks the situation is the reverse) and for a small deviation of the neutron/proton ratio from 1 in the actual targets are to be applied.

The CITF experiment has recently reported the measurement of small-y cross-sections[6] in the energy range 45 to 205 GeV. The results are given in Fig. 6a. The data are consistent with a linear rise of the small-y cross-sections with energy and with the equality for ν and $\bar{\nu}$. The best fit to the combined ν and $\bar{\nu}$ data yields the slope

$$\sigma(y = 0)/E = (0.719 \pm 0.035) \times 10^{-38} \text{ cm}^2 \text{ GeV}^{-1} \text{ nucleon}^{-1}$$

at an average incident energy of $\sim$ 100 GeV. The quoted error contains an over-all normalization error of 4% which, however, is not relevant to the comparison of the ν and $\bar{\nu}$ slopes. These are in good agreement, demonstrating that charge symmetry holds within ±5% at high energies.

The average "small-y" slope has also been reported from the BEBC experiment[5]:

$$\sigma(y = 0)/E = (0.79 \pm 0.07) \times 10^{-38} \text{ cm}^2 \text{ GeV}^{-1} \text{ nucleon}^{-1} ,$$

consistent with the more precise CITF value.

The CITF experiment has also reported new results on total ν and $\bar{\nu}$ cross-sections[7] in the same energy range $45 < E < 205$ GeV, measured in a NBB with external flux normalization. The BEBC group[5] has also published preliminary results obtained in a NBB. The results of both experiments are shown in Fig. 6b together with the previously mentioned GGM results. The measured slopes are summarized in Table 3.

Table 3

Slopes of ν and $\bar{\nu}$ total cross-sections for the GGM, CITF, and BEBC experiments

Energy (GeV)	GGM	CITF	BEBC (preliminary; statistical errors only)	
2-10	0.72 ± 0.05			Neutrinos
20-100		0.61 ± 0.02	0.61 ± 0.04	
100-200		0.62 ± 0.03	0.55 ± 0.04	
2-10	0.29 ± 0.02			Anti-neutrinos
20-100		0.28 ± 0.01	0.25 ± 0.02	
100-200		0.34 ± 0.03	0.32 ± 0.04	

Apparently, in the high-energy domain the combined results of both experiments are compatible with being energy-independent, and leave room for only a mild energy dependence at most. However, the ratio of the $\bar{\nu}$ to ν cross-sections show a

common trend to rise gently with energy, although the reason for the rise is different for the BEBC and CITF experiment (for BEBC the ν cross-section falls with energy, while for CITF the $\bar{\nu}$ cross-section rises with energy).

Preliminary data from the CDHS experiment[8] for the cross-section ratio as a function of energy are included in Fig. 6b. There is no evident energy dependence of the CDHS data, and the data are consistent with the CITF and BEBC results. The CDHS data points show statistical errors only. A common flux normalization error of $\sim$ 10% for all energies, and another uncertainty in the K/π ratio leading to an over-all error of $\sim$ 15% above 100 GeV only, are not included in the error bars.

The CITF experiment quotes the ratio of the average slopes of the $\bar{\nu}$ and ν cross-sections as 0.48 ± 0.05. In the scaling limit, and with strict validity of the Callan-Gross relation, this corresponds to

$$B = 0.70 \pm 0.09 ,$$

and according to Eq. (8)

$$\alpha = 0.17 \pm 0.06 .$$

The CDHS data are consistent with these results.

While there is no established energy dependence of the slopes above 30 GeV, there is a significant drop in the slope for ν from low energies (GGM) to high energies (BEBC, CITF) which does not occur for $\bar{\nu}$. The reason for this drop is unclear. It might be due to a Q^2-dependence of the structure functions (see Section 4.5). There is also an indication of a rise of the antiquark content of the nucleon (α = 7.5% for GGM, α = 17% for CITF).

4.2 y-distributions

Recent experimental results from CDHS[8], CITF[6,7], and BEBC[5] have not confirmed earlier experimental work, which reported substantial departure from the scaling behaviour[9]. Hence those earlier results will not be discussed here.

A good measurement of the y-distribution is a difficult task both for counter experiments and bubble chambers. To measure the hadron energy in a

bubble chamber, one has to correct for the missing neutral component of the shower. For a counter experiment, a uniform acceptance up to the largest muon scattering angles (which occur at large y) is important, as is full containment of the hadronic cascade in the measuring device. The NBB operation is particularly useful since the neutrino energy reconstructed from the radial position of the event enables an invaluable cross-check on the sum of hadron energy and muon momentum as measured in the detector.

Both the CDHS[8] and the CITF[10,11] experiments have recently provided preliminary data on y-distributions. Figure 7 shows the CDHS y-distribution for ν and $\bar{\nu}$ events in the energy range between 30 and 250 GeV. The distributions are compatible with the notion that the ν y-distribution is predominantly flat with a small $(1 - y)^2$ component from the antiquark content of the nucleon, the reverse being true for $\bar{\nu}$. The full lines represent a fit to the data with flat and $(1 - y)^2$ components only. A possible linear contribution in the y-distribution, indicative of a Callan-Gross violation, is not favoured by the data, although a linear term < 0.15 cannot be ruled out at the present stage of the analysis.

The y-distributions look like one would expect them to in the quark-parton model. They are consistent with $B = 0.70 \pm 0.09$, or equivalently with an antiquark content $\alpha = 0.17 \pm 0.06$ as derived above (see Section 4.1) from the CITF result $\sigma^{\bar{\nu}}/\sigma^{\nu} = 0.48 \pm 0.05$, with the assumption of scaling and the validity of the Callan-Gross relation.

The y-distributions do not show a significant energy dependence in the range 30 to 200 GeV. This is demonstrated in Fig. 8 with preliminary results on $\langle y \rangle$ from CITF and CDHS. In conclusion, the y-distributions above 30 GeV are consistent with the scaling hypothesis.

4.3 x-distributions and structure functions

The first evidence for scaling in x-distributions of neutrino scattering data has been reported by the GGM Collaboration. Using the same "scaling cuts" applied at SLAC for eN scattering data ($Q^2 > 1$ GeV^2, $W^2 > 4$ GeV^2, where

$W^2 = M^2 + 2M\nu - Q^2$ is the square of the invariant final-state hadron mass), a sample of 200 ν and 29 $\bar{\nu}$ events has remained. From these events, the structure functions $F_2(x)$ and $xF_3(x)$ have been determined[12] from the sum of the ν and $\bar{\nu}$ differential cross-sections and their difference, respectively. The result for $F_2(x) = q(x) + \bar{q}(x)$ is shown in Fig. 9 together with the structure function $F_2^{eN}(x)$ derived from e scattering on an isoscalar target. Since the electromagnetic interaction senses the electric charges of the u- and d-quarks ($+^2/_3$ and $-^1/_3$, respectively), whereas the weak interaction senses the equal (up to differences of quark masses) weak charges of the quarks, $F_2^{eN}(x)$ is to be divided by the average squared charges of the u- and d-quarks: $^5/_{18} = 1/3.6$. The agreement between the eN data and the GGM νN data is reasonably good.

At high energies, preliminary data on the x-distribution exist from the CDHS experiment. Figure 10 shows the x-distribution of CC events, separated for ν and $\bar{\nu}$, for different bins of y, integrated over the energy range $30 < E_\nu < 180$ GeV. The data are consistent with the picture that valence-quarks cover a larger range of x whereas the sea-quarks are compressed to small x. This is clearly visible, in particular at large y for $\bar{\nu}$, where virtually only sea-quarks contribute.

To demonstrate the difference in the x-distribution for valence- and sea-quarks, Fig. 11 shows the x-distribution for $\bar{\nu}$ and ν data for $y > 0.8$. Apart from a small correction, the $\bar{\nu}$ distribution represents the structure function of the sea, $\bar{q}(x)$. It can be parametrized roughly like $(1 - x)^7$. Note, however, that Fig. 11 displays raw data. They are corrected neither for acceptance and experimental resolution nor for Fermi motion.

The preliminary x-distributions of the CDHS experiment do not show a substantial dependence on the energy in the range 30-180 GeV, again confirming the approximate validity of Bjorken scaling. However, when calculating $F_2(x)$ from the sum of the differential cross-sections $d\sigma^\nu/dx$ and $d\sigma^{\bar{\nu}}/dx$, the resulting distribution shows a shrinkage towards small x compared to $F_2^{eN}(x)$ (see Fig. 9). Note that unfolding the Fermi motion in the CDHS data would increase the shrinkage effect.

The integral $\int F_2(x)\,dx$ is the total fractional momentum of the nucleon carried by interacting constituents. In the scaling limit and in the absence of a Callan-Gross violation, it is determined from the sum of ν and $\bar{\nu}$ total cross-sections. The resulting value for GGM energies is[4,12]

$$\int F_2(x)\,dx = 0.52 \pm 0.03 \ .$$

This means that $\sim$ 50% of the nucleon momentum is carried by non-interacting constituents, presumably gluons. An evaluation of the same integral is also obtained from the small-y cross-section in a more model-independent way, since this measurement is insensitive to the validity of scaling and of the Callan-Gross relation. The results are

$$\int F_2(x)\,dx = 0.45 \pm 0.02 \quad \text{(CITF)}$$

and

$$\int F_2(x)\,dx = 0.51 \pm 0.05 \quad \text{(BEBC)} \ ,$$

and agree reasonably well with the GGM result, which has been determined in a comparable range of small Q^2.

4.4 A short digression on inelastic e/μ-scattering results

In the past years a series of experiments have been carried out at SLAC (e scattering) and FNAL (μ scattering) in order to study the structure of the nucleon with a well-understood projectile. The double differential cross-section for inelastic e/μ scattering on nucleons is given by

$$\frac{d^2\sigma^{e,\mu}}{dxdy} = \frac{8\pi\alpha^2 ME}{Q^4}\left[\left(1 - y - xy\,\frac{M}{2E}\right)F_2^{e,\mu}(x,Q^2) + \frac{y^2}{2}\,2xF_1^{e,\mu}(x,Q^2)\right] , \qquad (13)$$

where α denotes the fine structure constant. The cross-section is described by two structure functions only, since the electromagnetic current is a parity-conserving vector current, in contrast to the parity-violating V-A current in CC neutrino scatterings.

The basic result of the first series of e-scattering experiments at SLAC was that the scaling hypothesis works reasonably well. Meanwhile, recent data on e scattering on protons and deuterium[13], and μ scattering on protons, deuterium, and iron nuclei[14], have provided evidence for a gentle scale-breaking Q^2-dependence of the structure functions. The evidence for the scale breaking of the structure function F_2 is shown in Fig. 12 for (ep)-scattering and (μp)-scattering data. If scaling was exact, then all the data would fall on horizontal lines, i.e. would be independent of Q^2. Instead, the data indicate a rise at small x and a fall at large x as Q^2 is increased. As a consequence, the structure function F_2 shrinks towards small x when Q^2 increases. This is indicated in Fig. 13 on the basis of both (ep)- and (μp)-scattering data.

Further data from scattering on deuterium and iron nuclei show a similar trend. Within the Q^2 range accessible in the experiments ($1 < Q^2 < 16$ GeV^2 at SLAC, $1 < Q^2 < 40$ GeV^2 at FNAL), the data appear to follow approximately straight lines in a plot of $\ln F_2$ versus $\ln Q^2$. The consistency of all data is clearly visible in Fig. 14 where the slopes $\partial \ln F_2/\partial \ln Q^2$ are summarized for different experiments. The slopes appear to be positive for $x < 0.2$ and turn over to negative values above $x \sim 0.2$. It should be noted, however, that there is no *a priori* justification that the extrapolation to higher Q^2 of the straight lines shown in Fig. 12 should provide a valid description of data.

A further important aspect of the e/μ-scattering data is the ratio $R = \sigma_L/\sigma_T$, the ratio of the photoabsorption cross-sections for the longitudinal and transverse virtual photons; R is related to the structure functions F_2 and $2xF_1$ as follows:

$$A(x,Q^2) = \frac{2xF_1(x,Q^2)}{F_2(x,Q^2)} = \frac{1 + (2Mx/Q)^2}{1 + R} \simeq \frac{1}{1 + R} . \qquad (14)$$

R is thus approximately related to the previously defined parameter A (see Section 3) which measures the amount of the Callan-Gross violation:

$$A = \frac{\int 2xF_1 dx}{\int F_2 dx} \cong \frac{1}{1 + R} \quad \text{or} \quad R = \frac{\sigma_L}{\sigma_T} \cong \frac{1 - A}{A} . \qquad (15)$$

Comparing with Eq. (12), it can be concluded that R is just the coefficient of the (1 - y) term to be expected in the ν and in the $\bar{\nu}$ y-distributions. In this context it is of great significance that e- and μ-scattering experiments both agree on a non-zero value for R, although the magnitude of R is uncertain[15]. The ratio R is extremely difficult to measure: in order to separate the structure functions $2xF_1$ and F_2 it is necessary to measure cross-sections at different polarizations of the virtual photon. This is accomplished at SLAC by measuring at different scattering angles, and at FNAL by measuring at different beam energies. Hence the systematic errors from the comparison of data measured in different set-ups are dominant. A value of R somewhere between 0.1 and 0.4 seems to be the best that one can conclude from the present data.

These e/μ-scattering results are particularly important for neutrino experiments, since the underlying structure functions are believed to have the same x- and Q^2-dependence. On the basis of the e/μ-scattering data, gentle scale-breaking effects could be expected to appear also in neutrino-scattering results. The precise measurement of scale-breaking effects is now the major challenge for CC neutrino-scattering work.

If Q^2 is indeed the variable where scale-breaking effects show up most clearly, plots versus the neutrino energy are not the most effective ones for studying scaling violations since, for every energy bin, all values of Q^2 between 0 and 2ME can contribute. Nevertheless, large scale-breaking effects must also show up in plots versus energy, since $\langle Q^2 \rangle$ increases with energy. The previous discussion has shown that above $\sim$ 30 GeV no significant energy-dependent effect has been observed in CC ν and $\bar{\nu}$ scattering.

4.5 Scaling violations

The only significant energy-dependent scale-breaking effect showing up so far in ν and $\bar{\nu}$ scattering on nucleons is an apparent change in the slope of the ν cross-section, and in the relative amount of antiquarks, when going from the GGM energy range to energies above 30 GeV. In order to further explore energy-dependent effects, $\langle Q^2 \rangle$ divided by the energy enables a useful check to be made.

The ratio $\langle Q^2 \rangle / E = 2M\langle xy \rangle$ is constant for exact Bjorken scaling. Since $Q^2 = 4E\,E_\mu \times$ $\times \sin^2(\theta_\mu/2)$, the ratio $\langle Q^2 \rangle / E$ depends only on the muon track parameters, and corrections for errors in the determination of the hadronic energy are only relevant to the binning in E. Thus $\langle Q^2 \rangle / E$ is particularly useful for bubble chambers. Figure 15 shows results from BEBC[5], the FNAL 15' chamber[16], and GGM[4,12]. Taken altogether between 1 and 200 GeV, these data exhibit significant deviations from exact scaling in neutrino scattering. The data are consistent, as indicated by the lines, with the empirical relation $\langle Q^2 \rangle / E \propto E^{-0.14}$ obtained from a fit of scaling deviations observed in e/μ scattering. It is tempting to conclude from this comparison that significant scaling deviations are observed in neutrino scattering, and that they are consistent with those observed in e/μ scattering. However, the high-energy BEBC data alone, not taken in conjunction with the low-energy GGM data, do not exhibit a significant violation of scaling.

Small scale-breaking effects in neutrino interactions are not only expected on the basis of the results of the e/μ-scattering experiments, but are also predicted by asymptotically free gauge theories[17] of strong interactions, also referred to as quantum chromodynamics (QCD). In this theory, the colour of quarks is regarded as the source of the field which mediates the forces between the quarks. The field quanta are eight gluons, which carry colour. The quark-gluon coupling constant α_s has not a unique value, but is dependent on Q^2:

$$\frac{\alpha_s}{\pi} = \frac{12}{(33 - 2m)} \frac{1}{\ln (Q^2/\Lambda^2)} . \qquad (16)$$

Here Λ is *a priori* an arbitrary parameter. It may have the meaning of something like the average distance between the quarks (Λ = 0.5 GeV corresponds to a distance of 0.4 fm); m is the number of quark flavours. At very small distances or, equivalently, very high Q^2, the coupling strength goes to zero. This effect is supposed to explain that in spite of the strong interaction between quarks, they behave like almost free particles when electrons, muons, or neutrinos interact with them inside a nucleon. The number of quark flavours can be as big as 16 while maintaining the property of asymptotic freedom. The behaviour of the theory

at large distances or, equivalently, low Q^2 is not yet known. Perturbation theory methods are only meaningful at $Q^2 >> \Lambda^2$ to make the coupling strength sufficiently low. However, this theoretical problem should not stop experimentalists from examining the whole Q^2 domain which is experimentally accessible.

The only group which has so far reported preliminary results on the Q^2-dependence of structure functions on neutrino scattering, is the BEBC[18] Collaboration. They have used data recorded in a NBB in the energy range 20-200 GeV, as well as the GGM data recorded in a low-energy WBB in the range 2-10 GeV. The data consist of $\sim$ 3000 ν and $\sim$ 2000 $\bar{\nu}$ events from GGM, and $\sim$ 1100 ν and $\sim$ 250 $\bar{\nu}$ events from BEBC. The data cover a range of Q^2 over three orders of magnitude, from 0.1 to 100 GeV^2.

In order to extract the structure functions, the data have been divided into bins of Q^2, x, and y. The experimental resolution and the Fermi motion in freon (GGM) and the heavy neon-hydrogen mixture (BEBC) have been accounted for. Starting from Eq. (1) and assuming charge symmetry, the following event numbers are computed with the known ν and $\bar{\nu}$ fluxes $\phi^{\nu}(E)$ and $\phi^{\bar{\nu}}(E)$:

$$
\begin{aligned}
N_1^{\nu,\bar{\nu}}(x,Q^2) &= \iint \frac{G^2 ME}{\pi} \cdot T \cdot \phi^{\nu,\bar{\nu}}(E) \cdot \frac{y^2}{2}\, dy\, dE\,, \\
N_2^{\nu,\bar{\nu}}(x,Q^2) &= \iint \frac{G^2 ME}{\pi} \cdot T \cdot \phi^{\nu,\bar{\nu}}(E) \cdot \left(1 - y - xy\,\frac{M}{2E}\right) dy\, dE\,, \qquad (17) \\
N_3^{\nu,\bar{\nu}}(x,Q^2) &= \iint \frac{G^2 ME}{\pi} \cdot T \cdot \phi^{\nu,\bar{\nu}}(E) \cdot \left(y - \frac{y^2}{2}\right) dy\, dE\,,
\end{aligned}
$$

where T is the number of nucleons in the target. The sum of these event numbers, weighted with the corresponding structure functions in each (x,Q^2) bin, are just the observed event numbers:

$$
\begin{aligned}
N_{obs}^{\nu} &= 2xF_1 \cdot N_1^{\nu} + F_2 \cdot N_2^{\nu} + xF_3 \cdot N_3^{\nu} \\
N_{obs}^{\bar{\nu}} &= 2xF_1 \cdot N_1^{\bar{\nu}} + F_2 \cdot N_2^{\bar{\nu}} - xF_3 \cdot N_3^{\bar{\nu}}\,.
\end{aligned} \qquad (18)
$$

With the assumption of $2xF_1 = F_2$, i.e. the validity of the Callan-Gross relation, we get from the sum and difference of the observed event numbers in each (x,Q^2) bin, the structure functions $F_2(x,Q^2)$ and $xF_3(x,Q^2)$, respectively. The results are shown in Fig. 16, where the results from BEBC, GGM, and from SLAC (ed)-scattering data are plotted. The SLAC data are multiplied by 9/5 = 1.8 to account for the relation

$$F_2^{\nu N} = \frac{18}{5} F_2^{eN} = \frac{18}{5} \frac{F_2^{ep} + F_2^{en}}{2} = \frac{9}{5} F_2^{ed} ,$$

arising from quark model considerations. The straight lines indicate empirical slopes $\partial \ln F_2 / \partial \ln Q^2$ which have been determined by Perkins et al.[19] from e/μ-scattering data, and which have been extrapolated tentatively into the so far unexplored Q^2 range up to 100 GeV^2.

The over-all agreement of the data is quite remarkable. The BEBC data compare well with the GGM data in the overlap regions. The neutrino data are roughly consistent with the Q^2 behaviour shown by the e/μ-scattering results. However, this consistency is dominated by the GGM data points, whereas the BEBC high-energy data taken alone neither support nor contradict (the error bars are statistical only) the qualitative features indicated by the straight lines. It is clear that more data are needed to clarify quantitatively the question of scaling violation in CC reactions.

Figure 17 shows the integral of the structure function F_2, plotted against $\ln Q^2$, computed with the assumption $2xF_1 = F_2$. Quasi-elastic events are included in the integral. For $Q^2 < 1$ GeV^2 the quasi-elastic process is dominant and the integral rises from ~ 0.4 for large Q^2 to about unity at low Q^2. In this Q^2 domain the nucleon reacts coherently as a whole, whereas at large Q^2 the constituent picture dominates, with 50-60% of the nucleon's momentum carried by non-interacting gluons.

Figure 18 shows the integral of the structure function xF_3 plotted against $\ln Q^2$, also computed with the assumption $2xF_1 = F_2$. The integral $\int xF_3\, dx$ represents the fractional momentum of valence-quarks only. The rapid rise below $Q^2 = 1$ GeV^2

is again due to the quasi-elastic contribution. For high Q^2, $\int xF_3\,dx$ shows the same falling tendency as $\int F_2\,dx$.

QCD predicts[17] the asymptotic values 0.43 for $\int F_2\,dx$ and zero for $\int xF_3\,dx$ in the limit $Q^2 \to \infty$ for m = 4 quark flavours. The latter can be seen intuitively, since QCD predicts with growing Q^2 (i.e. at distances becoming shorter and shorter) a rising contribution from $(q\bar{q})$ pairs. The fraction sea/valence is growing. As a consequence, $\sigma^{\bar{\nu}}/\sigma^{\nu}$ is expected to rise with energy, and for $E \to \infty$ one expects $\sigma^{\bar{\nu}} = \sigma^{\nu}$, and a relative fraction of valence/sea converging to zero. The ν and $\bar{\nu}$ y-distributions will become equal and tend to the asymptotic form $d\sigma/dy \propto 1 + (1 - y)^2$.

In the analysis of the structure functions, we can relax the Callan-Gross relation $2xF_1 = F_2$. In order to extract

$$A(x,Q^2) = \frac{2xF_1(x,Q^2)}{F_2(x,Q^2)} ,$$

the xF_3 term in Eq. (18) can be eliminated by adding the ν and $\bar{\nu}$ data. Then the y-distribution can be investigated in order to study $2xF_1/F_2$. Figure 19 shows the result for A as a function of $\ln Q^2$, for various ranges of x. The mean value of A is

$$\langle A \rangle = 0.96 \pm 0.20(0.09) \qquad \text{(BEBC)} ,$$

where the error quoted in brackets is the statistical error only. This result is in good agreement with

$$\langle A \rangle = 0.83 \pm 0.09 \qquad \text{(CITF)} ,$$

reported recently by the CITF group[11]. Altogether, the value of A obtained in ν scattering is compatible with a finite R, as reported from e/μ experiments, and with R = 0. Note, however, that A is strictly expected to be unity only in the asymptotic limit $Q^2 \to \infty$.

5. NEUTRAL CURRENT REACTIONS

In the five years which have elapsed since the discovery of neutral current (NC) reactions by the GGM group[20], a series of experiments have been carried out in order to answer the following basic questions:

a) What is the strength of NC compared to that of CC, and what is its energy-dependence?

b) What is the space-time structure of NC?

c) What is the isospin structure of NC?

We are now in a good position to have first answers to these questions since all recent experimental results are in good agreement. Experimental data are available in four different fields:

a) elastic neutrino scattering off electrons;

b) elastic neutrino scattering off protons;

c) deep inelastic inclusive neutrino scattering on isoscalar nuclei;

d) exclusive and semi-inclusive single-π production.

The cleanest NC reaction we can think of is neutrino-electron scattering, and we shall start with a discussion of the experimental situation.

5.1 Elastic neutrino scattering off electrons

The particularly attractive feature of νe scattering is that there is no uncertainty about the hadronic structure involved. As a consequence, νe scattering allows the cleanest study of the NC structure. The major drawback is, however, the very small cross-section. The ν cross-section is proportional to $s = 2mE$, where m is the mass of the target particle. Hence the cross-section for νe scattering is $\sim$ 2000 times smaller than the neutrino-nucleon cross-section. The νe-scattering experiments suffer notoriously from very small data samples and background problems.

Four NC reactions are possible in νe scattering:

$$\left.\begin{aligned} \nu_e + e^- &\to \nu_e + e^- \\ \bar{\nu}_e + e^- &\to \bar{\nu}_e + e^- \end{aligned}\right\} \text{ NC + CC}$$

$$\left.\begin{aligned} \nu_\mu + e^- &\to \nu_\mu + e^- \\ \bar{\nu}_\mu + e^- &\to \bar{\nu}_\mu + e^- \end{aligned}\right\} \text{ NC only}$$

Of these, ν_e and $\bar{\nu}_e$ can scatter via both NC and CC, whereas ν_μ and $\bar{\nu}_\mu$ scattering can take place only via the NC reaction. The expected cross-sections in the framework of the Weinberg-Salam model[21] have been calculated by 't Hooft[22] and are displayed in Fig. 20. In the Weinberg-Salam model, the neutral current j^λ_{NC} is a mixture of the neutral third isospin component j^λ_3 of the standard V-A current and the electromagnetic current j^λ_{em}:

$$j^\lambda_{NC} = j^\lambda_3 - 2 \sin^2 \theta_W \cdot j^\lambda_{em} \,. \tag{19}$$

The only free parameter in this model is the mixing angle θ_W, which is measured to be around 30° ($\sin^2 \theta_W \sim 0.25$; see Section 5.4). In the limiting case of $\sin^2 \theta_W = 0$, j^λ_{NC} maintains the pure V-A structure. For $\sin^2 \theta_W > 0$ the electromagnetic vector current adds a V+A term to the V-A structure.

The differential cross-section for νe scattering is given by:

$$\begin{aligned} \frac{d\sigma^\nu}{dy} &= \frac{2G^2 m_e E}{\pi}\left[\left(\frac{C_V + C_A}{2}\right)^2 + \left(\frac{C_V - C_A}{2}\right)^2 (1 - y)^2\right] \\ \frac{d\sigma^{\bar{\nu}}}{dy} &= \frac{2G^2 m_e E}{\pi}\left[\left(\frac{C_V + C_A}{2}\right)^2 (1 - y)^2 + \left(\frac{C_V - C_A}{2}\right)^2\right], \end{aligned} \tag{20}$$

with the variable $y = E_e/E$ which measures, analogously to the neutrino-nucleon scattering process, the fraction of energy transferred to the electron. The values of the coupling constants C_V and C_A are given in Table 4 for the Weinberg-Salam theory.

Note that the singular value $\sin^2 \theta_W = 0.25$ leads to a particularly nice symmetry in the world of leptons: the electromagnetic current is pure vector,

the charged weak current is an equal mixture of vector and axial vector, and the neutral weak current is a pure axial vector.

Table 4

Coefficients C_V and C_A in the Weinberg-Salam model for neutrino-electron scattering

Process	C_V	C_A
$\nu_e + e^-$	$1/2 + 2 \sin^2 \theta_W$	$1/2$
$\bar{\nu}_e + e^-$	$1/2 + 2 \sin^2 \theta_W$	$-1/2$
$\nu_\mu + e^-$	$-1/2 + 2 \sin^2 \theta_W$	$-1/2$
$\bar{\nu}_\mu + e^-$	$-1/2 + 2 \sin^2 \theta_W$	$1/2$

Owing to the interference between the NC and CC processes in $\nu_e e$ scattering, the cross-section is lower than the pure V-A prediction for small $\sin^2 \theta_W$. The only process studied experimentally is $\bar{\nu}_e + e^- \rightarrow \bar{\nu}_e + e^-$. The experiment has been performed at the Savannah River reactor by Reines and co-workers[23]. The experiment is particularly hard, because with $\sin^2 \theta_W \sim 0.25$ as determined from neutrino-nucleon inclusive measurements, the total cross-section does not differ greatly from the cross-section predicted by the V-A CC reaction alone. The reactor experiment has measured the recoil electron spectrum in two energy bands: $1.5 < E_e < 3.0$ MeV and $3.0 < E_e < 4.5$ MeV, respectively. The resulting cross-sections are

$$\sigma(\bar{\nu}_e e) = (0.87 \pm 0.25) \times \sigma(\text{V-A}) \qquad 1.5 < E_e < 3.0 \text{ MeV}$$

$$\sigma(\bar{\nu}_e e) = (1.7 \pm 0.44) \times \sigma(\text{V-A}) \qquad 3.0 < E_e < 4.5 \text{ MeV},$$

expressed in units of the V-A CC cross-section. Hence there is no significant evidence either for or against the existence of a NC contribution in the observed total cross-section. However, since the cross-section varies rapidly with $\sin^2 \theta_W$ (see Fig. 20), the authors quote a fairly precise value for this parameter: $\sin^2 \theta_W = 0.29 \pm 0.05$, in agreement with inclusive neutrino-nucleon scattering results.

The processes $\nu_\mu + e^- \to \nu_\mu + e^-$ and $\bar{\nu}_\mu + e^- \to \bar{\nu}_\mu + e^-$ have been studied by the GGM[24] and the Aachen-Padova[25] groups. The results are summarized in Table 5 and displayed in Fig. 21.

Table 5

Results of the Aachen-Padova and the GGM experiment on neutrino-electron elastic scattering cross-sections

Projectile	No. of events	Background	Slope of cross-section *)	Experiment
ν	10	4.2	1.2 ± 0.6	Aachen-Padova
$\bar{\nu}$	8	3.4	2.4 ± 1.1	
ν	1	0.5 ± 0.3	< 2.3	GGM
$\bar{\nu}$	3	0.44 ± 0.13	$1.0 \,^{+\,2.1}_{-\,0.9}$	

*) In units of 10^{-42} cm^2 GeV^{-1} electron^{-1}.

The major conclusion is that a signal has been established above background for both channels. The errors on the cross-sections are unfortunately large, reflecting the small data sample. The results do not enable a significant discrimination between various models for the NC space-time structure. However, as can be seen in Fig. 21, the Aachen-Padova cross-sections are in agreement with V+A, pure V or A, and with the Weinberg-Salam model, with $\sin^2 \theta_W = 0.38 \pm 0.10$, which is compatible with $\sin^2 \theta_W \sim 0.25$. Pure V-A coupling is not favoured by the Aachen-Padova data.

The over-all agreement of the νe scattering results with the predictions of the Weinberg-Salam model with $\sin^2 \theta_W \sim 0.25$ is somewhat spoiled by the observation made by the Aachen-Padova group that the average energy of the final-state electrons differs for ν_μ and $\bar{\nu}_\mu$ by about two standard deviations. The value $\sin^2 \theta_W = 0.25$, as suggested from neutrino-nucleon inclusive experiments, is a singular value for $\nu_\mu e$ and $\bar{\nu}_\mu e$ scattering, as can be seen in Table 5 and in Fig. 20: the interaction becomes a pure axial vector interaction since C_V becomes

zero. The ν_μ and $\bar{\nu}_\mu$ cross-sections become equal, and both y-distributions have the same form $1 + (1 - y)^2$. In other words, the measured energies of final-state electrons must have the same spectrum for equal ν_μ and $\bar{\nu}_\mu$ fluxes. Figure 22 shows the experimental result from the Aachen-Padova Collaboration: the observed electron energy distributions do not agree well with each other. However, they also do not agree particularly well with the Weinberg-Salam model, irrespective of whether $\sin^2 \theta_W = 0.38$ (which is their favoured value) or $\sin^2 \theta_W = 0.25$.

The over-all discrepancy with the Weinberg-Salam model with $\sin^2 \theta_W = 0.25$ is about three standard deviations, and it is up to everyone to reach his own conclusion. However, given the statistical problems of a very small data sample together with a large background, one should content oneself with seeing the $(\bar{\nu})_\mu$-e scattering process experimentally established, and wait for forthcoming experiments with hopefully larger statistics.

5.2 Elastic neutrino scattering off protons

Elastic neutrino scattering off protons is a unique tool for studying the hadronic NC, analogous in its importance to neutron β-decay. Various NC models give definite predictions for the NC to CC ratio at $Q^2 = 0$. Hence a precise measurement of this quantity puts restrictions on both the space-time and isospin structure of the weak NC[26].

Unfortunately, measurements are only possible above a minimum Q^2 since the outgoing proton must have a minimum energy in order to be detected. As a consequence, the Q^2-dependence of the form factors involved complicates the situation. In addition, the problem of a severe neutron background present in all experiments, in particular at low Q^2, has made the analysis very difficult.

Several experiments have been carried out to detect elastic ν_μ and $\bar{\nu}_\mu$ scattering off protons. The basic outcome is that both processes can be considered established experimentally, although the evidence is better for ν_μ than for $\bar{\nu}_\mu$. The measured NC/CC ratios are consistent with the Weinberg-Salam model with $\sin^2 \theta_W \sim 0.25$. However, the large errors on the results do not allow a crucial

test. The experimental results are summarized in Table 6. To indicate the experimental difficulties, the total number of observed events is given as well as the background estimate.

Table 6

Results for the ratios $R_\nu(\nu p) = \sigma(\nu_\mu + p \to \nu_\mu + p)/\sigma(\nu_\mu + n \to \mu^- + p)$ and $R_{\bar\nu}(\bar\nu p) = \sigma(\bar\nu_\mu + p \to \bar\nu_\mu + p)/\sigma(\bar\nu_\mu + p \to \mu^+ + n)$. The Q^2 interval is in all experiments nearly the same: $0.3 < Q^2 < 1.0$ GeV^2.

$R_\nu(\nu p)$	No. of events	Background	Experiment
0.17 ± 0.05 *)	30	7	HPW [27]
0.23 ± 0.09 *)	38	19	CIR [28]
0.12 ± 0.06	100	62	GGM [29]
0.10 ± 0.04	155	69	AP [30]
$R_{\bar\nu}(\bar\nu p)$	No. of events	Background	Experiment
0.2 ± 0.1 *)	22	8	HPW [27]

*) Uncorrected for $\overset{(-)}{\nu} + n \to \overset{(-)}{\nu} + n$, where np charge exchange occurs in the target nucleus.

The results of the Harvard-Pennsylvania-Wisconsin (HPW) and Columbia-Illinois-Rockefeller (CIR) Collaborations, in contrast to the quoted GGM and Aachen-Padova results, are not corrected for the NC reaction $\overset{(-)}{\nu}_\mu + n \to \overset{(-)}{\nu}_\mu + n$, where np charge exchange occurs in the target nucleus. This correction may lower the HPW and CIR results by 10-20%. The over-all agreement between the experiments is then quite good.

A direct comparison of the ν_μ and $\bar\nu_\mu$ elastic scattering rates is obtained from the measured ratios $R_\nu(\nu p)$ and $R_{\bar\nu}(\bar\nu p)$ from the HPW experiment if the ratio of the CC quasi-elastic cross-sections is known. Taking this as $\sigma(\bar\nu_\mu + p \to \mu^+ + n)/\sigma(\nu_\mu + n \to \mu^- + p) = 0.34$ [27], we obtain

$$\sigma(\bar\nu_\mu + p \to \bar\nu_\mu + p)/\sigma(\nu_\mu + p \to \nu_\mu + p) = 0.4 \pm 0.2 \ ,$$

where the error is statistical only. This ratio is not in favour of a parity-conserving pure V or A structure where the ratio is expected to be unity. However, this conclusion is only valid if one and only one Z boson mediates the weak NC interaction.

The results of the HPW Collaboration are shown in Fig. 23a for ν_μ scattering and in Fig. 23b for $\bar{\nu}_\mu$ scattering.

5.3 Inclusive inelastic neutrino scattering off protons

The measurement of the ν and $\bar{\nu}$ inclusive inelastic NC/CC cross-section ratio on protons, in contrast to the same measurement on isoscalar targets, enables a further check on the validity of the Weinberg-Salam model, extended by the Glashow-Iliopoulos-Maiani (GIM)[31] scheme to include the weak interaction between the u-, d-, s-, and c-quarks. In this model, the effective Lagrangian of the interaction of muon-neutrinos with quarks is given as

$$L = L^{CC} + L^{NC}$$

with

$$L^{CC} = \frac{G}{\sqrt{2}}\left\{\bar{\mu}\gamma_\lambda(1+\gamma_5)\nu\left[\bar{u}\gamma^\lambda(1+\gamma_5)\left(d\cos\theta_C + s\sin\theta_C\right)\right.\right.$$
$$\left.\left. + \bar{c}\gamma^\lambda(1+\gamma_5)\left(-d\sin\theta_C + s\cos\theta_C\right)\right]\right\}, \tag{21}$$

and

$$L^{NC} = \frac{G}{\sqrt{2}}\left\{\bar{\nu}\gamma_\lambda(1+\gamma_5)\nu\left[\bar{u}\gamma^\lambda\left(C_V + C_A\gamma_5\right)u + \bar{c}\gamma^\lambda(C_V + C_A\gamma_5)c\right.\right.$$
$$\left.\left. - \bar{d}\gamma^\lambda\left(C'_V + C'_A\gamma_5\right)d - \bar{s}\gamma^\lambda\left(C'_V + C'_A\gamma_5\right)s\right]\right\},$$

where θ_C denotes the Cabibbo angle. With the NC as defined in Eq. (19), we get the coupling constants

$$C_V = \frac{1}{2} - \frac{4}{3}\sin^2\theta_W \qquad C_A = \frac{1}{2}$$
$$C'_V = -\frac{1}{2} + \frac{2}{3}\sin^2\theta_W \qquad C'_A = -\frac{1}{2}. \tag{22}$$

Using Eqs. (22), taking $\theta_C = 0$, and for the sake of simplicity neglecting the small contributions from the sea, we calculate in the framework of the quark-parton model and for a proton target the ratios of NC to CC cross-sections to be

$$R_\nu^p = \frac{3}{4} - \frac{5}{3}\sin^2\theta_W + \frac{4}{3}\sin^4\theta_W \cong 0.42$$

$$R_{\bar\nu}^p = \frac{3}{8} - \frac{5}{6}\sin^2\theta_W + 2\sin^4\theta_W \cong 0.29 \qquad \text{for } \sin^2\theta_W = 0.25$$

in contrast with the same ratios on an isoscalar target, with the same simplifications:

$$R_\nu = \frac{1}{2} - \sin^2\theta_W + \frac{20}{27}\sin^4\theta_W \cong 0.30$$

$$R_{\bar\nu} = \frac{1}{2} - \sin^2\theta_W + \frac{20}{9}\sin^4\theta_W \cong 0.39 \qquad \text{for } \sin^2\theta_W = 0.25\ .$$

The differences of the cross-section ratios between isoscalar and proton targets are big enough to be tested in experiments even with moderate statistical precision.

Recently, a first measurement of R_ν^p and $R_{\bar\nu}^p$ has been reported by two groups. The experiments have been performed in the FNAL 15′ chamber filled with hydrogen and exposed to a ν and $\bar\nu$ horn-focused WBB.

The Fermilab-Berkeley-Hawaii-Michigan Collaboration[32] has measured, at typical neutrino energies of $\sim$ 25 GeV, a ratio $R_\nu^p = 0.48 \pm 0.17$, where the quoted error does not include the uncertainty of various corrections. The Argonne-Carnegie Mellon-Purdue Collaboration[33] has determined the same ratio in a $\bar\nu$ beam, with the result $R_{\bar\nu}^p = 0.42 \pm 0.13$ where the error includes both statistical and systematic errors.

Unfortunately, while the results are consistent with the expectation from the Weinberg-Salam model, the error bars are too large to allow further conclusions. In this context it is worth mentioning that the CDHS counter experiment will record events originating in a hydrogen tank in front of the iron target, and will make an attempt to measure both R_ν^p and $R_{\bar\nu}^p$ with good precision.

5.4 Measurement of R_ν and $R_{\bar\nu}$ in inclusive neutrino scattering on isoscalar targets

Neutral current reactions have been discovered[20] in the inclusive scattering process. After a period of confirmation and first exploration, inclusive NC experiments have now entered the stage of detailed analysis.

Two things are of crucial importance for high-precision NC experiments: large statistics and good acceptance for final-state muons, if there are any. If also differential cross-sections are to be studied, NBB kinematics, with the advantage of the known energy-radius relation, is almost indispensable. However, the over-all cross-section ratios $R_\nu = (NC/CC)_\nu$ and $R_{\bar\nu} = (NC/CC)_{\bar\nu}$ can be determined without major problems also in WBB.

The experiment which has so far given the most precise information is that of the CDHS Collaboration[34]. The basic criterion for separating NC from CC events is the "event length", i.e. the distance measured in centimetres of iron, between the start and the end of the event as given by the scintillator pattern, projected onto the axis of the detector. This method has already been used successfully in an early experiment of the CITF Collaboration[35] demonstrating unambiguously an excess of events at short event lengths, which is ascribed to NC events. The advantage of the method is that no reconstruction of the muon track (if any) is involved, and therefore problems of reconstruction inefficiency are *a priori* avoided.

Neutral current events are only detectable if a minimum amount of hadronic energy E_H is dissipated. Different cut-offs at low E_H are applied in different experiments in order to ensure that the detection efficiency for E_H above the cut-off is unity. The effect of the cut-off is more severe for the low-energy GGM data compared to data taken in the 100 GeV domain.

The resulting event-length distributions for ν and $\bar\nu$ events are shown in Fig. 24 for CITF and Fig. 25 for CDHS. The general features are the same. However, the CDHS data sample is larger by one order of magnitude, and the background of CC events with stopping low-energetic muons or with muons escaping at the side is greatly reduced, thanks to the large lateral dimensions of the CDHS detector.

A major source of systematic uncertainty comes from the WBB background which is unavoidably present in NBB. It has been determined empirically in both experiments in special runs with the momentum-defining collimator closed. The CC subtraction in the NC signal region has been performed in the CDHS experiment by means of a Monte Carlo extrapolation on the basis of the number of events found in the "monitor region" (see Fig. 25). Note that this means virtually an extrapolation of CC events from large y to y = 1, since large-y CC events constitute the bulk of the events in the monitor region after the subtraction of WBB events. The CC y-distribution is essentially flat at large y, both for ν and $\bar{\nu}$, in the latter case as a consequence of the finite amount of antiquark scattering showing up as a flat component in the y-distribution. This is the reason why the CC subtraction is insensitive to the actual amount of antiquarks, since the subtraction is based on the observed number of events in the monitor region, with very little uncertainty in the extrapolation.

Another feature of the analysis is equally important, both for CDHS and CITF: any contribution from "prompt" new phenomena originating possibly in the target and giving rise to "false" muonless events (see Section 7) is avoided when subtracting the properly scaled event numbers recorded in closed-collimator runs.

The results of the most recent experiments on R_ν and $R_{\bar{\nu}}$ are summarized in Table 7, and shown in Fig. 26 together with the expectation from the Weinberg-Salam model. The graphical comparison of Fig. 26 is not completely fair, since the E_H cut-off corrections are applied for only part of the experiments, and the Weinberg-Salam prediction depends slightly on the amount of antiquarks as well as on small deviations from isoscalarity of the targets used. The curve in Fig. 26 is drawn for the conditions of the CDHS experiment. Note that a small change of α, the relative amount of antiquarks, has very little effect on the determination of $\sin^2 \theta_W$ from R_ν. In fact, R_ν mainly determines $\sin^2 \theta_W$ and its precision. The value of α which has been used in the CDHS analysis was $\alpha = 0.10$. As discussed in Section 4, $\alpha \simeq 0.17$ seems to be more appropriate for high energies. However, the quoted error of 0.02 on $\sin^2 \theta_W$ covers the range $0.05 < \alpha < 0.20$ (the statistical error on $\sin^2 \theta_W$ is only one third of the quoted over-all error).

Table 7

Summary of most recent experiments results on R_ν, $R_{\bar\nu}$, and $\sin^2\theta_W$ from inclusive neutrino scattering on isoscalar targets

Experiment	Beam	⟨Energy⟩ (GeV)	R_ν and $R_{\bar\nu}$	E_H cut-off	$\sin^2\theta_W$
GGM[36]	WBB	2 "	$R_\nu = 0.26 \pm 0.04$ $R_{\bar\nu} = 0.39 \pm 0.06$	Corrected	0.32 ± 0.05
HPWF[37]	WBB	85 40	$R_\nu = 0.29 \pm 0.04$ $R_{\bar\nu} = 0.39 \pm 0.10$	$E_H > 4$ GeV	0.23 ± 0.06
CITF[38]	NBB	90 70	$R_\nu = 0.28 \pm 0.03$ $R_{\bar\nu} = 0.35 \pm 0.11$	$E_H > 12$ GeV	0.33 ± 0.07 *)
CDHS[34]	NBB	100 90	$R_\nu = 0.293 \pm 0.010$ $R_{\bar\nu} = 0.35 \pm 0.03$	$E_H > 12$ GeV	0.24 ± 0.02
BEBC[39] (preliminary)	NBB	100 90	$R_\nu = 0.32 \pm 0.04$ $R_{\bar\nu} = 0.38 \pm 0.07$	$E_H > 15$ GeV	0.21 ± 0.04 (statistical error only)

*) Determined from an over-all fit including normalized E_H spectra.

As can be seen from Table 7 and Fig. 26, all recent experiments are in reasonable agreement. They point to a value of $\sin^2\theta_W$ near to 0.25, which is just the singular value for pure leptonic interactions as discussed in Section 5.1. The most precise value for $\sin^2\theta_W$ comes from the CDHS experiment, and is

$$\sin^2\theta_W = 0.24 \pm 0.02 \ .$$

A graphical comparison of the results of different experiments for $\sin^2\theta_W$ is shown in Fig. 27.

The apparent difference in the result for $\sin^2\theta_W$ between CDHS and CITF (although the ratios R_ν and $R_{\bar\nu}$ appear to be almost identical) is due to the fact that CITF has determined $\sin^2\theta_W$ in an over-all fit which has included the observed distributions in E_H (this offers additional information on $\sin^2\theta_W$, see Section 5.5) from CC and NC, with an external flux normalization of ν and $\bar\nu$ events. Determining $\sin^2\theta_W$ directly from R_ν and $R_{\bar\nu}$ would of course give a $\sin^2\theta_W$ closer to the CDHS value.

The striking feature in Table 7 is that the R_ν and $R_{\bar{\nu}}$ values from GGM show no significant difference from the high-energy values, although determined with low-energy neutrinos. Note, however, that $\sin^2 \theta_W$ has been determined from the GGM data assuming the energy to be below the charm threshold, in contrast to the analyses of the high-energy experiments.

5.5 Hadron energy distributions of inclusive neutral current events

The E_H-distribution of neutral current events reflects the NC y-distribution, folded with the neutrino energy spectrum. Hence, the y-distribution can be inferred from the E_H-distribution.

In practice, the best study of E_H-distributions can be done in a NBB because for a given radius slice the incident neutrino energy is dichromatic (owing to the π/K ambiguity), and the y-distribution is transparent in the observed E_H-distribution. In a WBB, however, owing to the lack of an energy-radius correlation, the neutrino energy spectrum is unavoidably folded into the observed E_H spectrum, thus making the interplay between a possible energy dependence of the NC cross-section and the form of the y-distribution irresolvable. However, assuming R_ν and $R_{\bar{\nu}}$ to be energy independent, the parameters of the NC y-distribution can be determined by an unfolding procedure also in WBB.

So far, the only experiment which has reported statistically meaningful results on the separate study of ν and $\bar{\nu}$ NC y-distributions is the CDHS experiment[40]. The results have been obtained in a NBB. The E_H-distributions of NC and CC events are shown in Figs. 28a and 28b. To avoid a direct comparison with Monte Carlo events for which a very good understanding of the hadron energy calibration and of all resolution effects is necessary, the ratio of the NC and CC E_H-distributions in each radial bin, as a function of E_H, has been studied. This has the advantage that systematic errors are greatly reduced, and the primary aim of the study -- to look for a difference of the NC y-distribution with respect to the CC y-distribution -- is more transparent. As can be seen from Fig. 28, the NC E_H-distribution follows very closely the CC E_H-distribution. It can immediately

be concluded that the NC and CC y-distributions do not differ greatly and that there is no substantial energy dependence of R_ν and $R_{\bar{\nu}}$.

The ratios of the NC and CC E_H-distributions are shown in Figs. 29a and 29b. If R_ν and $R_{\bar{\nu}}$ are independent of energy, and the NC and CC y-distributions are the same, all ratios must be compatible with being constant in all radius bins. This is nearly the case, but there is a visible trend towards a gentle deviation from the constant. The ν and $\bar{\nu}$ data have been fitted independently, with a functional form for the y-distribution as follows:

$$\frac{NC}{CC}(y) = R_0 \frac{1 + \alpha_{NC}(1 - y)^2}{1 + \alpha_{CC}(1 - y)^2} \quad \text{for } \nu$$
$$= \bar{R}_0 \frac{(1 - y)^2 + \bar{\alpha}_{NC}}{(1 - y)^2 + \alpha_{CC}} \quad \text{for } \bar{\nu} \,. \tag{23}$$

This particular parametrization comes from the prejudice that the NC has a V,A structure, together with the assumption of approximate scaling behaviour. It finds its *a posteriori* justification from the close similarity of the NC and CC E_H-distributions.

The input CC y-distribution consists only of components with flat y and $(1 - y)^2$, which is a reasonable parametrization of the data (see Section 4.2). The parameter α_{CC} has been chosen to be 0.10, independent of energy. However, as long as conclusions are based on the difference between NC and CC E_H-distributions, the results are almost independent of the chosen value of α_{CC}.

The first result which can be obtained is R_ν and $R_{\bar{\nu}}$ without cut-off in E_H. This means, in practice, that the parametrization [Eq. (23)] is taken to be valid also for the undetected NC events with $E_H < 12$ GeV. Integrating Eq. (23) with the best-fit values for R_0 ($\bar{R}_0$) and α_{NC} ($\bar{\alpha}_{NC}$), the result is

$$\left.\begin{aligned} R_\nu &= R_0 \frac{1 + \frac{1}{3}\alpha_{NC}}{1 + \frac{1}{3}\alpha_{CC}} = 0.295 \pm 0.010 \\ R_{\bar\nu} &= \bar R_0 \frac{\frac{1}{3} + \bar\alpha_{NC}}{\frac{1}{3} + \alpha_{CC}} = 0.34 \pm 0.03 \end{aligned}\right\} \begin{array}{l} E_H > 0 \text{ GeV}, \\ \alpha_{CC} = 0.10 \ . \end{array}$$

The corrected values for R_ν and $R_{\bar\nu}$ point to a steeper NC y-distribution for ν and a flatter distribution for $\bar\nu$, compared to the CC y-distribution.

In a NBB with its radius-energy correlation it is possible to study the energy-dependence of R_ν and $R_{\bar\nu}$. For this purpose, the parameters R_0 and $\bar R_0$ are split into two energy bins, $E_\nu < 100$ GeV and $E_\nu > 100$ GeV, but with an energy-independent y-distribution. The result is

$$R_\nu(E_\nu > 100 \text{ GeV})/R_\nu(E_\nu < 100 \text{ GeV}) = 0.99 \pm 0.07$$

$$R_{\bar\nu}(E_{\bar\nu} > 100 \text{ GeV})/R_{\bar\nu}(E_{\bar\nu} < 100 \text{ GeV}) = 1.03 \pm 0.18 \ .$$

This result does not favour a substantial energy dependence of R_ν ($R_{\bar\nu}$). The average neutrino energy is 60 GeV below and 150 GeV above 100 GeV. The result is illustrated in Fig. 30.

The shape of the NC y-distribution is characterized by α_{NC} ($\bar\alpha_{NC}$). Note, however, that the absolute value of α_{NC} ($\bar\alpha_{NC}$) is meaningless since it depends strongly on the input assumption for α_{CC}. The result is therefore quoted as the difference between α_{NC} ($\bar\alpha_{NC}$) and α_{CC}:

$$\left.\begin{aligned} \alpha_{NC} - \alpha_{CC} &= 0.09 \pm 0.18 \\ \bar\alpha_{NC} - \alpha_{CC} &= 0.10 \pm 0.07 \end{aligned}\right\} \text{ with } \alpha_{CC} = 0.10 \ .$$

Hence, the best fit favours a NC y-distribution which is steeper for ν and flatter for $\bar\nu$, compared to the CC y-distribution, although the difference is of course statistically not significant. The result is illustrated in Fig. 31. It is a great challenge to experimenters to reduce the experimental error so that

the indicated difference becomes significant. For this it is of prime importance to further increase the statistics of NC events, in particular for $\bar{\nu}$ where a flatter y-distribution can more easily be established.

In NC reactions the outgoing neutrino is unobserved, and it is not *a priori* clear that the incoming and outgoing neutrinos are identical. If both neutrinos are identical, the effective Lagrangian is proportional to $\bar{\nu}\gamma_\lambda(1 + \gamma_5)\nu \cdot j_H^\lambda$, where the space and time components of the hadronic current are required to be Hermitian since the Lagrangian is believed to be Hermitian on very general grounds. Hence the differential cross-sections must be the same for ν and $\bar{\nu}$ wherever the VA interference term vanishes, e.g. at $y = 0$. On the other hand, with two different neutrinos it is possible to consider non-Hermitian hadronic neutral currents, with the result that the ν and $\bar{\nu}$ cross-sections at $y = 0$ are not necessarily the same. The argument is due to Wolfenstein[41]. The experimental result for the forward cross-section ratios at $y = 0$ is:

$$R_0 \frac{1 + \alpha_{NC}}{1 + \alpha_{CC}} = 0.313 \pm 0.033$$

$$\bar{R}_0 \frac{1 + \bar{\alpha}_{NC}}{1 + \alpha_{CC}} = 0.297 \pm 0.034 ,$$

or

$$\left[R_{\bar{\nu}}/R_\nu\right]_{y=0} = 0.95 \pm 0.15$$

on an iron target. This result, together with the experimentally established charge symmetry for CC interactions, is in agreement with the concept of "neutrino identity" (but does not necessarily prove it).

5.6 The space-time structure of neutral currents

The space-time structure can be explored via the NC y-distribution. However, this is strictly true only in the scaling limit, because in the general case [see Eq. (1)] the y-distribution does not factorize. But if scaling holds at least approximately, which has been demonstrated in CC scattering results, the

y-dependence of the differential NC cross-section becomes explicit and indicative of the NC space-time structure. On general grounds it can then be at most a second-order polynomial in y.

In order to get statistically meaningful results on the NC space-time structure, the CDHS group[40] has performed a common fit of the ν and $\bar{\nu}$ data sets, with only two fit parameters which interchange their place when changing from ν to $\bar{\nu}$. Thus the errors on the fit parameters are greatly reduced compared to all fits discussed in the previous section, where ν and $\bar{\nu}$ data have been independently fitted, each data set with two fit parameters. Since the simple parametrization [Eq. (23)] is not adequate for the statistical accuracy of the total data sample, the parametrization is refined by taking into account the small effects of the strange sea and the deviation of iron from an isoscalar target:

$$\frac{NC}{CC}(y) = \frac{g_L + g_R(1-y)^2 \left[+g_{SP}y^2\right]}{f_L + f_R(1-y)^2} \quad \text{for } \nu$$

$$= \frac{g_L(1-y)^2 + g_R \left[+g_{SP}y^2\right]}{\bar{f}_L(1-y)^2 + \bar{f}_R} \quad \text{for } \bar{\nu}\ , \tag{24}$$

where g_L and g_R denote the effective contributions from left- and right-handed NC for a target of iron nuclei; g_L and g_R are the same for ν and $\bar{\nu}$ NC interactions, whereas the equivalent CC parameters are slightly different for ν and $\bar{\nu}$:

$$f_L = 1 + \delta + \xi_s = 1.05$$
$$f_R = \xi_{ud} = 0.07$$
$$\bar{f}_L = 1 - \delta = 0.98$$
$$\bar{f}_R = \xi_{ud} + \xi_s = 0.10$$

with

$$\delta = \frac{1}{3}\frac{N-Z}{N+Z} = 0.023 \qquad \text{for iron (non-isoscalar correction)}$$

$$\xi_{ud} = \frac{\int x(\bar{u}+\bar{d})dx}{\int x(u+d)dx} \qquad \text{taken to be 0.07 (non-strange sea)}$$

$$\xi_s = \frac{\int x 2\bar{s}dx}{\int x(u+d)dx} \qquad \text{taken to be 0.03 (strange sea)}\ .$$

The such defined parameters f_L, f_R, $\bar{f}_L$, and $\bar{f}_R$ have been used as input parameters in the fit, for the description of the y-distribution of CC interactions on iron nuclei. The relative amount of strange plus non-strange sea is assumed to be $\xi_s + \xi_{ud} = 0.03 + 0.07 = 0.10$.

The S or P couplings, in the presence of V,A terms, would show up as a y^2 term in the NC y-distribution, with same strength for ν and $\bar{\nu}$. In Eq. (24), the best fit for g_{SP} yields the result

$$\frac{g_{SP}}{g_L + g_R} = 0.02 \pm 0.07 \ ,$$

which does not favour the presence of S or P terms in the NC structure. However, this interpretation is only valid if there is no intrinsic (1 - y) term present (a longitudinal contribution analogous to the one discussed for CC in Section 3). A y^2 term could also be indicative of a (1 - y) term, although the coefficient of the y^2 term is then negative*).

In the quark-parton model, g_L is to be interpreted as the sum of the contributions of the V-A current from quarks, and the V+A current from antiquarks, with the reverse true for g_R. The result for g_L and g_R is

$$\left.\begin{aligned} g_L &= 0.300 \pm 0.012 \\ g_R &= 0.050 \pm 0.005 \end{aligned}\right\} \text{ with } \xi_{ud} + \xi_s = 0.10 \ .$$

It should be stressed, however, that these values of g_L and -- in particular -- g_R are dependent on the input assumption on $\xi_{ud} + \xi_s$, and are subject to small changes if a higher input value for the sea is used. For this reason, the intensities of the V-A and V+A couplings have not been quoted since they are meaningful only once the amount of sea is known with very good precision.

---

*) I thank Prof. M. Gourdin for having pointed this out to me.

Nevertheless, to demonstrate a significant contribution of V+A coupling besides the dominant V-A contribution, the ratio $g_R/g_L = 0.167 \pm 0.018$ is compared with the one which can be expected for pure V-A coupling of the NC, namely

$$\left[g_R/g_L\right]^{\text{pure V-A}} = \frac{\int x(\bar{u} + \bar{d} + \bar{s})dx}{\int x(u + d)dx} = 0.07 + \frac{0.03}{2} = 0.085 ,$$

with the assumptions stated above (which entered also into the results for g_L and g_R!). This result is in disagreement with a pure V-A structure of the NC, and requires a V+A admixture with a significance of 4 standard deviations (6 standard deviations statistical error only). This significance is fairly independent of the assumption for $\xi_{ud} + \xi_s$ in the range $0.05 < \xi_{ud} + \xi_s < 0.20$.

A graphical illustration of this result is given in Fig. 32. It shows clearly the significance of the result in discriminating between different hypotheses for the NC space-time structure. The hypotheses of V+A and pure V or A are completely ruled out, confirming earlier but less precise results[36-38]. The question today is to establish firmly the small V+A contribution of the weak NC.

Figure 33 shows the analogous CITF result. The experiments agree on their conclusions although CITF tends to a higher relative contribution of the right-handed NC component.

As can be seen in both Figs. 31 and 32, the data are in good agreement with the Weinberg-Salam model. The value of $\sin^2 \theta_W = 0.24 \pm 0.02$ derived from the CDHS values of R_ν and $R_{\bar{\nu}}$ describes very well also the observed E_H distributions, both for ν and $\bar{\nu}$, as can be seen in Fig. 29. Performing a fit in the framework of the Weinberg-Salam model with both $\sin^2 \theta_W$ and the sea $\xi_{ud} + \xi_s$ as unknowns, the best fit yields $\xi_{ud} + \xi_s = 0.16 \pm 0.05$, with $\sin^2 \theta_W$ unchanged. This result for the sea, although obtained in the framework of a very specific model, is well consistent with $\alpha = 0.17 \pm 0.06$ obtained from CITF CC data (see Section 4.2).

5.7 Upper limits for strangeness- and charm-changing neutral currents

In the Weinberg-Salam model, extended by the GIM model to incorporate the weak CC and NC interactions of quarks, the weak hadronic current is, by construction [see Eq. (21)], strangeness- and charm-conserving. Experimental tests of this conjecture have been reported.

The conservation of strangeness by neutral weak currents has been verified experimentally with very good precision in the decay of strange particles. For neutrino reactions, the GGM group[42] has examined a sample of about 10,000 ν NC events for single strange particle production. No signal has been found for Λ or Σ^0 production, yielding an upper limit

$$\frac{\sigma[\nu + N \to \nu + \Lambda(\text{or } \Sigma^0) + \text{non-strange hadrons}]}{\sigma(\nu + N \to \nu + X)} < 5.4 \times 10^{-3}$$

at the 90% confidence level.

At neutrino energies in the 100 GeV domain, where the production of massive charmed particles is not kinematically suppressed, the CDHS experiment[43] has reported an upper limit for charm production by NC by examining "wrong-sign" events in a ν NBB. Suppose a charm-changing NC converts a u-quark into a c-quark, $\nu + u \to \nu + c$, which in turn decays semileptonically, $c \to s + \mu^+ + \nu$, resulting in a wrong-sign muon. All the events found can be attributed to known sources of background, mainly WBB background. A cut at a visible energy greater than 100 GeV leaves one event which is most likely due to background, giving an upper limit for charm-changing NC,

$$\frac{\sigma(\text{NC with } \Delta C = 1)}{\sigma(\text{NC with } \Delta C = 0)} < 2.6 \times 10^{-2}$$

at the 90% confidence level. This limit can also be interpreted as an upper limit to the fraction of the charmed sea in the nucleon.

5.8 The isospin structure of the weak neutral current

Starting with the prejudice that the weak NC does not change isospin by more than one unit ($|\Delta I| < 1$) -- motivated by analogy to the isospin structure of both the CC weak current and the electromagnetic current -- the NC can contain only isoscalar ($\Delta I = 0$) and isovector ($\Delta I = 1$) terms. The single-pion production in neutrino interactions is one of the simplest reactions for investigating the isospin structure.

The GGM group[44] has recently reported measurements of all four possible NC-induced exclusive single-π channels. They are listed in Table 8 together with the respective transition amplitudes and the measured cross-sections given in arbitrary units.

Table 8

Transition amplitudes and cross-sections for all four neutral current single-π production channels

Reaction channel	Transition amplitude	Cross-section (arbitrary units)
$\nu + p \to \nu + p + \pi^0$	$2A_3 + A_1 - S$	297 ± 37
$\nu + n \to \nu + n + \pi^0$	$2A_3 + A_1 + S$	177 ± 43
$\nu + n \to \nu + p + \pi^-$	$\sqrt{2}(A_3 - A_1 - S)$	237 ± 59
$\nu + p \to \nu + n + \pi^+$	$\sqrt{2}(A_3 - A_1 + S)$	180 ± 31

S = isoscalar amplitude
A_1 = isovector $\frac{1}{2}$ amplitude
A_3 = isovector $\frac{3}{2}$ amplitude

Three isospin amplitudes can contribute to exclusive single-π production: the amplitudes S (isoscalar) and A_3 (isovector $\frac{1}{2}$) lead to a final-state π-nucleon system with $I = \frac{1}{2}$. The amplitude A_3 (isovector $\frac{3}{2}$) leads to a final state with $I = \frac{3}{2}$. Five real quantities (one over-all phase can be arbitrary) cannot be determined from the measured cross-sections since the system is under-determined. However, extreme hypotheses can be tested:

a) The weak hadronic current is pure isoscalar ($A_1 = A_3 = 0$) or pure isovector $\frac{1}{2}$ ($S = A_3 = 0$): then one expects the ratio of cross-sections $(p\pi^0):(n\pi^0):(p\pi^-):(n\pi^+) = 1:1:2:2$. This expectation is incompatible with the observed cross-sections and is ruled out with a confidence level $< 10^{-4}$.

b) The weak hadronic current is pure isovector $\frac{3}{2}$ ($S = A_1 = 0$): then one expects the ratio of cross-sections $(p\pi^0):(n\pi^0):(p\pi^-):(n\pi^+) = 2:2:1:1$. This expectation is, although not incompatible, still very unlikely: the confidence level is only 0.02.

Moreover, a survey of the π-nucleon mass spectra exhibits a peak in the $(p\pi^0)$ channel which is due to Δ production (see Fig. 34). This observation makes an A_3 component necessary and favours its dominance in a mixture of isoscalar and isovector components.

The main conclusion of the analysis (which is very difficult, since a detailed understanding of nuclear re-interactions is crucial), i.e. that the weak hadronic NC is composed of an isoscalar and an isovector term, is supported by other measurements of the GGM group: the exclusive single-π production in $\bar{\nu}$ NC interactions, and the semi-inclusive single-π production in NC ν and $\bar{\nu}$ interactions[45].

Finally, the experimental results on the isospin structure of the weak hadronic current are in agreement with the expectation from the Weinberg-Salam model. However, the experimental error bars are unfortunately too large to enable a critical test to be made.

6. MULTILEPTON EVENTS

The discovery of neutrino-induced 2μ events has been one of the most interesting developments in neutrino physics in the past few years. They have provided direct experimental evidence for the excitation of a new hadronic degree of freedom, which was subsequently identified with charm. Recently, the discovery of neutrino-induced events with even higher muon multiplicity has again caused considerable efforts to be made to understand the origin of these events.

6.1 Opposite-sign 2μ events

Events with 2μ in the final state were first reported by the HPWF group[46] and have been confirmed by the CITF group[47]. Both groups have made a big effort to explore the nature of both opposite-sign and like-sign 2μ events[48,49]. This early work demonstrated that the opposite-sign 2μ events are mainly due to the production and subsequent semileptonic decay of charmed particles. However, the nature of like-sign and $\bar{\nu}$-induced opposite-sign 2μ events has remained unclear owing to lack of statistics.

The CDHS group[50] has reported a study of ν- and $\bar{\nu}$-induced opposite-sign 2μ events, where the statistics of events with all relevant kinematical parameters measured has been increased by an order of magnitude. Since the data have been recorded in a NBB, the total visible energy can be compared to the incident ν energy reconstructed from the known radial position of the event. Thus a check for missing energy carried away by unobserved final-state neutrinos is possible.

The conclusion from the characteristics of a sample of 257 ν- and 58 $\bar{\nu}$-induced opposite-sign 2μ events is, in line with the earlier work, that these events are predominantly due to charm production, with properties just as expected from the GIM charm model[31]. Within the statistical accuracy of the data sample, no other mechanism is needed in order to explain the events.

In the GIM charm model, the production and subsequent semileptonic decay of charmed quarks can occur in different reaction channels. They are listed in Table 9 together with the resulting expectations for the rate and for the x- and y-distributions. One therefore expects the data to exhibit the following properties:

a) The 2μ events occur in ν and $\bar{\nu}$ interactions, with a comparable strength.

b) For ν, the scattering takes place both on valence- and sea-quarks. The x-distribution should be slightly compressed towards smaller x compared to normal CC interactions. For $\bar{\nu}$, the scattering takes place exclusively from sea-quarks, and almost only from the strange-quark component. The x-distribution then represents the structure function of the (strange) sea.

Table 9

Possible processes for opposite-sign dilepton production for ν and $\bar{\nu}$

$$\xi_{ud} = \frac{\int x(\bar{u} + \bar{d})dx}{\int x(u + d)dx} \; ; \quad \xi_s = \frac{\int x 2\bar{s}dx}{\int x(u + d)dx} \; ; \quad \ell = \mu \text{ or } e$$

Process	Relative rate	Scattering occurs off:	y-distribution
$\nu + d \to \mu^- + c$	$\sin^2 \theta_C \sim 0.05$	Valence-quarks	Flat
$\nu + s \to \mu^- + c$ (with $c \to s + \ell^+ + \nu$)	$\xi_s \cos^2 \theta_C \sim 0.04$	Sea-quarks	Flat
$\bar{\nu} + \bar{d} \to \mu^+ + \bar{c}$	$\xi_{ud} \sin^2 \theta_C \sim 0$	Sea-quarks	Flat
$\bar{\nu} + \bar{s} \to \mu^+ + \bar{c}$ (with $\bar{c} \to \bar{s} + \ell^- + \bar{\nu}$)	$\xi_s \cos^2 \theta_C \sim 0.04$	Sea-quarks	Flat

c) The y-distribution is also flat for $\bar{\nu}$ interactions. Hence on the average, half of the ν energy is transferred to the hadron system. The second muon comes from the decay of a particle which is only part of the shower. As a consequence, one typically expects a high-energy "leading" muon from the lepton vertex opposed to a low-energy second muon, with a strong anti-correlation in the azimuthal angle difference $\Delta\phi$ of the momentum projections on the plane perpendicular to the direction of the incident neutrino.

d) The transverse momentum of the second muon is limited with respect to the shower direction, calculated from the difference of the vector momenta of the incident neutrino and the leading muon.

e) Owing to the unobserved neutrino from the semileptonic decay of the charmed particle, the visible energy is smaller than the reconstructed incident energy.

All these features are well reproduced by the data. Figure 35 shows the scatter plot of the energies of the leading and second muons. The average energy of the leading muon is three times larger than the average energy of the second

muon, well outside the Pais-Treiman bound[51] $0.48 < \langle E_{\mu 1} \rangle / \langle E_{\mu 2} \rangle < 2.10$ for the creation of a neutral heavy lepton with spin $\frac{1}{2}$, which could be an alternative explanation of opposite-sign 2μ events. Note that the momentum of the muons is required to be > 4.5 GeV on the average, to enable an unambiguous muon identification and the reconstruction of the vector momentum. Thus the "true" ratio without cut-off will be even higher.

Figure 36 shows the anticorrelation of the two muons in a scatter plot of $\Delta\phi$ and the energy of the second muon. This plot demonstrates clearly the association of the second muon with the shower direction. This association becomes even more pronounced with the increasing energy of the second muon.

Figure 37 shows clearly the limited transverse momentum p_T of the second muon with respect to the direction of the hadron shower, independent of the energy of the second muon. Figure 38 demonstrates the behaviour expected from GIM charm in the distributions of the scaling variables x and y. The y-distributions are consistent with a flat distribution, the x-distributions are compressed towards small x, in particular for $\bar{\nu}$ events. The observed x-distribution for $\bar{\nu}$ events is compatible with the one observed in antineutrino CC single-muon events for large y (see Section 4.3), strongly supporting the notion that the antiquarks are concentrated at small x, with a distribution as given in Fig. 38b.

A significant difference between the observed energy and the incoming energy is measured: for ν, 8 ± 4% (for $\bar{\nu}$, 10 ± 5%) of the total energy is carried away by unobserved neutrinos.

Figure 39 shows the rate of the opposite-sign 2μ events [after correction for $\pi(K) \to \mu$ background] as function of the incident ν energy, normalized to the rate of single-muon CC events. The increase of the rate with energy reflects the improving acceptance to observe the events in a charm model. The acceptance is essentially the probability that the muon from charm decay exceeds the cut of 4.5 GeV. Above 100 GeV, the observed rate is

$$\frac{\sigma(\mu^+\mu^-)}{\sigma(\text{single } \mu)} \cong 5 \times 10^{-3} \quad (E_\nu > 100 \text{ GeV})$$

with a 2μ acceptance of about 50%. The observed rates are smoothly dependent on energy, with no significant indication for a threshold effect because of a substantial production of a new sort of hadronic matter beyond charm.

The observed ν and $\bar{\nu}$ rates can be used to calculate the magnitude of the strange sea on the basis of the relations given in Table 9:

$$\xi_s = \frac{\int x(2\bar{s})dx}{\int x(u + d)dx} = \tan^2 \theta_C \frac{\sigma^{\bar{\nu}}}{\sigma^{\nu}} \frac{1}{\left[R(2\mu)/\bar{R}(2\mu)\right] - (\sigma^{\bar{\nu}}/\sigma^{\nu})} .$$

With $\tan^2 \theta_C = 0.057$, $R(2\mu)/\bar{R}(2\mu) = 1.05$, and $\sigma^{\bar{\nu}}/\sigma^{\nu} = 0.48$ (see Section 4.1), we get for the momentum fraction of the quarks of the strange sea $\xi_s \cong 0.05$. Taking the present world average for the semileptonic branching ratio for charmed mesons[52], $B_\mu = 9\%$, and a rate $\sigma(2\mu)/\sigma(\mu) = 5 \times 10^{-3}$ with an acceptance of 50%, we arrive at the result that $\sim$ 11% of the total CC cross-section is accounted for by charm production at high energies, both for ν and $\bar{\nu}$.

When comparing the opposite-sign 2μ sample with models of charm production, information can be extracted about the fragmentation function D(z) of the charmed quark, where

$$z = \frac{2p_D^*}{\sqrt{W^2 - (M + M_D)^2}}$$

is the function of the available centre-of-mass momentum carried by the charmed D meson [W denotes the invariant hadron mass, M is the nucleon mass, and M_D is the mass of the D(1870) meson]. The choice of a flat or slightly increasing function of z, which can be motivated by leading-particle effects, yields a good description of the data[53] as shown in Fig. 40.

6.2 μe events

The detection of μe events is so far only possible in bubble chambers because of their excellent capability to detect electrons, whereas counter experiments are in general blind in this respect.

The first events with a μ^- in association with an e^+ have been observed by the GGM group[54] and have subsequently been confirmed by the FNAL 15' chamber[55-58]. Recently, the BEBC group[59] has also recorded a number of 2μ and μe events (and even one 3μ event). The characteristics of the μe events are fully compatible with the characteristics of the opposite-sign 2μ events and need not be discussed again. The difference between 2μ and μe events is that the semileptonic decay of the charmed particle yields in one case a muon, in the other case an electron.

Moreover, the bubble chambers found a particularly nice confirmation of the GIM charm picture: there is a strong correlation of μe events with the production of strange particles. This is expected in the GIM model, where the charmed quark couples with a strength of $\cos^2 \theta_C \sim 0.95$ to the s-quark and with $\sin^2 \theta_C \sim 0.05$ to the d-quark.

The charm model can accommodate ~ 1.5 strange particles per μe event for ν, and ~ 2 for $\bar{\nu}$, since two strange particles must be created when producing charm off the sea. Then the expected K^0 multiplicity is about 0.8 per event[60] in the GIM charm model. Unfortunately, different experimental results have not yet yielded a consistent picture, since the reported K^0 multiplicities are not in agreement:

$$\langle n_{K^0} \rangle = 1.84 \, {}^{+\,0.63}_{-\,0.53} \quad \text{(Refs. 55, 56)}$$

$$\langle n_{K^0} \rangle = 0.5 \pm 0.2 \quad \text{(Ref. 57)}$$

$$\langle n_{K^0} \rangle = 1.7 \pm 0.7 \quad \text{(Ref. 59)} \; .$$

This discrepancy is not yet understood. It might be an experimental problem, or it might be due to the energy dependence of the associated strange-particle production. Hence, there is no good reason to give up the GIM charm model, which describes all other features of dilepton events remarkably well.

6.3 Like-sign 2μ events

The existence of like-sign 2μ events and their characteristics are of particular interest in connection with models other than charm production, which

have been proposed to explain the origin of at least part of the opposite-sign 2μ events, and of 3μ events. In particular, some models, constructed to explain certain features of 3μ events, have postulated the existence of heavy lepton cascades. Such a model, for example, would predict a substantial number of like-sign 2μ events with the characteristic property that both muons would be energetic and not associated with the hadron shower. With less speculation, it can be argued that in any case, the 3μ events, whatever their origin might be, must have their reflections in the 2μ events also, most simply when one of the muons is too slow to be detected. Another source which must contribute to like-sign 2μ events at a certain level is associated charm production, with one of the charmed-particle pair decaying semileptonically.

The only statistically meaningful result on like-sign 2μ events has been reported by the CDHS group[61]. It is based on 47 (--) events and zero (++) events recorded in a ν exposure, and on 9 (++) events and zero (--) events in a $\bar{\nu}$ exposure. The data are shown in Fig. 41. The average energy of the second muon (the more energetic muon is chosen as the leading muon) is significantly lower than in the opposite-sign data (compare to Fig. 35). The relative rate of like-sign to opposite-sign 2μ events is about 15%, measured in the very dense (> 5 g/cm^3) CDHS detector. At this level, the problem of trivial background of π(K) → μ decay from shower particles is severe. This background has been calculated on the basis of the known mean free path of pions and kaons in iron, and the properties of ν-induced showers and their subsequent development in matter. The main qualitative features of this background are in agreement with the observed properties of the like-sign 2μ events. One interesting feature is displayed in Fig. 42: the p_T distribution of like-sign 2μ events, where p_T denotes the transverse momentum of the second muon with respect to the plane defined by the leading muon and the incident neutrino (this p_T is on the average smaller by a factor of $\sqrt{2}$ than the p_T with respect to the shower direction, if the second muon is associated with the shower). Figure 42 demonstrates, although with limited statistics, that the second muon is indeed confined to very small p_T, thus pointing clearly to the association of the second muon with the hadron shower.

The Monte Carlo calculated $\pi(K) \rightarrow \mu$ background can only account for $\sim$ 60% of the observed signal, although the systematic uncertainty of such a calculation is difficult to estimate. If the excess of observed events over background is considered significant, then the like-sign 2μ rate which remains after the background subtraction is of the order of $(3 \pm 2) \times 10^{-4}$ of the CC single-μ rate, and of the order of (0.05 ± 0.03) of the opposite-sign 2μ rate, both for ν and $\bar{\nu}$. Much more statistics are needed to pin down a genuine like-sign 2μ signal.

6.4 3μ events

Neutrino-induced 3μ events were first observed by the CITFR group[62]. They have been confirmed by the HPWFR group[63], and later by the CDHS[64] and the BEBC group[59].

A sample of 13 3μ events recorded by the HPWFR group[63,65] (for a long time the largest sample) has caused considerable interest. Some aspects of these early 3μ events have been interpreted by the HPWFR group to be inexplicable by conventional processes[66]. New production mechanisms such as new lepton production and decay cascades have been suggested as the origin of 3μ events.

The data of the HPWFR group have been obtained at FNAL in three different beam types, which are listed in Table 10 together with the observed number of events and the effective number of protons on the target. In the same table are also included the equivalent numbers of the CDHS experiment, which has recorded a substantially larger sample of 3μ events[67]. It seems appropriate to study the dynamics of 3μ events first with the high statistics data sample and then to compare them with the earlier HPWFR results.

The possible sources of 3μ events may be listed as follows:

i) Trivial sources such as

   a) accidental space-time coincidences of a 2μ event and a CC single-μ event. This is estimated to account for at most a few percent of the events observed by CDHS.

Table 10

Comparison of the beams (see also Fig. 2) and event numbers of the HPWFR and CDHS 3μ-event studies

Beam	Sign selection of flux	Proton energy	Effective No. of protons on target	No. of (--+) 3μ events	Experiment
Quadrupole triplet beam	$\nu + \frac{2}{3}\bar{\nu}$	400 GeV	5.8×10^{17}	6	HPWFR
Bare target ν beam	ν (+10% $\bar{\nu}$)		3.3×10^{17}	6	
Bare target $\bar{\nu}$ beam	$\bar{\nu}$ (+10% ν)		18.8×10^{17}	1	
Horn focused WBB + plug	ν (+3% $\bar{\nu}$)	350 GeV	17.0×10^{17}	63	CDHS
Horn focused WBB + plug	ν (+3% $\bar{\nu}$)	400 GeV	2.3×10^{17}	13	

b) $\pi(K) \rightarrow \mu$ decay in addition to 2μ events. This is estimated for the dense CDHS detector to yield of the order of 6 $\mu^-\mu^-\mu^+$ and 6 $\mu^-\mu^+\mu^+$ events (note that this source is about symmetric in the $\mu^-\mu^-\mu^+$ and $\mu^-\mu^+\mu^+$ signature). The numbers actually observed were 76 $\mu^-\mu^-\mu^+$ events and 4 $\mu^-\mu^+\mu^+$ events. The observed 4 events of the latter type are consistent with this background, and will not be discussed further. However, it is clear that a genuine $\mu^-\mu^-\mu^+$ signal exists above trivial background.

ii) Non-trivial but conventional sources such as

a) production and subsequent decay of vector mesons into $\mu^+\mu^-$ pairs;

b) electromagnetic $\mu^+\mu^-$-pair production both from the final-state μ at the lepton vertex and from the quarks at the hadron vertex;

c) associated production and subsequent semileptonic decay of charmed particles;

d) internal $\mu^+\mu^-$-pair creation after $q\bar{q}$ annihilation (Drell-Yan process).

iii) Exotic sources such as production and subsequent cascade decay of new heavy leptons, or heavy quarks, or both together.

Apparently, the bulk of the listed conventional processes yields an additional $\mu^+\mu^-$ pair which is associated with the hadron vertex. To explore this possibility, the CDHS group has defined a "leading" negative muon (μ_1) such that the sum of the absolute values of the transverse momenta of the second negative muon (μ_2) and of the positive muon (μ_3) with respect to the direction of the hadron shower ($\vec{\nu} - \vec{\mu}_1$) is minimal.

The momentum distribution of the three muons exhibits a clear distinction between the leading and the non-leading muons (Fig. 43). The average energy of the leading muon is a factor of 2 higher than the average energies of the non-leading muons. On the other hand, the two non-leading muons appear to be rather symmetric, as shown in Fig. 44.

The fact that for nearly all events the transverse momenta of the non-leading muons with respect to the direction of the hadron shower (calculated as $\vec{\nu} - \vec{\mu}_1$) are confined to small values, is shown in Fig. 45. The observed $\langle p_T \rangle$ is close to the one observed for the second muon in opposite-sign 2μ events ($\sim$ 700 MeV).

At this stage the tendency of the non-leading muons to be dominantly associated with the shower is already clear. This notion is confirmed in Fig. 46, where the difference $\Delta\phi$ in the azimuthal angles of the projections of the muons on the plane perpendicular to the incident neutrino is shown. To be less affected by measurement errors, events are plotted only when all transverse momenta with respect to the direction of the incident neutrino are greater than 200 MeV. The distributions in $\Delta\phi$, for both combinations of a leading with a non-leading μ, peak at 180°, pointing clearly to a dominantly hadronic origin of the events. If both non-leading μ's have a common parent particle, it is meaningful to look for the distribution of $\Delta\phi$ between the leading μ and the vectorial sum of the two non-leading μ's. This distribution (Fig. 46c) peaks even more sharply at 180°. However,

a significant number of events cluster around $\Delta\phi = 0°$. This indicates that not all the secondary muons are associated with the shower.

The mass plots (Figs. 47a-d) show rather smooth distributions. The non-leading dimuon mass is significantly compressed to smaller values. Unfortunately, the mass resolution is not good enough to clearly resolve peaks from, for example, ρ production.

The scatter plot of the three possible dimuon masses versus the 3μ mass is shown in Fig. 48. Figure 48a shows the two possible $\mu^+\mu^-$-pair mass combinations. As the 3μ mass increases, the dimuon masses separate into two bands, one rising linearly with the 3μ mass, the other being confined to small values. Note that with the chosen definition of the leading muon, the non-leading dimuon mass is always in the lower band. In contrast to that, the dimuon masses containing the leading muon lie close to the kinematical upper bound which is given by the 3μ mass. From this plot it can be concluded that the parent mass of the non-leading dimuons must be rather small.

The distribution of the visible energy spectrum is given in Fig. 49 for single-μ CC, for opposite-sign 2μ, and for 3μ events. The distribution for 3μ events is smooth and does not exhibit a threshold effect. Figure 50 shows the 3μ rate compared to the single-μ CC rate, as function of visible energy. The raw rate (i.e. uncorrected for acceptance) of 3μ events to single-μ CC events is, for visible energy above 30 GeV,

$$\frac{\sigma(3\mu)}{\sigma(\text{single }\mu)} = (3.2 \pm 0.4) \times 10^{-5} \quad (350 \text{ GeV WBB})$$

$$= (5.0 \pm 1.5) \times 10^{-5} \quad (400 \text{ GeV WBB}) \,.$$

The rate increases from $(1.2 \pm 0.3) \times 10^{-5}$ at 50 GeV to $(11.0 \pm 2.5) \times 10^{-5}$ at 130 GeV. This increase is mainly due to acceptance, since each of the three muons is required to exceed a threshold of 4.5 GeV, on the average.

The x- and y-distributions of 3μ events are consistent with those for normal single-μ CC events. This means that on the average, half of the incident ν energy goes into the hadron system (including the non-leading muons).

The CDHS data have been compared with four different models for the origin of the 3μ events:

i) *Hadronic μ-pair production*

It has been assumed that the production of $\mu^+\mu^-$ pairs by 150 GeV π^+ mesons on beryllium has about the same features as does the production of $\mu^+\mu^-$ pairs by virtual W^+ bosons on nucleons. The data have been taken from Anderson et al.[68]. The Feynman x-distribution has been slightly modified to $x_F(1 - x_F)$ in order to reproduce the 3μ data better. As can be judged from Figs. 43-50, the hadronic μ-pair production describes the bulk of the data rather well. It contains basically the production and decay of vector mesons and the μ-pair bremsstrahlung from the quark sector.

ii) *Internal bremsstrahlung*

This process can occur both in the lepton sector and in the hadron sector, with interference between the two. The process has been calculated[69] to occur at a rate of $\sim 10^{-5}$ of the CC events, for the experimental conditions of the CDHS experiment. A particular feature of this process is that the distribution in $\Delta\phi$ between the leading μ and the vectorial sum of the non-leading μ's (Fig. 46c) is roughly symmetric: it peaks at 0° and at 180°, and has a minimum at 90°. This feature is well in line with the data. The following rates have been obtained from a fit to the $\Delta\phi$ distribution in Fig. 46c:

$$\frac{\sigma(3\mu)}{\sigma(\text{single }\mu)}\left[\text{e.m. bremsstrahlung}\right] = (0.8 \pm 0.4) \times 10^{-5} ,$$

in good agreement with the expectation.

iii) *Heavy lepton cascade*

A possible mechanism for 3μ production might be the production and subsequent cascade decay of heavy leptons:

$$\nu + N \to L^- + X$$
$$\hookrightarrow L^0 + \mu^- + \bar{\nu}$$
$$\hookrightarrow \mu^+ + \mu^- + \nu \; .$$

In order to resemble the observed data, L^- must have a large mass (taken as 9 GeV), and L^0 a small mass (1.5 GeV). The model has assumed a constant decay matrix element, a flat cross-section above threshold, and the same x- and y-distributions as found in ν CC interactions. The transverse momenta yielded by this model are substantially larger than those observed in the data (Fig. 45c). This allows us to arrive at the conclusion that at most 17% (90% c.l.) of the 3μ events observed by CDHS are due to this heavy lepton cascade.

iv) *Heavy quark model*

The production and subsequent cascade decay of heavy quarks, for example

$$\nu + \bar{u} \to \mu^- + \bar{b} + X \qquad (b = \text{"bottom" quark}) ,$$
$$\hookrightarrow \bar{c} + \mu^+ + \nu$$
$$\hookrightarrow \bar{s} + \mu^- + \bar{\nu}$$

is another possible source of 3μ events. The model, computed with a $\bar{b}$ mass of 4.5 GeV, x- and y-distributions consistent with production off the sea, and a Feynman x-distribution peaked at $x_F = 1$, also does not exhibit close similarity with the data.

In conclusion, the 3μ events recorded in the CDHS experiment can be explained both in the kinematic distributions and in the observed cross-section by conventional sources (hadronic muon pair and bremsstrahlung pair production). Exotic sources can at most account for $\sim$ 20% of the observed events, although there is no apparent need to invoke such phenomena. The 3μ production due to a new type of neutrino is improbable, as shown in a beam dump experiment (see Section 7). Associated charm production cannot contribute substantially since the expected rate is too small ($\sim 10^{-6}$ of the CC events). Finally, the Drell-Yan mechanism is also expected to contribute at a much lower level than the observed rate of 3μ events.

At this stage, let us return to the 3μ events reported by the HPWFR group. Their conclusion that the origin of a substantial fraction of their 3μ-event sample may be in the lepton sector rather than in the hadron sector has been based in part on the observed raw rate of $\sim 5 \times 10^{-4}$ per neutrino interaction above 100 GeV. This rate has been found to be too high to be understood by conventional sources of 3μ events, in agreement with the rate estimates of the CDHS group. However, the rate of 3μ events quoted recently by the HPWFR group[70],

$$\frac{\sigma(3\mu)}{\sigma(\text{single } \mu)} = (9 \pm 5) \times 10^{-5} \qquad \text{for } E_\nu > 30 \text{ GeV}$$

$$\frac{\sigma(3\mu)}{\sigma(\text{single } \mu)} = (2.6 \pm 1.5) \times 10^{-4} \qquad \text{for } E_\nu > 100 \text{ GeV}$$

is in good agreement with the rates reported by the CDHS group. Also the invariant $\mu^+\mu^-$-pair masses, for the 8 out of 13 events which satisfy about the same cut-off (4.5 GeV) in muon energy as that applied to the CDHS data, fit without problems into the CDHS mass-distribution scatter plot (Fig. 48a). Note that this mass comparison is independent of the choice of the leading muon, which has been defined in the HPWFR analysis to be the most energetic one. The over-all conclusion is that no discrepancy between the HPWFR and CDHS data is exhibited either from the rate or from the characteristics of the bulk of observed events. The dominantly hadronic origin of 3μ events can therefore be considered to be established.

However, two events (Nos. 119-017991 and 281-147196) of the HPWFR 3μ sample seem not to fit into the picture of the hadronic origin. They are shown in Fig. 51, superimposed on the HPWFR detector. Although the $\mu^+\mu^-$-pair mass combinations do not appear to be extraordinary (see Fig. 48a), the events have the unusual characteristics that

a) most of the energy of the incident ν goes into the muons, and very little energy to the hadron showers, and

b) no pair of opposite-sign muons is able to balance the transverse momentum of the third (negative) muon as would be expected for a $\mu^+\mu^-$ pair from the hadronic vertex of the event (see Fig. 52).

The HPWFR group has concluded[65] that these two events may have a combined weak-electromagnetic origin.

Events with such characteristics have not been recorded by the CDHS group. However, given the total energy of the two HPWFR events (> 200 GeV) there is no discrepancy between the experiments. Despite the fact that the fluxes of the beams used at FNAL and at CERN for the 3μ search are largely different at low energies, the beam energy spectra converge more or less at very high energies since the difference in the focusing devices becomes unimportant. Given the fact that the total number of 400 GeV protons on the target (see Table 10) is a factor of 4 higher for HPWFR, and is reduced to an effective factor of 2 by the larger fiducial target mass of the CDHS detector ($\sim$ 670 tons for CDHS and $\sim$ 290 tons for HPWFR), the CDHS group would expect roughly one event -- always assumed that these events have a very high production threshold somewhere around 200 GeV. Thus so far the observations are compatible.

6.5 Four-lepton events

A ν-induced event with four energetic muons, displayed in Fig. 53, has recently been observed by the CDHS group[71] in the same exposure where the 76 $\mu^-\mu^-\mu^+$ events were found. Thus the raw rate of 4μ events is of the order of 10^{-6} compared to single-μ CC events. The main kinematical parameters are listed in Table 11.

Another 4μ event has been reported by the HPWFR group[65]. It has a fast negative muon with 25 GeV, and three additional muons with +10, +5, and -5 GeV, respectively. In the same reference 65, there is mention of the observation of another 4μ event.

Very recently, a $\mu^+e^-e^+e^-$ event has been found in the FNAL 15′ chamber[72].

Table 11

Main kinematical parameters of the CDHS 4μ event

Total observed energy		91.4 ± 7.3 GeV	
E_H		58 ± 7 GeV	
Momenta of the muons in GeV:	p_x	p_y	p_z
Muon 1 (+)	0.50	0.20	11.1
Muon 2 (-)	-1.52	-1.69	8.4
Muon 3 (+)	-0.93	-1.12	9.0
Muon 4 (-)	-0.24	-0.63	4.45

While it seems premature to reach conclusions about the nature of four-lepton events (given the very low statistics), the world statistics of these four-lepton events is already relatively high compared to that of 3μ events. This is unexpected if one has, for example, the notion that four-lepton events are basically 3μ events, but with additional single-charmed-particle production as in opposite-sign 2μ events.

7. BEAM DUMP EXPERIMENTS

Recently, a beam dump experiment has been carried out at the SPS neutrino facility at CERN. A total of 4.3×10^{17} protons with an energy of 400 GeV have been dumped into a solid copper block, in order to absorb the particles of the hadron cascade as quickly as possible. This reduces the flux of ordinary ν_μ from $\pi \to \mu + \nu$ and $K \to \mu + \nu$ decay by a factor of about 2000 compared to normal running in a horn-focused WBB, and increases the sensitivity for new "prompt" phenomena substantially.

Three neutrino detectors have been in operation during the beam dump running, at an average distance of 900 m from the target: the electronic detector of the CDHS group, and the bubble chambers BEBC and GGM, both filled with heavy liquids.

The original motivation for the beam dump experiment was the search for a new sort of penetrating particle produced either directly in the primary proton interaction or by prompt decay of new particles ("prompt" means a lifetime $\tau < 10^{-11}$ sec, or conversely a decay distance which is small compared to the nuclear absorption length in copper). The new particles could, for example, manifest themselves via an abnormal rate of multilepton events, an abnormal NC to CC ratio, and anomalies in the kinematic distributions of CC events.

The search for "new" particles has failed. But, unexpectedly, a new source of "old" neutrinos has been found by all three experiments involved[73-75].

Thanks to the high target mass, the CDHS detector has recorded the largest data sample. Table 12 summarizes the number of recorded events, together with the numbers of events of BEBC and GGM.

Table 12

Numbers of events recorded in the CDHS, BEBC, and GGM beam dump experiments

	CDHS	BEBC	GGM
μ^- events	727	29	12 } + 2 ambiguous
μ^+ events	160	5	2 } + 2 ambiguous
$\mu^+\mu^-$ events	6 (E_{vis} > 30 GeV)	0	0
3μ events	0	0	0
NC events	-	21	7
"Muonless" events	261	-	-
e^- events	-	11	} 9
e^+ events	-	4	} 9
Cut in visible energy	E_{vis} > 20 GeV	E_{vis} > 10 GeV	E_{vis} > 10 GeV
Effective number of protons on target	4.3×10^{17}	3.5×10^{17}	3.5×10^{17}

An immediate conclusion can be reached on the basis of the number of multi-muon events recorded by the CDHS experiment. The same experiment has previously observed, in a WBB run with 2.3×10^{17} protons of 400 GeV on the target, 13 3μ events and ∿ 1500 2μ events above 30 GeV visible energy. Normalizing to the same number of incident protons and making a comparison with the observed 3μ and 2μ event numbers in the beam dump experiment, it can be concluded that

$$< 10\% \text{ of } 3\mu \text{ events} \quad \text{and}$$

$$< 0.3\% \text{ of } 2\mu \text{ events}$$

observed in normal WBB running are due to the interaction of new particles, with 90% c.l. The six observed 2μ events are consistent, both in rate and characteristics, with those observed previously in NBB[50].

The distributions of the scaling variables x and y for the single-μ CC events observed by CDHS are in agreement with the expectation for normal ν_μ- and $\bar{\nu}_\mu$-induced CC events. But the predicted ratio of μ^+ to μ^- events for $E_\nu > 20$ GeV, i.e. 0.146 ± 0.015, falls significantly below the measured ratio of 0.22 ± 0.02. This excess of μ^+ events (see Fig. 54) indicates a new source of $\bar{\nu}_\mu$. With the assumption (!) that the new source is symmetric in ν_μ and $\bar{\nu}_\mu$, we obtain for the fraction $f = \mu^-(\text{new})/\mu^-(\text{old})$, from

$$\frac{\mu^+}{\mu^-} = \frac{(0.146 \pm 0.015) + f(\sigma^{\bar{\nu}}/\sigma^{\nu})}{1 + f} = 0.22 \pm 0.02 \ ,$$

the result $f = (28 \pm 11)\%$, where $\sigma^{\bar{\nu}}/\sigma^{\nu} = 0.48$ has been used.

BEBC and GGM, thanks to their excellent electron detection capability, have observed unambiguous events with energetic e^+ and e^- in the final state. The expected rate of e^+ and e^- events from standard sources such as K and hyperon decays cannot account for the observed number of events. The predicted ratio of e^- events to μ^- events of 0.06 is significantly exceeded. BEBC expects 1.8 e^- and 0.5 e^+ events, in contrast to 11 e^- and 4 e^+ events observed. GGM is in agreement with this observation. This excess of electron events indicates unambiguously also a new source of ν_e and $\bar{\nu}_e$.

The CDHS experiment confirms this conclusion, but not by direct observation of electron results. It uses the property that an electromagnetic shower develops much faster in iron than does a hadron shower. From an analysis of the energy deposition as a function of the depth in iron, it has been shown that an abnormal amount of electromagnetic energy is present in "muonless events" (electron events appear in the CDHS detector as muonless events, since the electromagnetic cascade is masked by the hadron shower). The observed ratio of muonless events to CC events, which is expected to be ~ 0.3 (see Section 5.4), is actually observed to be 0.84 ± 0.08, confirming the contribution of a new source of ν_e and $\bar{\nu}_e$. The total visible energy spectrum of the new source is shown in Fig. 55.

The most plausible origin of the excess of $\bar{\nu}_\mu$-, ν_e-, and $\bar{\nu}_e$-induced events (and possibly of ν_μ-induced, too) is associated charm production in the target. Charmed particles are expected to have electronic and muonic semileptonic decays of similar strength. The fluxes of ν_μ, $\bar{\nu}_\mu$, ν_e, and $\bar{\nu}_e$ of this new source are expected to have the same intensity.

The calculation of the total cross-section for associated charm production is very much model-dependent. Only a small fraction of neutrinos, arising from charmed particles produced in the very forward direction, can be detected. The results are (assuming associated $D\bar{D}$ production)

$$\sigma_{D\bar{D}}\ (p\text{-}p) \sim 30\ \mu b \qquad \text{(CDHS)}$$

$$\sigma_{D\bar{D}}\ (p\text{-}p) = 100\text{-}400\ \mu b \qquad \text{(BEBC)}$$

$$\sigma_{D\bar{D}}\ (p\text{-}p) = 360\ ^{+\ 170}_{-\ 110}\ \mu b \qquad \text{(GGM)}$$

where a semileptonic branching ratio of D mesons of 9% [52] has been assumed. All experiments agree on the existence of a new source. However, the CDHS experiment quotes a production cross-section which is lower than that from the bubble chambers, mainly because there is a lower number of "muonless" events than would be expected on the basis of the electron event numbers observed in the two bubble chambers. The discrepancy between the CDHS result and the bubble chamber results has a statistical significance of $\sim 3\sigma$, and is as yet unexplained.

In any case, the reported cross-sections seem fairly high compared to the limit $\sigma_{D\bar{D}} \lesssim 1.5$ μb reported by an emulsion experiment at 300 GeV [76]. The contradiction is possibly avoided if the lifetime of the charmed particle is either very short ($< 10^{-14}$ sec) or very long ($> 10^{-12}$ sec). In either case the emulsion experiment would not be fully efficient.

8. NEW PARTICLES

8.1 The W boson

No direct evidence for the production and decay of W bosons has been reported so far, suggesting that the W-boson mass is too large to be produced at the centre-of-mass energies at present available. (Note that the expectation of the Weinberg-Salam model with $\sin^2 \theta_W = 0.25$ is $M_W = 75$ GeV and $M_{Z^0} = 87$ GeV.) Only lower limits for the W-boson mass can be given from a fit of a propagator term to total ν cross-section data.

The CITFR group[77] concludes from its data that $M_W > 30$ GeV (90% c.l.), in the absence of scale-breaking terms (see Fig. 56). If a scale-breaking Q^2-dependence is allowed, the sensitivity for the propagator effect is diminished. With $\langle Q^2 \rangle / E \propto E^{-0.15}$, they then get $M_W > 20$ GeV.

8.2 New heavy leptons

In gauge theories of the Georgi-Glashow type[78] the existence of a positively charged heavy lepton M^+ with a muonic lepton quantum number is needed to cancel divergent processes. It is produced and decays as follows:

$$\nu_\mu + N \rightarrow M^+ + X \,, \qquad M^+ \rightarrow \mu^+ \nu_\mu \nu_\mu$$

Hence, "wrong-sign" muons are a signature for gauge-theory-type heavy leptons.

The branching ratio $B_\mu = (M^+ \rightarrow \mu^+)/(M^+ \rightarrow \text{anything})$ is predicted to be a function of the M^+ mass[79,80]. The ν-M^+ coupling is expected to be the same as the ν-μ^- coupling[80].

The CDHS experiment has reported a search for single positive muons in a ν NBB[43]. One event with a visible energy greater than 100 GeV has been found, most likely due to background. The result for the lower limit on the M^+ mass is 12 GeV (90% c.l.).

A similar search has been carried out by the CITF group[81], with a lower limit for the M^+ mass of 8.4 GeV (90% c.l.).

Upper limits on the production of heavy leptons $L^\pm$ with a muonic lepton quantum number have recently been reported by a Brookhaven-Columbia group[82] from a search for the decays $L^\pm \to e^\pm + \nu + \bar{\nu}$ in the FNAL 15' chamber. The signature is an e^+ or e^- without any other charged leptons in the final state of ν_μ-induced events. The events found are most likely due to ν_e and $\bar{\nu}_e$ interactions from the ν_e, $\bar{\nu}_e$ contamination of the horn-focused WBB. The results for the masses of heavy leptons with muonic lepton quantum number are:

$$M(L^-) > 7.5 \text{ GeV} \quad \text{and} \quad M(L^+) > 9 \text{ GeV (90\% c.l.)} .$$

8.3 τ production by neutrinos

From the same result on the search for electrons in the final state of ν_μ-induced reactions cited in the preceding section, the Brookhaven-Columbia group[82] concludes that the coupling strength of the heavy lepton τ [83] to ν_μ must be less than 2.5% (90% c.l.) of the (ν_μ-μ) coupling strength.

A similar result has recently been obtained by the BEBC group[59]. Again, from a search for electron events (assumed to arise from the leptonic τ decay mode $\tau^- \to e^- + \bar{\nu}_e + \nu_\tau$) it is concluded that the (ν_μ-τ) coupling strength is less than 6% (90% c.l.) of the (ν_μ-μ) coupling strength, in agreement with the previous result.

8.4 The SKAT heavy-lepton candidate

In the heavy-liquid bubble chamber SKAT at Serpukhov, an interesting event has been observed[84] in a WBB exposure ($E_\nu \sim$ 2-30 GeV) among 500 ν interactions. The event has one μ^- and one e^+ track, originating from a common vertex at a

distance of 4.8 mm after the neutrino interaction point. The direction of the total momentum of the $\mu^- e^+$ pair does not coincide with the one that connects the pair vertex and the neutrino interaction vertex. The observed event is consistent with the topology

$$\nu_\mu + p \rightarrow \mu^- + e^+ + 2\pi^0 + p \ .$$

The authors conclude that background processes are unlikely to explain the observed event. It may be interpreted as the production and subsequent decay of a heavy neutral lepton M^0 with muonic lepton quantum number:

$$\begin{array}{l} \nu_\mu + p \rightarrow M^0 + 2\pi^0 + p \\ \qquad\qquad\quad \hookrightarrow \mu^- + e^+ + \nu_e \ . \end{array}$$

The mass of M^0 is in the range 1.4–2.1 GeV, and the lifetime $\sim 6 \times 10^{-12}$ sec.

8.5 The Aachen-Padova heavy-lepton candidates

In the Aachen-Padova group multiplate spark chamber experiment exposed to the low-energy WBB at the CERN PS, a signal of events with μe pairs has been observed[85] above background. The μe pairs are not accompanied by other particles except recoil protons. The background is dominated by single-π^0 production in CC interactions, with one decay γ lost. For electron energies above 2 GeV the expected background is 4 ± 2 events, whereas 12 μe events have been observed. The relative rate normalized to single-μ CC interactions is $\sim 10^{-4}$. The absence of hadrons, the large energy of the electron, and the small angles between the muon and the electron make charm production and decay an unlikely source of the observed events. However, the observed topology is consistent with the production and decay of a neutral heavy lepton with a mass of ∼ 2 GeV, in the same process which may explain the SKAT event.

9. CONCLUSIONS AND OUTLOOK

In the recent past, good progress has been achieved in the understanding of the physics of ν scattering. On the other hand, it is fair to say that no discovery has been made which has substantially changed our physics picture. One

might entitle the recent outcome of neutrino experimentation "Back to the normal world. But is it really so normal?".

The achievements may be summarized in more detail as follows:

a) The naive quark parton model describes the data reasonably well. Possible deviations at the level of 10-20% are in agreement with the data. The deviations are in line with the results of e/μ scattering experiments and with predictions of QCD. However, the only firm conclusion that can be reached at present on the basis of the existing data is that things change between the energy domains below 10 GeV and above 30 GeV. One may interpret this as scaling violation. But scaling violations have not been demonstrated in ν scattering on the basis of data above 30 GeV. The precise measurement of structure functions and their scaling behaviour in a Q^2 range as wide as possible is today's challenge in the physics of CC interactions.

b) In all aspects that have been tested, NC experiments have confirmed the predictions of the Weinberg-Salam model surprisingly well. The favoured value of $\sin^2 \theta_W$, with relatively good agreement of all experiments, is $\sin^2 \theta_W \sim 0.25$. It is hard to imagine that it is just a simple accident that $\sin^2 \theta_W$ has adopted this singular value.

c) Despite the good over-all agreement of all NC phenomena in ν scattering, we should not forget that only inelastic scattering on isoscalar targets has reached fairly good experimental precision. There is still a lot to be done: in particular, to increase the statistics in $\nu_\mu e$ scattering; to make precise measurements of R_ν and $R_{\bar{\nu}}$ on proton targets; to study all NC single-π production channels also for incident $\bar{\nu}$; to increase the statistics in order to enable more precise measurements of the NC y-distribution; and last but not least, to measure the NC x-distribution.

d) The failure to observe parity violation in atomic transitions[86] at the level predicted by the Weinberg-Salam model causes a considerable problem. If the model is too simple, the choice of a larger gauge group while

preserving the successful description of ν-scattering phenomena may be necessary. However, a lack of understanding of the effects of the atomic shell in heavy atoms might also cause the trouble, or -- less likely -- the experiments may change their results. It is worth mentioning in this context that none of the ν experiments has demonstrated parity violation in NC by measuring a pseudoscalar quantity. Hence parity violation in ν scattering is not proved experimentally.

e) The physics of opposite-sign 2μ events is understood in terms of charm production and decay. At the present level of accuracy, no further mechanism is needed to account for all observations. However, the existing data sample has already been increased by a factor of 100, and high statistics results will become available. Also, measurements of the polarization of the second muon will be performed in due time.

f) Like-sign 2μ events are mainly due to trivial $\pi(K) \rightarrow \mu$ decay background. A genuine like-sign signal might exist at a lower level. Already available high statistics data will answer this question.

g) The bulk of 3μ events is understood, in terms of conventional sources, by the hadronic and electromagnetic creation of $\mu^+\mu^-$ pairs. For events with total energy below about 200 GeV, no further mechanism is needed to explain the data; this, of course, only at the present level of statistical accuracy.

h) Two 3μ events with visible energy above 200 GeV found by the HPWFR group might indicate another physics origin. Only more statistics can help us understand the source of the events.

i) Four-lepton events exist. Since several production mechanisms are conceivable (conventional and new ones), only more statistics can help us to understand them.

j) The beam dump experiments suggest associated charm production in pp collisions with a larger cross-section (> 10 μb) than is commonly expected.

k) No "new" particles beyond charm have been established in ν scattering. The τ lepton has small coupling to the ν_μ, if any. However, there are experimental hints at the existence of a neutral heavy lepton with a mass of about 2 GeV. It may, if it exists, show up via its muonic decay mode in opposite-sign 2μ events. Why not look for it in a high statistics data sample?

Acknowledgements

A substantial fraction of the experimental data described in these lectures comes from the work of my colleagues from the CDHS Collaboration: T. Hansl, M. Holder, J. Knobloch, J. May, H.P. Paar, P. Palazzi, F. Ranjard, D. Schlatter, J. Steinberger, H. Suter, H. Wahl, S. Whitaker and E.G.H. Williams from CERN; F. Eisele, K. Kleinknecht, H. Lierl, G. Spahn and H.J. Willutzki from Dortmund; W. Dorth, C. Geweniger, V. Hepp, K. Tittel and J. Wotschack from Heidelberg; F. Bloch, B. Devaux, S. Loucatos, J. Maillard, B. Peyaud, J. Rander, A. Savoy-Navarro and R. Turlay from Saclay; and F.L. Navarria from Bologna.

In particular I would like to thank F. Eisele, F.L. Navarria and S. Whitaker for a critical reading of the manuscript.

Last, but not least, I thank Prof. H. Mitter for his kind invitation and for the pleasant stay in Schladming.

REFERENCES

1) J. Steinberger, High-energy neutrino experiments, Proc. 1976 CERN School of Physics (report CERN 76-20, Geneva, 1976), p. 57.
D.H. Perkins, Inelastic lepton-nucleon scattering, Rep. Prog. Phys. 40, 409 (1977).
B.C. Barish, CalTech preprint CALT 68-621 (1977), to be published in Phys. Rep.

2) C.H. Llewellyn Smith, Phys. Rep. 3C, 261 (1972).

3) J.D. Bjorken, Phys. Rev. 179, 1547 (1969).

4) T. Eichten et al., Phys. Letters 46B, 274 (1973).

5) P.C. Bosetti et al., Phys. Letters 70B, 273 (1977).

6) B.C. Barish et al., Phys. Rev. Letters 39, 741 (1977).

7) B.C. Barish et al., Phys. Rev. Letters 39, 1595 (1977).

8) M. Holder et al., Phys. Rev. Letters 39, 433 (1977), and to be published.

9) B. Aubert et al., Phys. Rev. Letters 33, 984 (1974).
A. Benvenuti et al., Phys. Rev. Letters 36, 1478 (1976); 37, 189 (1976).

10) B.C. Barish et al., CalTech preprint CALT 68-607 (1977), unpublished.

11) F. Sciulli, Proc. Internat. Symposium on Lepton and Photon Interactions at High Energies, Hamburg, 1977 (ed. F. Gutbrod), (DESY, Hamburg, 1977), p. 239.

12) H. Deden et al., Nuclear Phys. B85, 269 (1975).

13) E.M. Riordan et al., Phys. Letters 52B, 249 (1974); SLAC-Pub-1634 (1975).
W.B. Atwood et al., SLAC-Pub-1758 (1976).

14) D.J. Fox et al., Phys. Rev. Letters 33, 1504 (1974).
Y. Watanabe et al., Phys. Rev. Letters 35, 898 (1975).
C. Chang et al., Phys. Rev. Letters 35, 901 (1975).
H.L. Anderson et al., Phys. Rev. Letters 37, 4 (1976); 38, 1450 (1977).

15) E. Gabathuler, talk given at the European Conference on Particle Physics, Budapest, 1977.
L.N. Hand, Proc. Internat. Symposium on Lepton and Photon Interactions at High Energies, Hamburg, 1977 (ed. F. Gutbrod), (DESY, Hamburg, 1977), p. 417.

16) J.P. Berge et al., Phys. Rev. Letters 39, 382 (1977).

17) D.J. Gross and F. Wilczek, Phys. Rev. D 8, 3633 (1973); D 9, 980 (1974).
A. Giorgi and H.D. Politzer, Phys. Rev. D 9, 416 (1974).

18) K. Schultze, Proc. Internat. Symposium on Lepton and Photon Interactions at High Energies, Hamburg, 1977 (ed. F. Gutbrod), (DESY, Hamburg, 1977), p. 359.
W.G. Scott, Seminar given at CERN, September 1977.

19) D.H. Perkins et al., Phys. Letters 67B, 347 (1977).

20) F. Hasert et al., Phys. Letters 46B, 138 (1973).

21) S. Weinberg, Phys. Rev. Letters 19, 1264 (1967); Phys. Rev. D 5, 1412 (1972).
A. Salam, Proc. 8th Nobel Symposium, Aspenasgården, 1968 (ed. N. Svartholm), (Almqvist and Wiksell, Stockholm, 1968), p. 367.

22) G. 't Hooft, Phys. Letters 37B, 195 (1971).

23) F. Reines et al., Proc. Internat. Neutrino Conference, Aachen, 1976 (eds. H. Faissner et al.), (Vieweg, Braunschweig, 1977), p. 217; Phys. Rev. Letters 37, 315 (1976).

24) J. Blietschau et al., Nuclear Phys. B114, 189 (1976); Phys. Letters 73B, 232 (1978).

25) H. Faissner, talk given at the Internat. Conf. on Parity Non-Conservation, Weak Neutral Currents and Gauge Theories, Batavia, 1977; Report PITHA 99 (1977).

26) G. Ecker, Nuclear Phys. B123, 293 (1977), and references quoted therein.

27) D. Cline et al., Phys. Rev. Letters 37, 252 and 648 (1976).
H.H. Williams, Proc. Internat. Symposium on Lepton and Photon Interactions at High Energies, Hamburg, 1977 (ed. F. Gutbrod), (DESY, Hamburg, 1977), p. 205.

28) W. Lee et al., Phys. Rev. Letters 37, 186 (1976).

29) M. Pohl et al., Phys. Letters 72B, 489 (1978).

30) H. Faissner et al., talk presented by E. Frenzel at the Tagung der Deutschen Physikalischen Gesellschaft, 13-16 March 1978, Heidelberg.

31) S.L. Glashow, J. Iliopoulos and L. Maiani, Phys. Rev. D 2, 1285 (1970).

32) F.A. Harris et al., Phys. Rev. Letters 39, 437 (1977).

33) M. Derrick et al., Report ANL-HEP-PR-77-69 (1977).

34) M. Holder et al., Phys. Letters 71B, 222 (1977).

35) B.C. Barish et al., Phys. Rev. Letters 34, 538 (1975).

36) J. Blietschau et al., Nuclear Phys. B118, 218 (1977).

37) P. Wanderer et al., preprint HPWF-77/1 (1977), submitted to Phys. Rev. D.

38) F. Merrit et al., CalTech preprints CALT 68-600 (1977) and CALT 68-601 (1977), unpublished.

39) H. Deden et al., talk presented at the Tagung der Deutschen Physikalischen Gesellschaft, 13-16 March 1978, Heidelberg.

40) M. Holder et al., Phys. Letters 72B, 254 (1977).

41) L. Wolfenstein, Nuclear Phys. B91, 95 (1975).

42) J. Blietschau et al., Phys. Letters 71B, 231 (1977).

43) M. Holder et al., Search for single positive muon production in neutrino interactions, CERN preprint, submitted to Phys. Letters.

44) W. Krenz et al., preprint CERN/EP/PHYS 77-50, submitted to Nuclear Phys. B.

45) O. Erriques et al., Phys. Letters 73B, 350 (1978).
H. Kluttig et al., Phys. Letters 71B, 446 (1977).

46) A. Benvenuti et al., Phys. Rev. Letters 34, 419 (1975).

47) B.C. Barish et al., Phys. Rev. Letters 36, 939 (1976).

48) B.C. Barish et al., Phys. Rev. Letters 39, 981 (1977).

49) A. Benvenuti et al., Phys. Rev. Letters 35, 1199, 1203, and 1249 (1975).

50) M. Holder et al., Phys. Letters 69B, 377 (1977).

51) A. Pais and S.B. Treiman, Phys. Rev. Letters 35, 1206 (1975).

52) G.J. Feldman, SLAC-Pub-2068 (1977).

53) R. Odorico, Phys. Letters 71B, 121 (1977).

54) J. Blietschau et al., Phys. Letters 58B, 361 (1975); 60B, 207 (1976).

55) J. von Krogh et al., Phys. Rev. Letters 36, 710 (1976).

56) P. Bosetti et al., Phys. Rev. Letters 38, 1248 (1977).

57) C. Baltay et al., Phys. Rev. Letters 39, 62 (1977).

58) H.C. Ballagh et al., Phys. Rev. Letters 39, 1650 (1977).

59) P.C. Bosetti et al., Phys. Letters 73B, 380 (1978).

60) M.K. Gaillard, Proc. Internat. Neutrino Conference, Aachen, 1977 (eds. H. Faissner et al.), (Vieweg, Braunschweig, 1977), p. 553.

61) M. Holder et al., Phys. Letters 70B, 396 (1977).

62) B.C. Barish et al., Phys. Rev. Letters 38, 577 (1977).

63) A. Benvenuti et al., Phys. Rev. Letters 38, 1110 (1977).

64) M. Holder et al., Phys. Letters 70B, 393 (1977).

65) A. Benvenuti et al., Phys. Rev. Letters 40, 488 (1978).

66) A. Benvenuti et al., Phys. Rev. Letters 38, 1183 (1977).

67) T. Hansl et al., Characteristics of trimuon events observed in high-energy neutrino interactions, CERN preprint, to be submitted to Nuclear Phys. B.

68) K.J. Anderson et al., Phys. Rev. Letters 37, 799 (1976).

69) C.H. Albright, J. Smith and J.A.M. Vermaseren, Fermilab Publ. 78/14-THY (1978), and references quoted therein.

70) T.Y. Ling, talk presented at XIIIth Rencontre de Moriond, 12-24 March 1978 (Les Arcs, France).

71) M. Holder et al., Phys. Letters 73B, 105 (1978).

72) J. von Krogh, private communication.

73) T. Hansl et al., Phys. Letters 74B, 139 (1978).

74) P.C. Bosetti et al., Phys. Letters 74B, 143 (1978).

75) P. Alibran et al., Phys. Letters 74B, 134 (1978).

76) G. Bertrand-Coremans et al., Phys. Letters 65B, 480 (1976).

77) B.C. Barish et al., Phys. Rev. Letters 39, 1595 (1977).
B.C. Barish, CalTech preprint CALT 68-621 (1977), to be published in Phys. Rep.

78) H. Georgi and S.L. Glashow, Phys. Rev. Letters 28, 1494 (1972).

79) C.H. Albright and C. Jarlskog, Nuclear Phys. B84, 467 (1975).

80) J.D. Bjorken and C.H. Llewellyn Smith, Phys. Rev. D 7, 887 (1973).

81) B.C. Barish et al., Phys. Rev. Letters 32, 1387 (1974).

82) A.M. Cnops et al., Phys. Rev. Letters 40, 144 (1978).

83) M.L. Perl et al., Phys. Rev. Letters 35, 1489 (1975).
M.L. Perl, Proc. Internat. Symposium on Lepton and Photon Interactions at High Energies, Hamburg, 1977 (ed. F. Gutbrod), (DESY, Hamburg, 1977), p. 145.

84) D.S. Baranov et al., Phys. Letters 70B, 269 (1977).
L.D. Soloviev, Proc. Internat. Symposium on Lepton and Photon Interactions at High Energies, Hamburg, 1977 (ed. F. Gutbrod), (DESY, Hamburg, 1977), p. 387.

85) H. Faissner et al., talk presented at the Internat. Conf. on Neutrino Physics and Neutrino Astrophysics, Elbrus (USSR), 1977.

86) L.L. Lewis et al., Phys. Letters 39, 795 (1977).
P.E.G. Baird et al., Phys. Letters 39, 798 (1977).

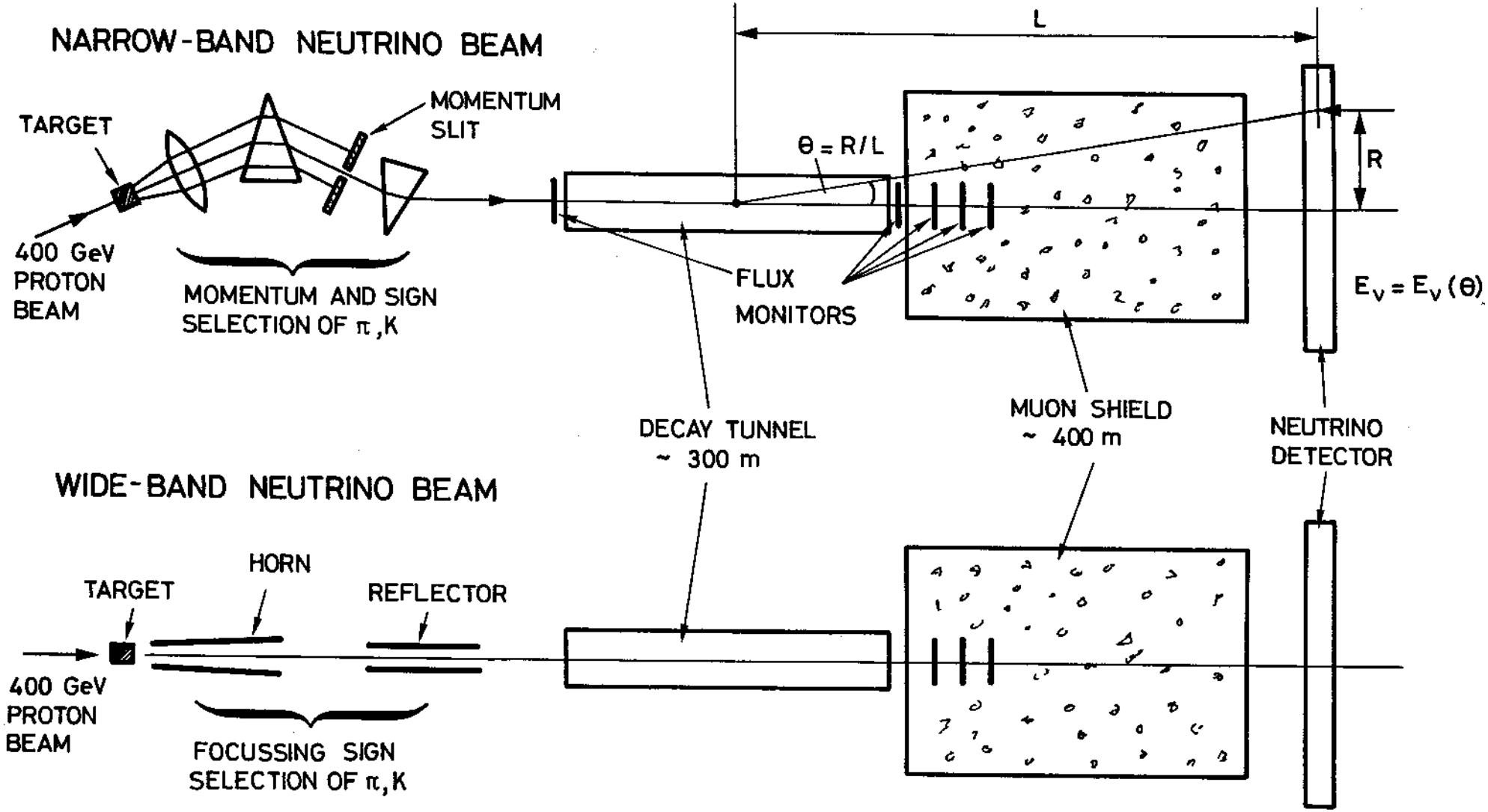

Fig. 1: Schematic layout of the narrow-band and wide-band neutrino beams.

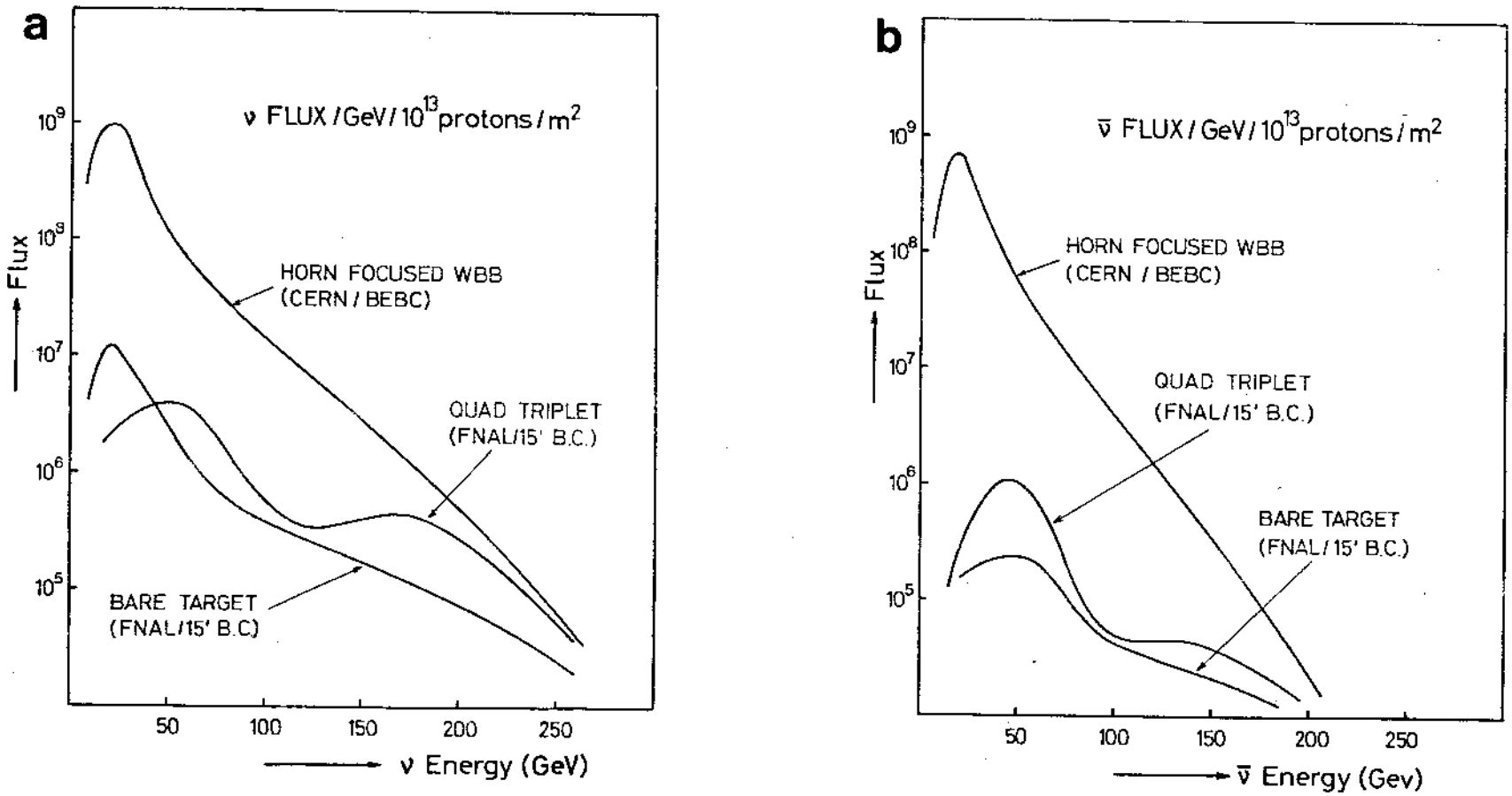

Fig. 2: Fluxes of different types of neutrino beam at FNAL and CERN, for neutrinos (Fig. 2a) and antineutrinos (Fig. 2b).

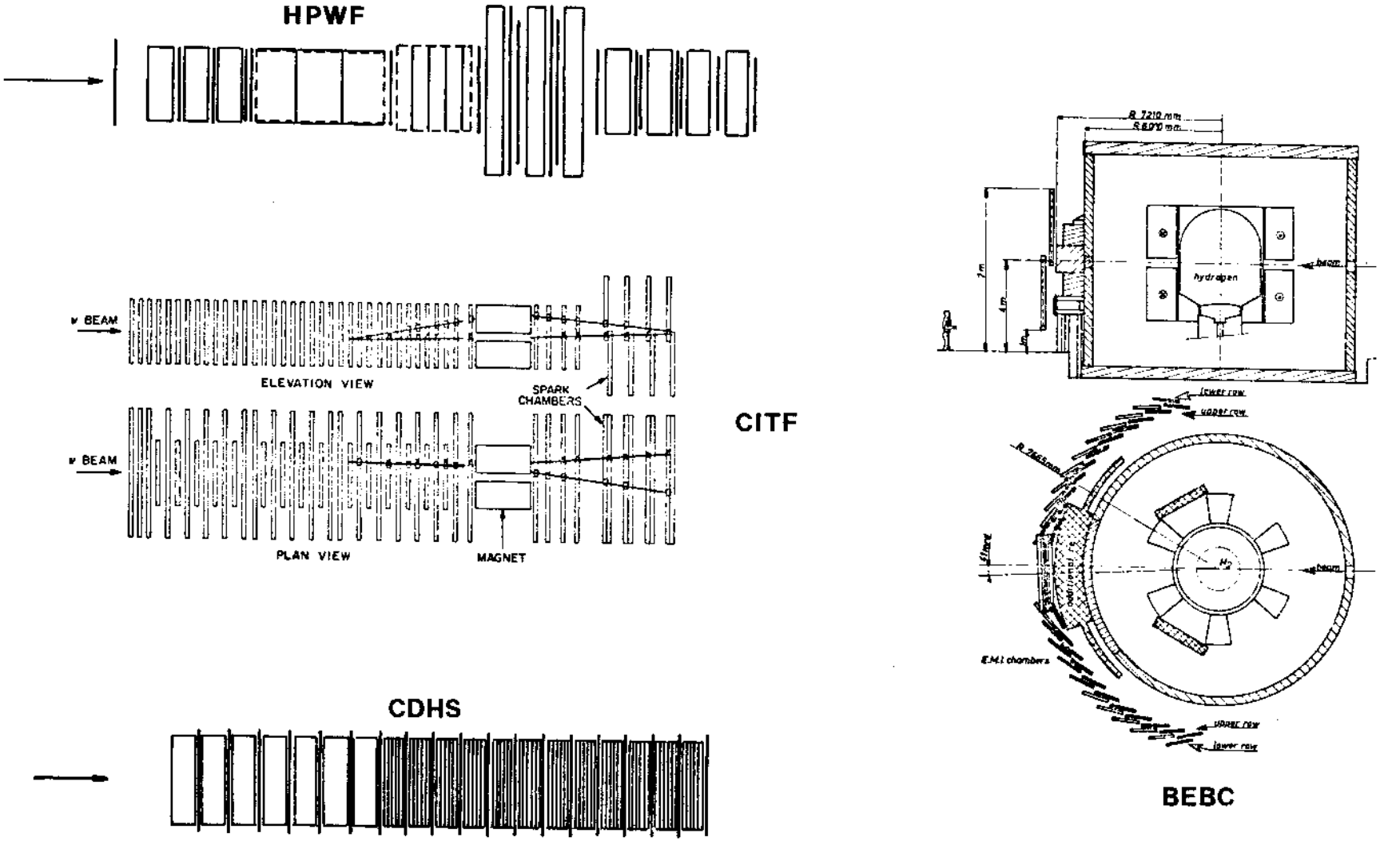

Fig. 3: On-scale comparison of the electronic detectors of the HPWF, CITF, and CDHS Collaborations, and the bubble chamber BEBC.

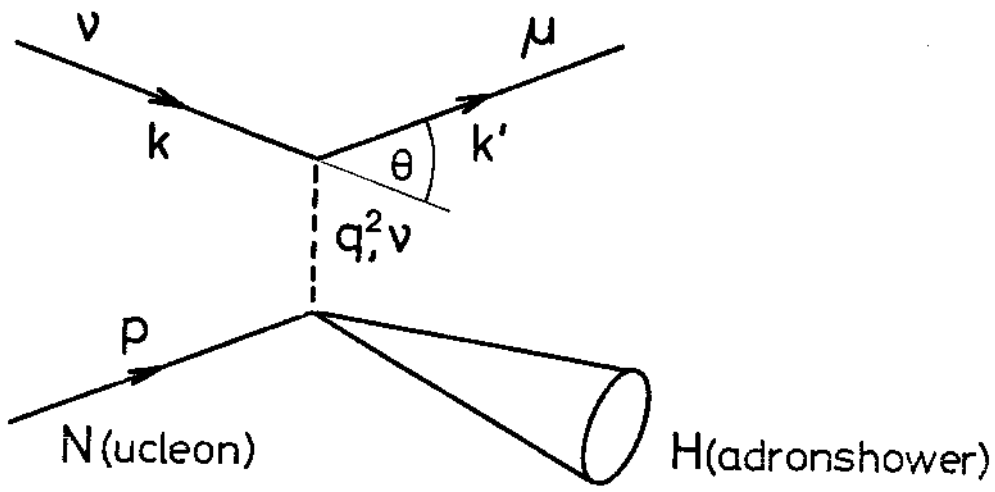

Inelastic neutrino-nucleon scattering

Fig. 4: Deep inelastic scattering of a neutrino on a nucleon via a charged current reaction.

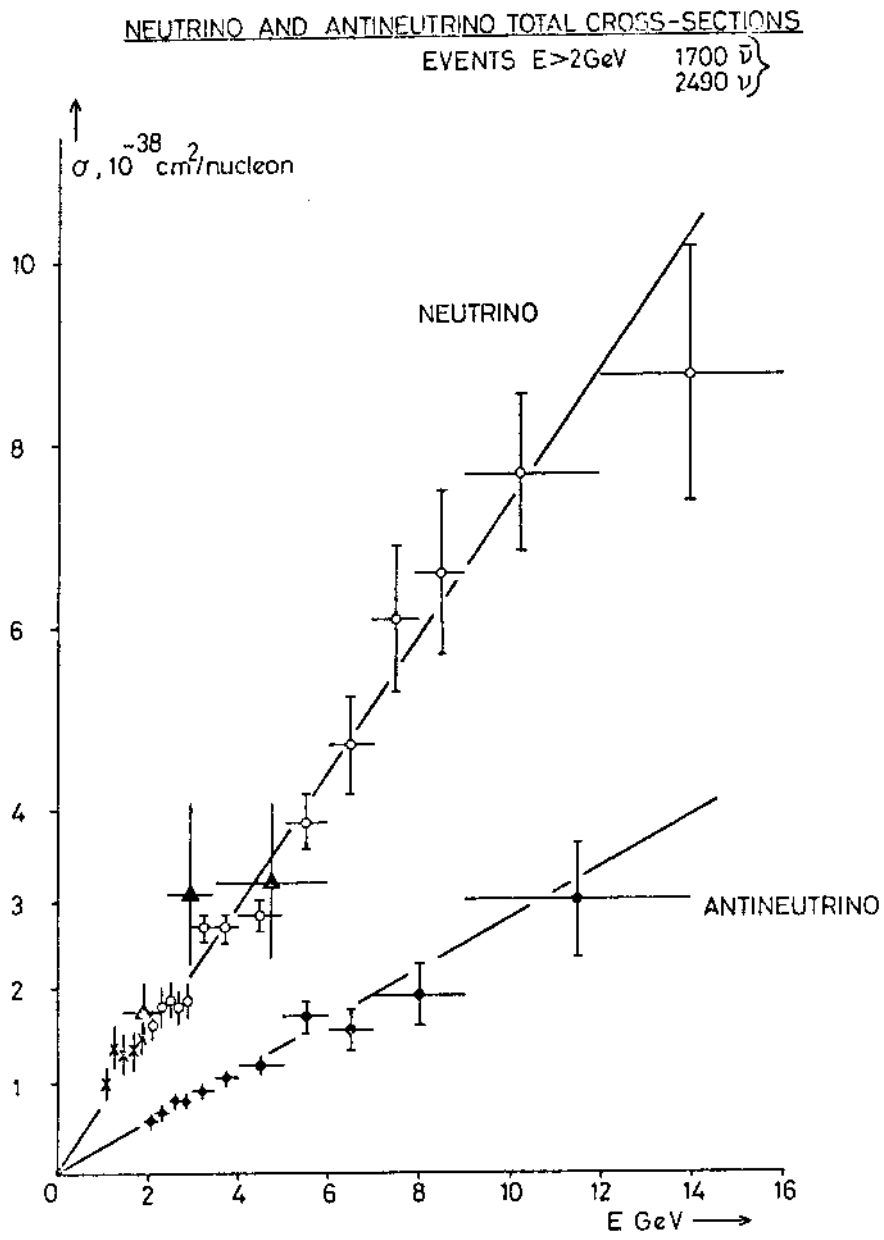

Fig. 5: ν and $\bar{\nu}$ total cross-sections in the energy range 1-15 GeV (GGM data).

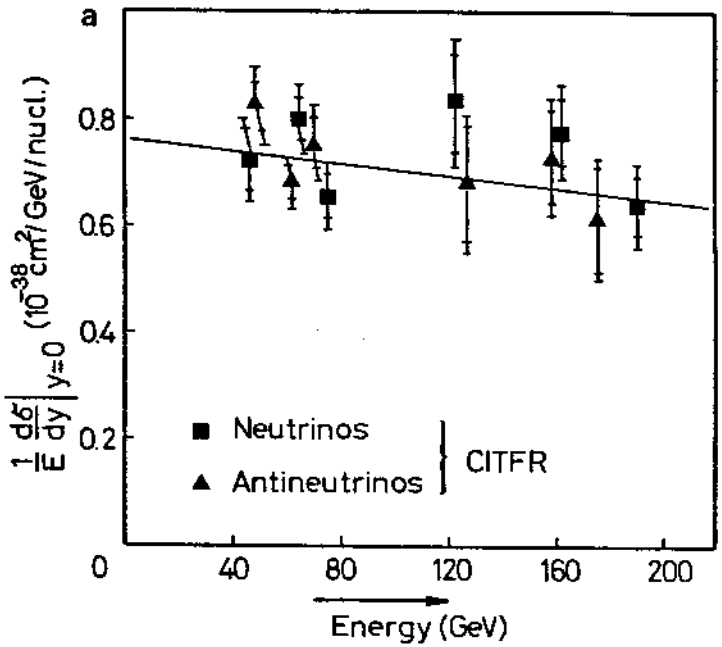

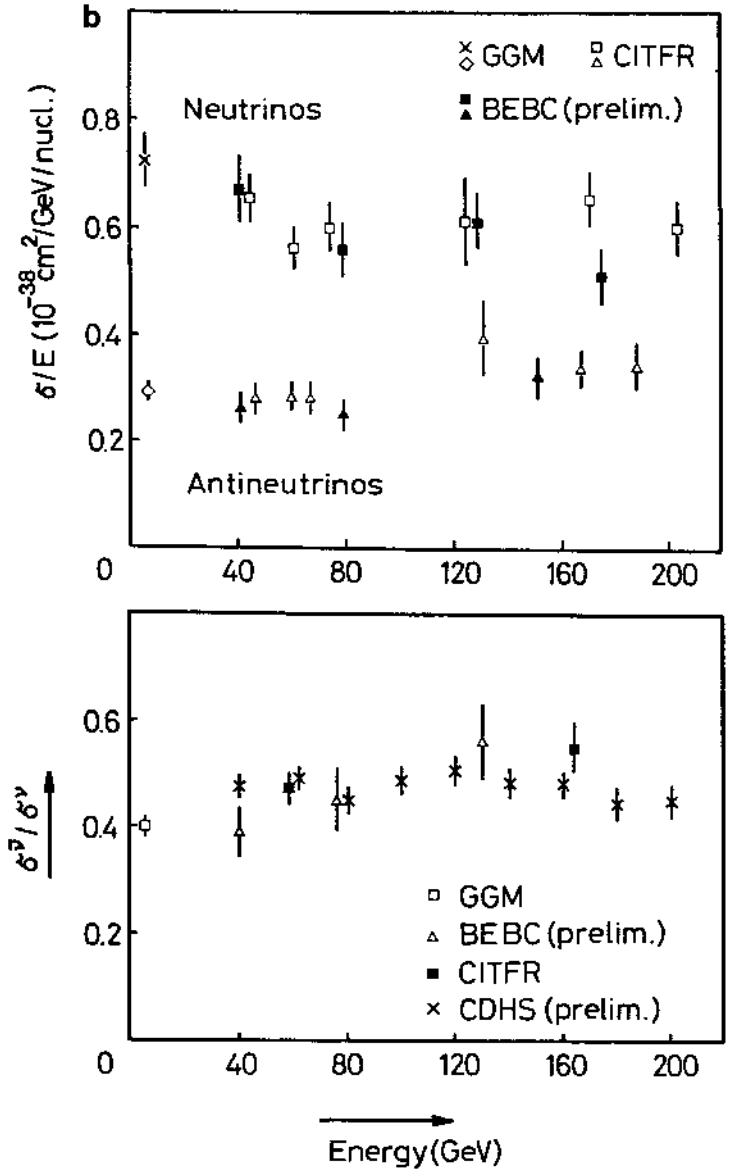

Fig. 6: Slopes of the ν and $\bar{\nu}$ "small-y" cross-sections in the energy range 45 to 200 GeV. The inner error bars denote statistical errors only. The best linear 2-parameter fit and the energy independent value are shown (CITF data) (Fig. 6a).

ν and $\bar{\nu}$ total cross-sections divided by energy, and their ratio, as a function of energy. The BEBC and CDHS error bars are statistical only. The CDHS points are subject to a common $\sim$ 10% normalization uncertainty below 100 GeV, and of $\sim$ 15% above (Fig. 6b).

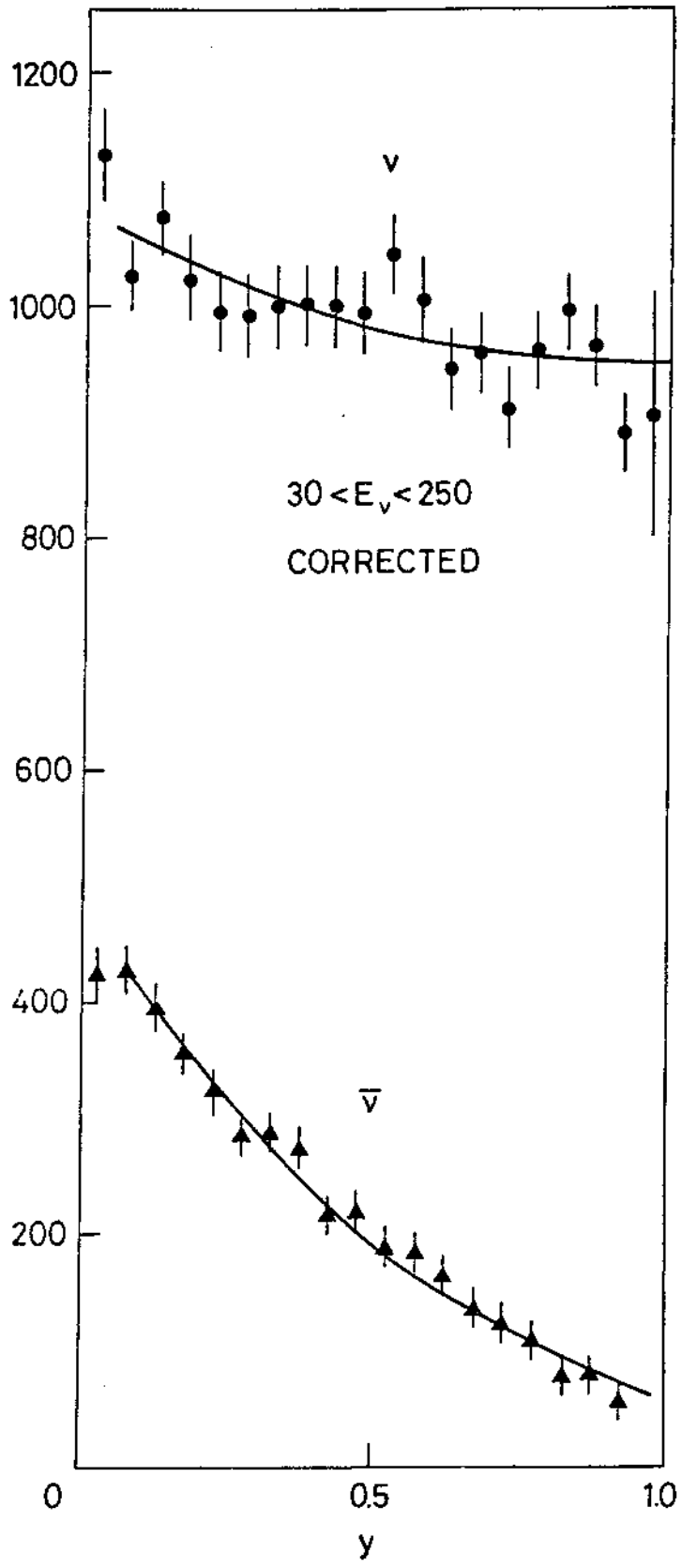

Fig. 7: y-distribution of ν and $\bar{\nu}$ CC events in the energy range 30-250 GeV. Errors are statistical only. The points are corrected for acceptance (CDHS data).

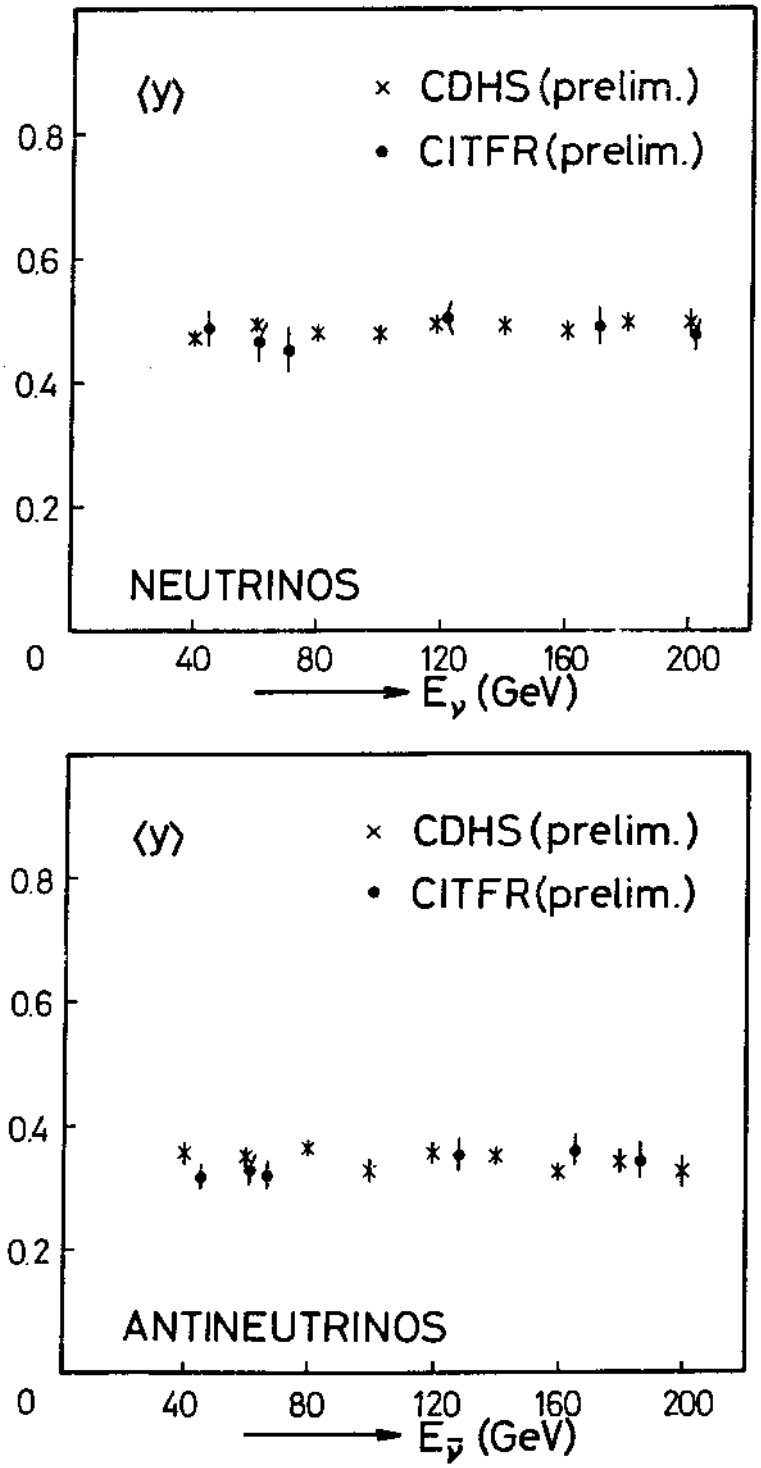

Fig. 8: <y> for ν and $\bar{\nu}$ as function of energy. The errors of the CDHS points are statistical only.

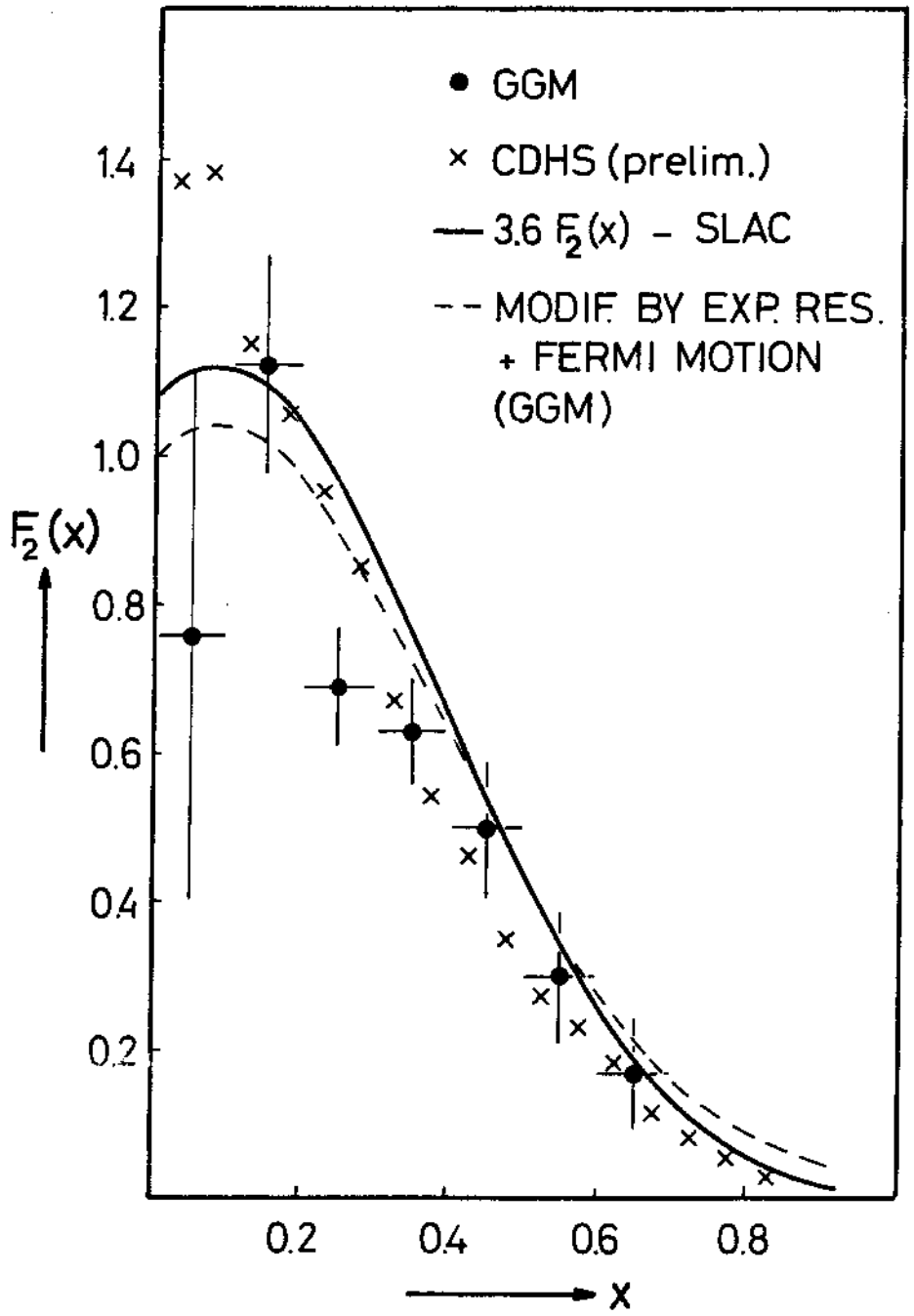

Fig. 9: Comparison of $F_2^{\nu N}(x)$ measured by GGM and CDHS. The smooth line is $F_2^{eN}(x)$ as determined in SLAC ed scattering experiments. The modification of $F_2^{eN}(x)$ due to Fermi motion and experimental resolution is indicated for the GGM experiment. The CDHS data are corrected for experimental resolution, but not for Fermi motion. They are normalized in area to $F_2^{eN}(x)$.

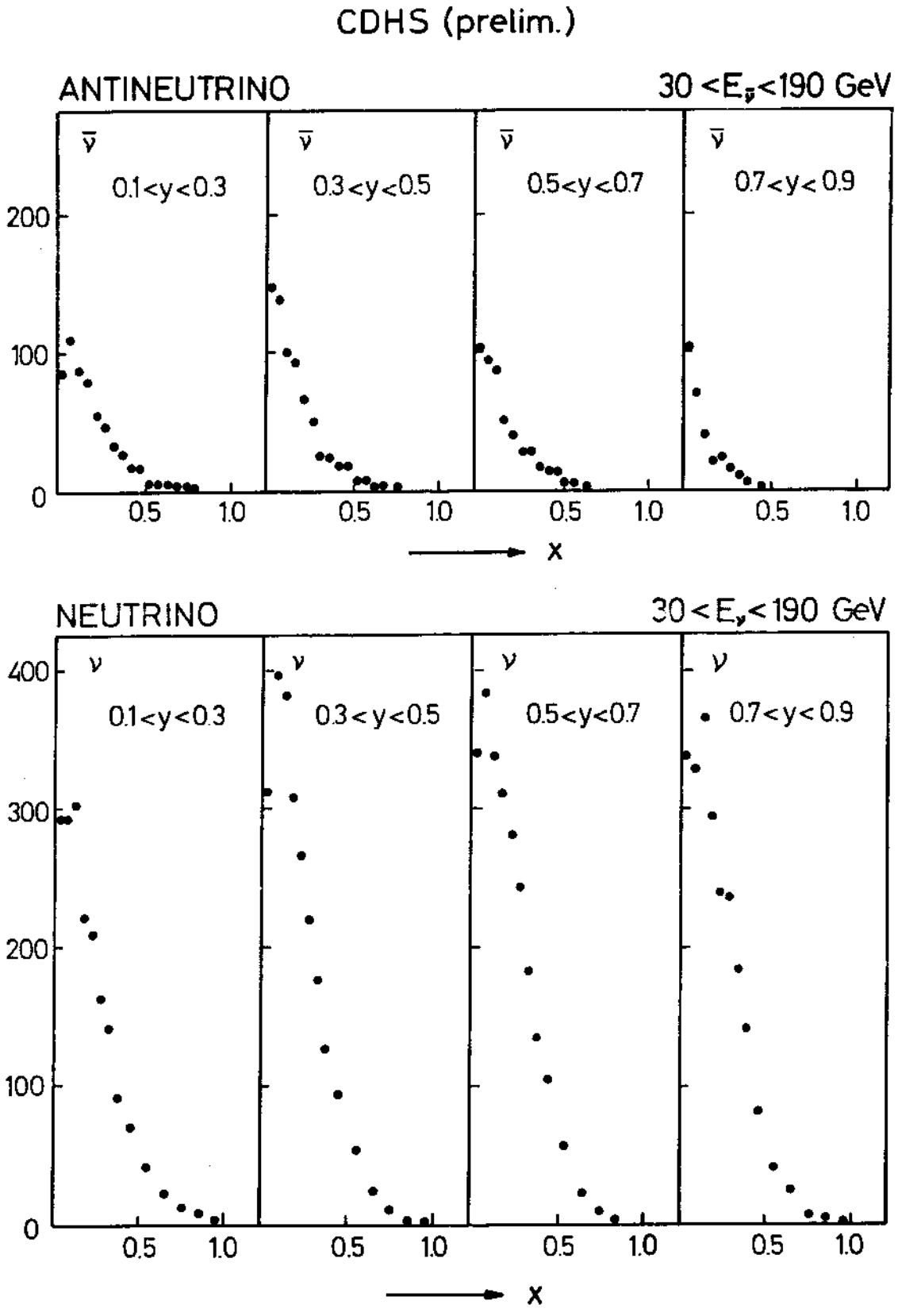

Fig. 10: x-distribution for ν and $\bar{\nu}$, for different bins in y, integrated over the energy range 30-190 GeV. The data are corrected for experimental resolution, but not for Fermi motion (CDHS data).

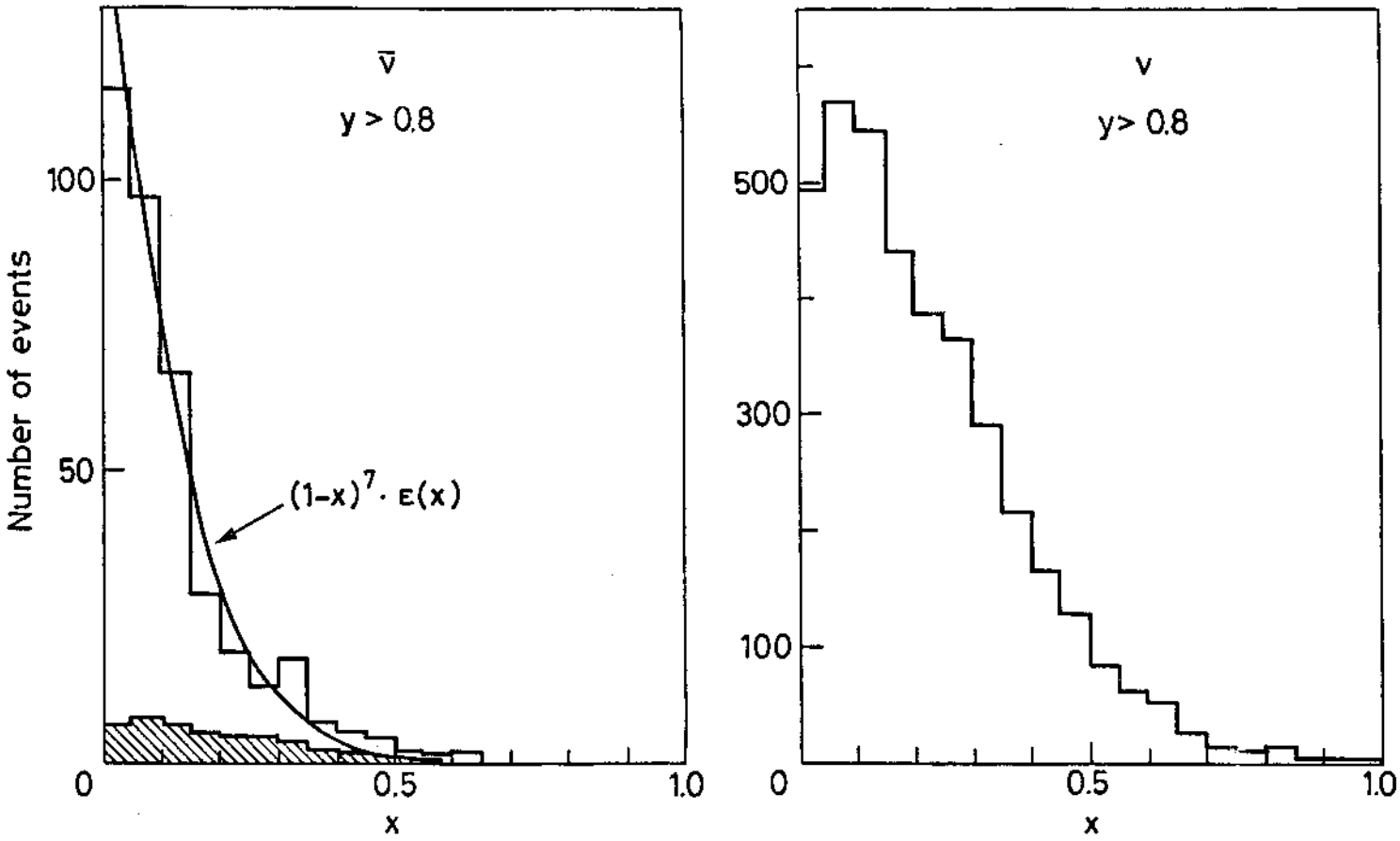

Fig. 11: x-distributions for y > 0.8 for ν and $\bar{\nu}$. The plot displays raw data. They are not corrected for acceptance, experimental resolution and Fermi motion (CDHS data).

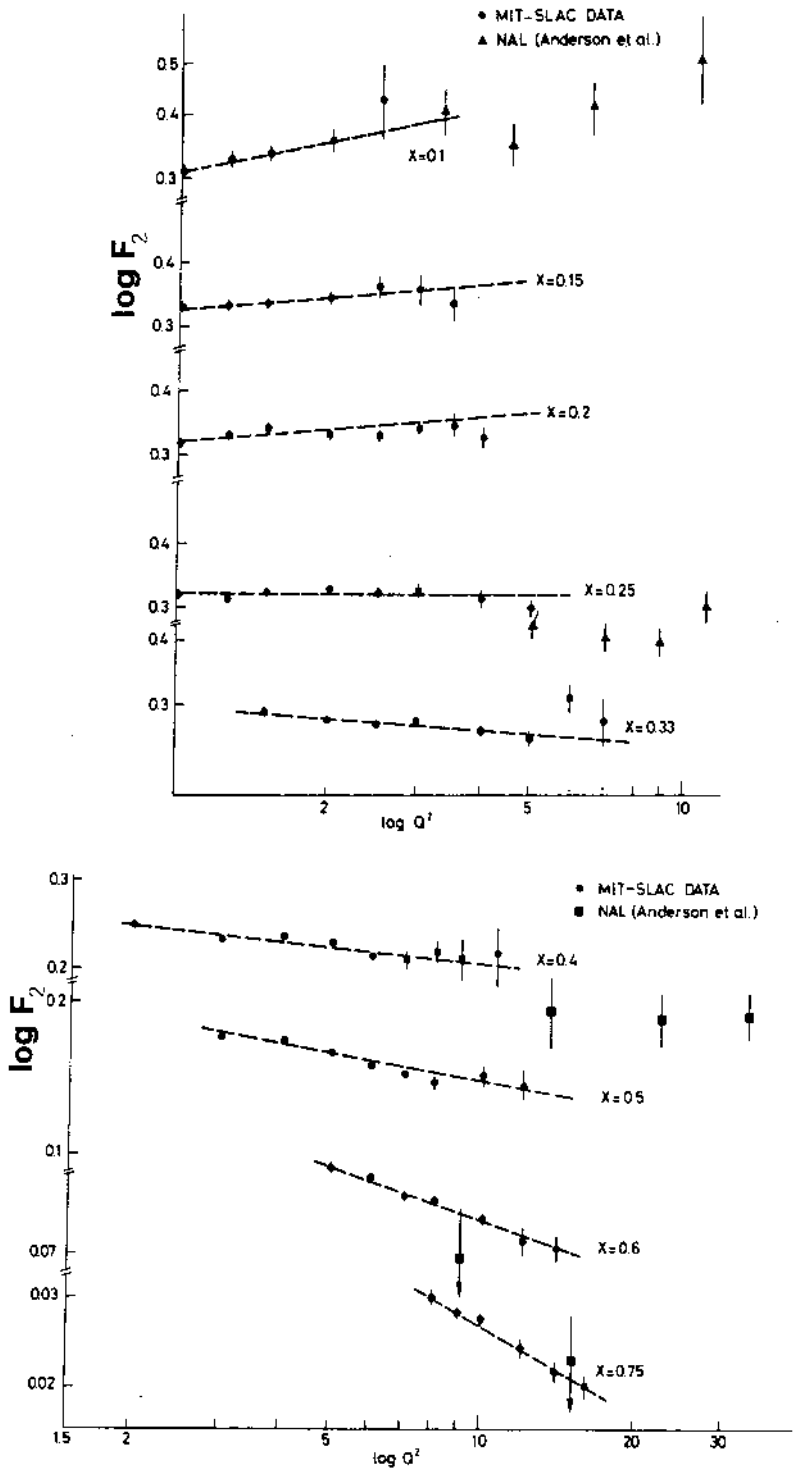

Fig. 12: The structure function F_2 for (ep)-scattering data from SLAC and for (μp)-scattering data from FNAL, as a function of Q^2 for different values of x. The dotted lines are least-squares fits to the data.

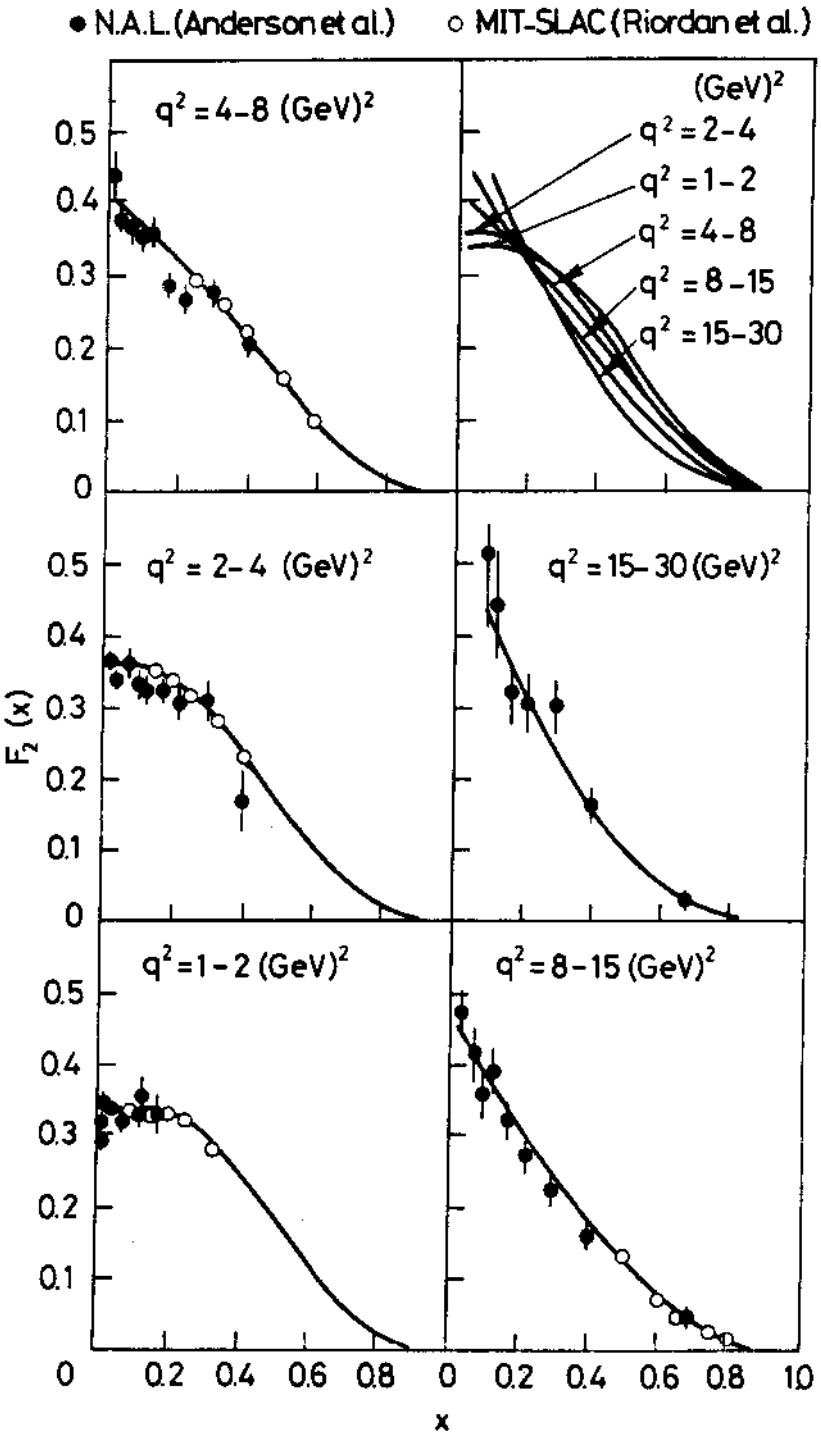

Fig. 13: The structure function $F_2(x)$ for (ep)-scattering data (SLAC) and (μp)-scattering data (FNAL) as a function of x in different Q^2 intervals.

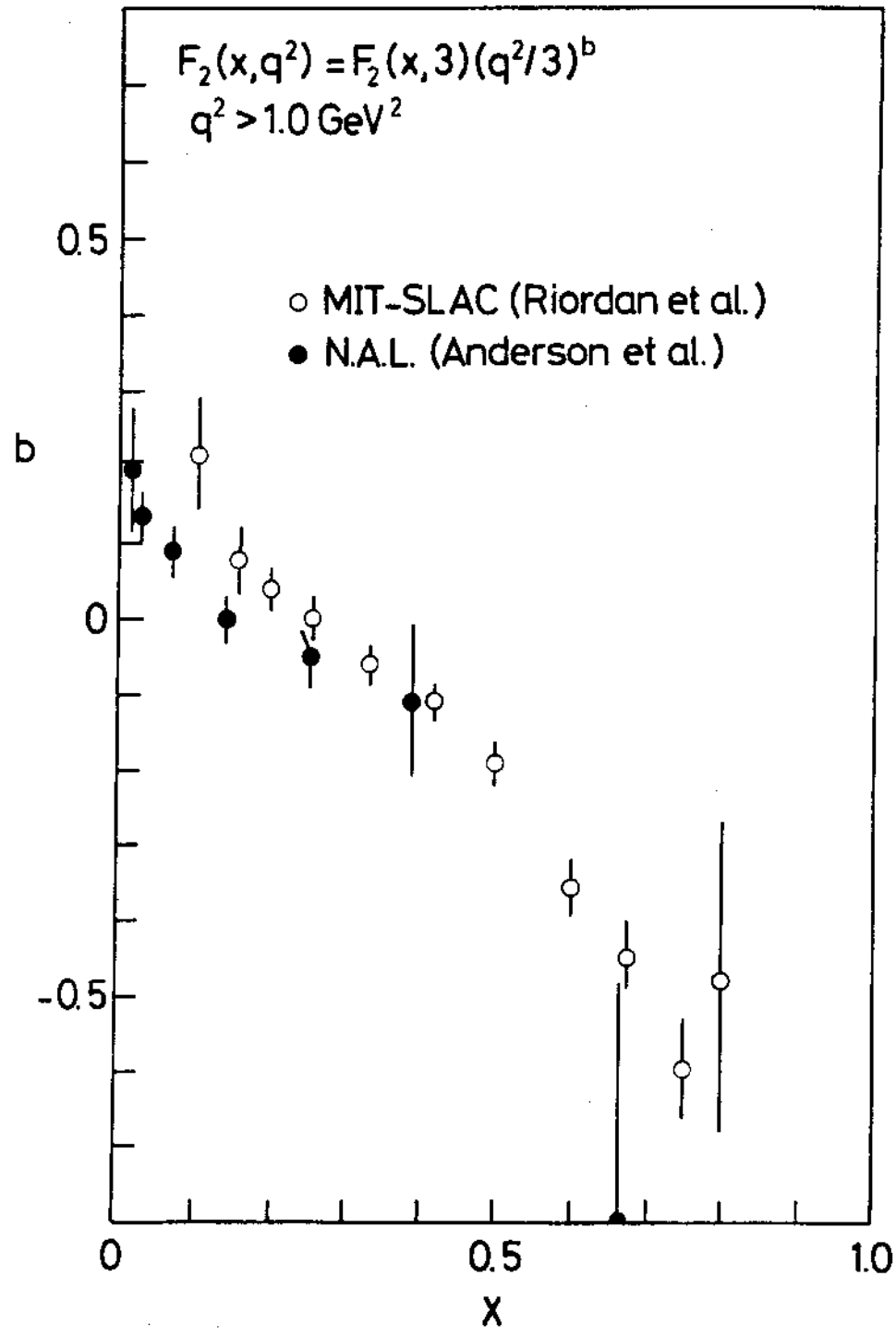

Fig. 14: Values of the rate of change of ln F_2 with ln Q^2 plotted versus x, for different e/μ scattering experiments.

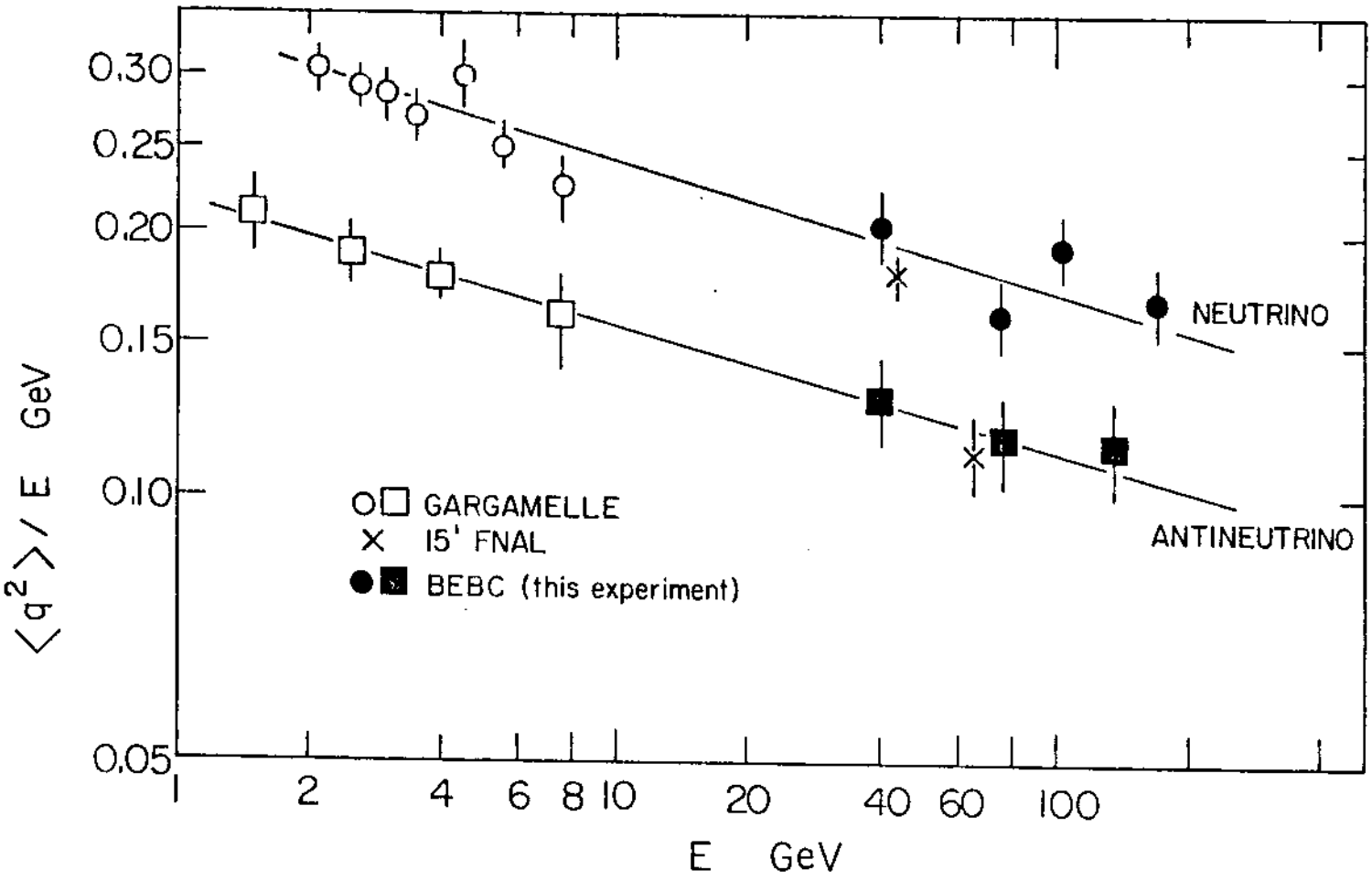

Fig. 15: $\langle Q^2 \rangle / E = 2M \langle xy \rangle$ as function of energy. The lines indicate the variation $\langle Q^2 \rangle / E \propto E^{-0.14}$ expected from an empirical fit to scaling deviations in e/μ scattering.

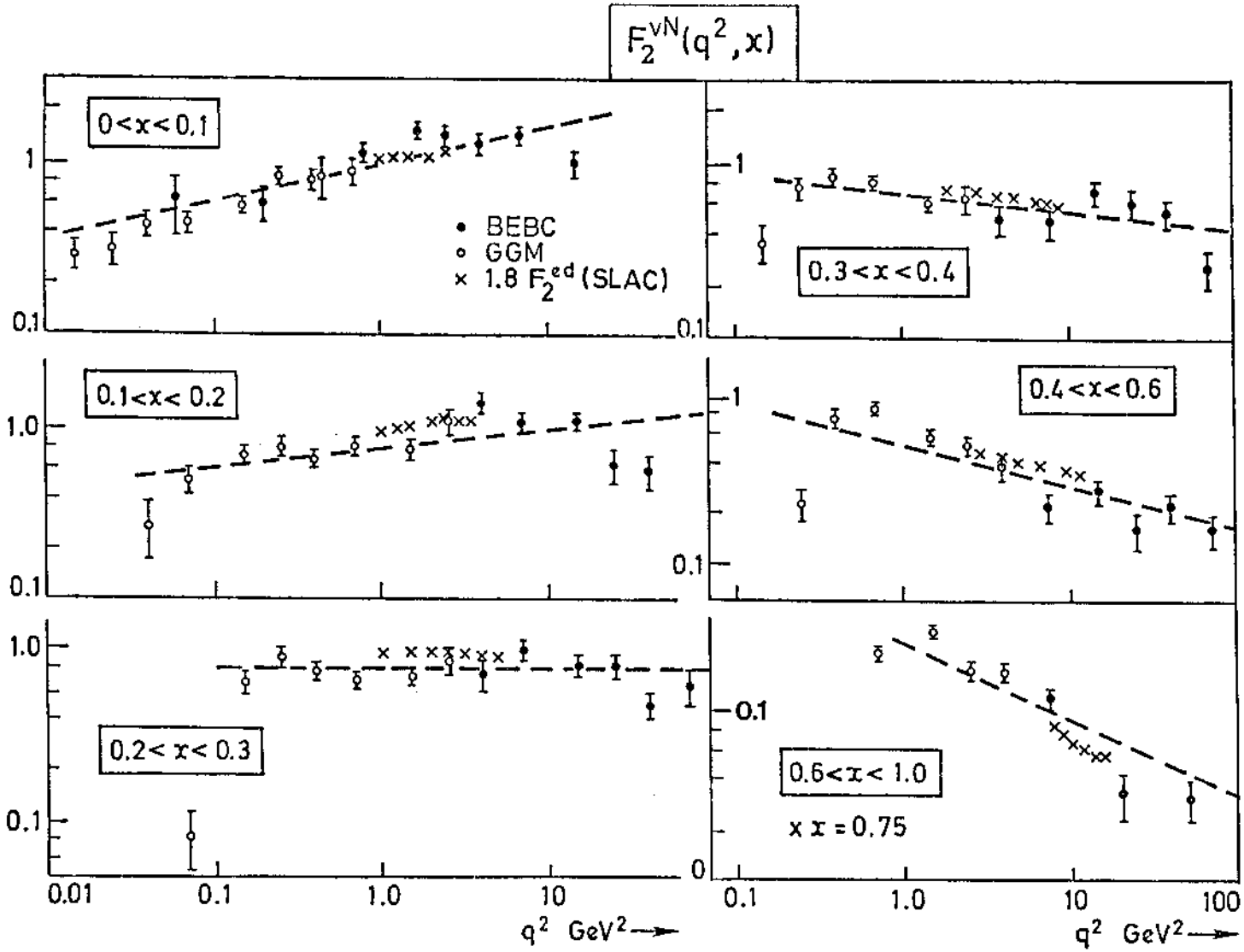

Fig. 16: $\ln F_2^{\nu N}$ for various x-ranges, as a function of $\ln Q^2$. GGM and BEBC points are shown separately. Results from SLAC (ed) scattering experiments are given for comparison, multiplied by a factor 1.8.

The straight lines indicate the slopes derived by Perkins et al. from an empirical fit to e/μ scattering data. Errors shown are statistical only.

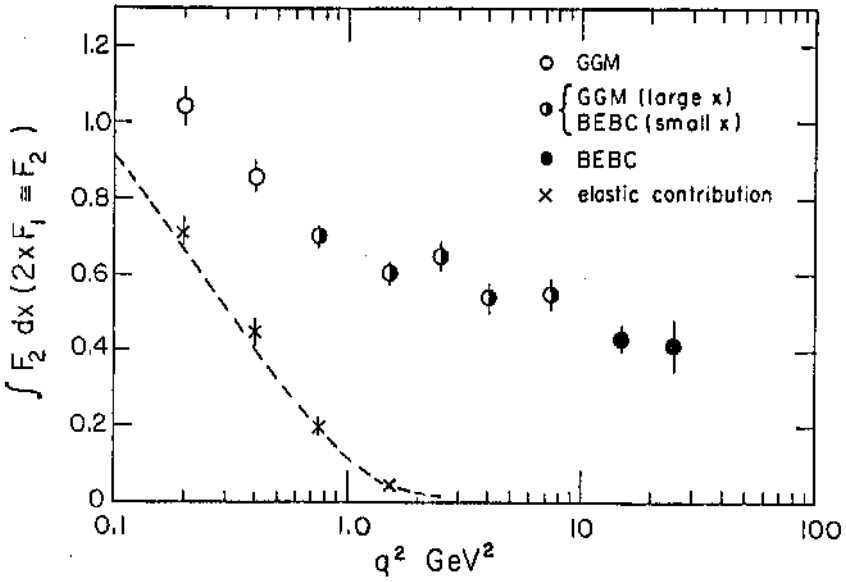

Fig. 17: $\int F_2(x,Q^2)dx$ plotted versus ln Q^2

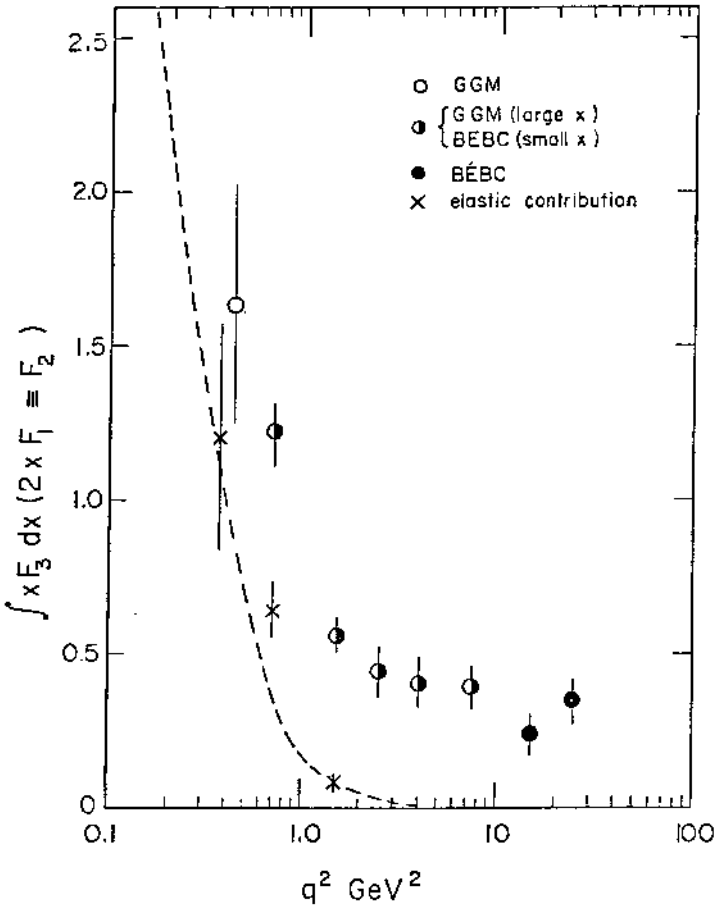

Fig. 18: $\int xF_3(x,Q^2)dx$ plotted versus ln Q^2

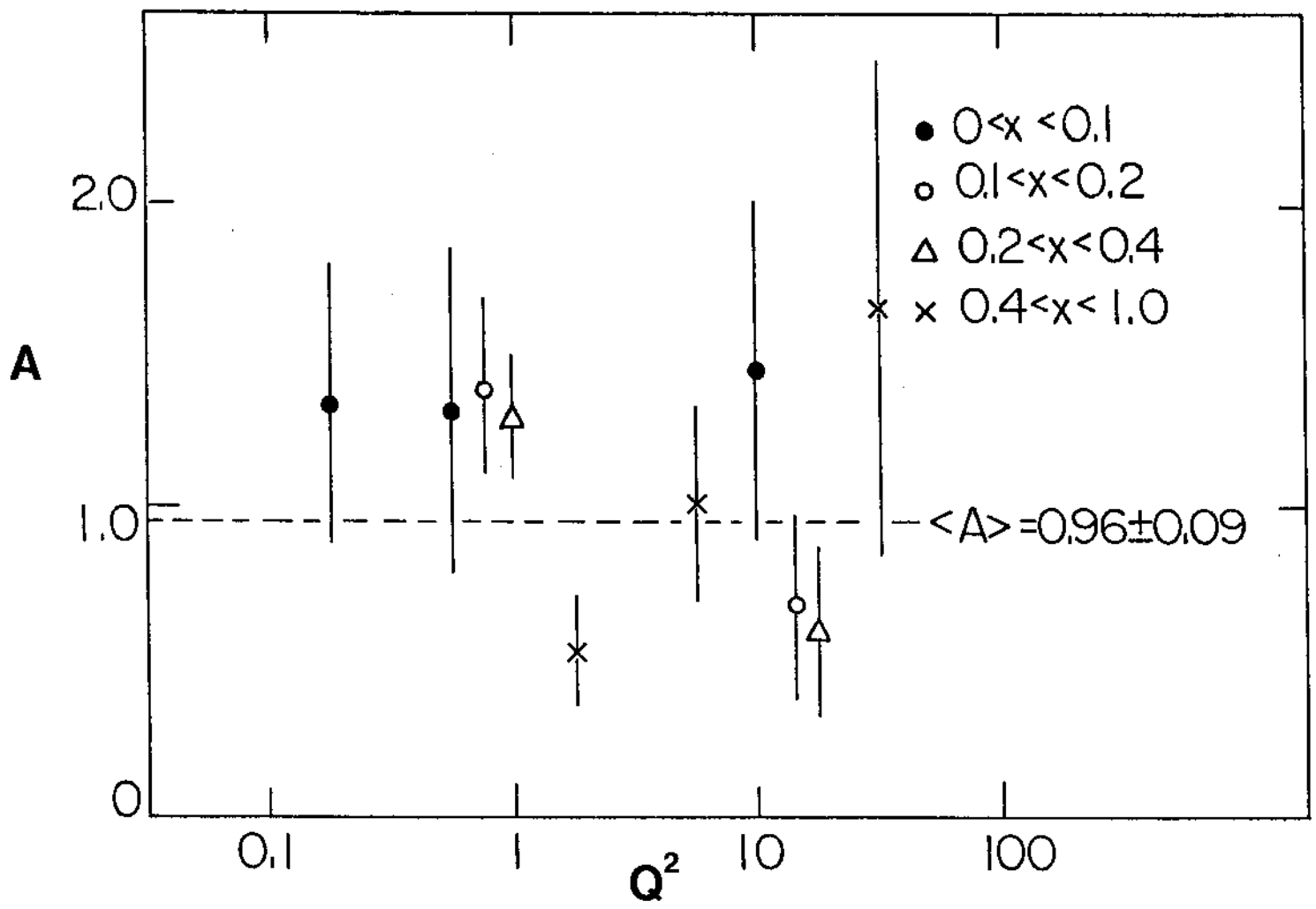

Fig. 19: A = $2xF_1/F_2$ versus ln Q^2, for various ranges of x
(GGM and BEBC data)

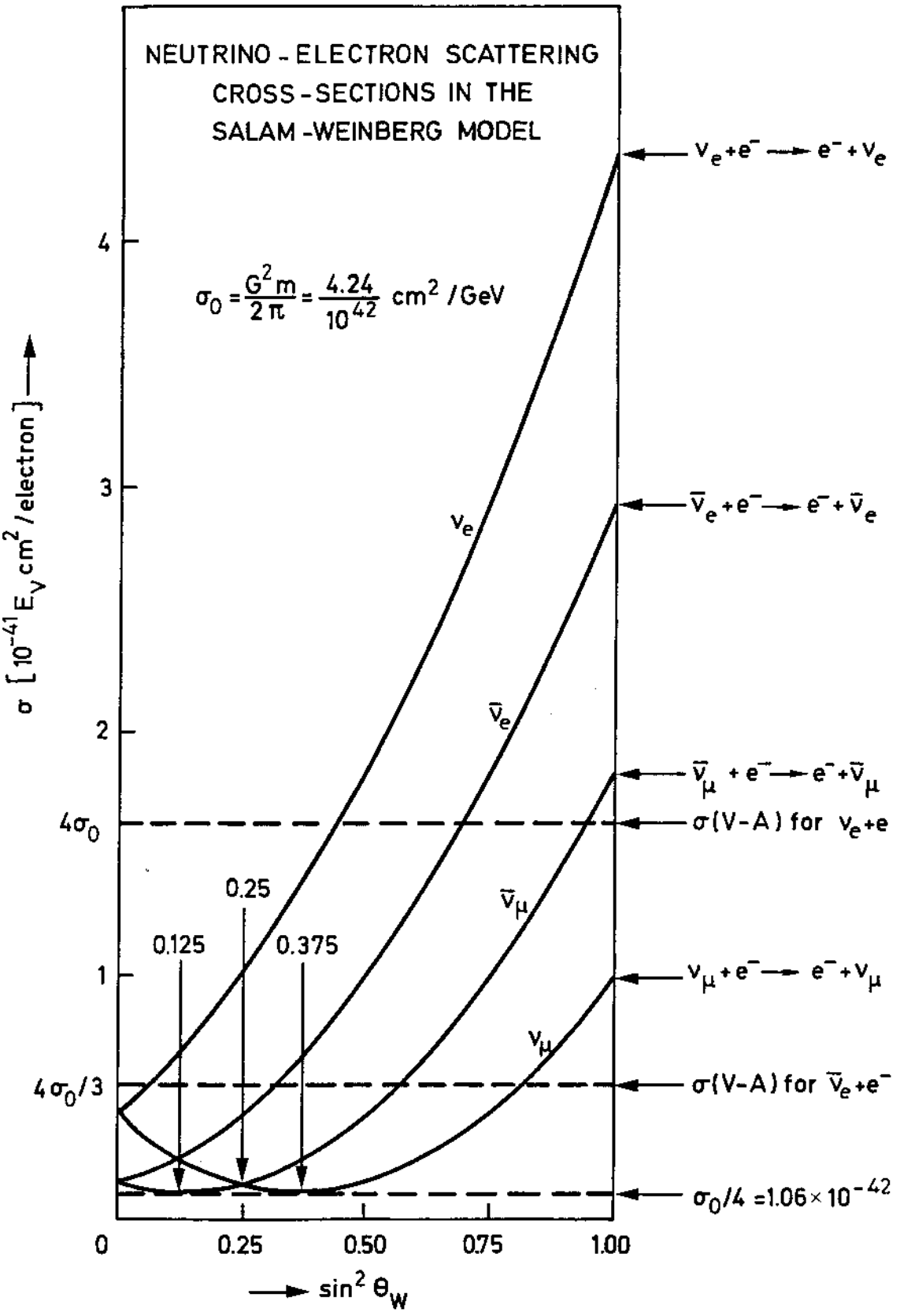

Fig. 20: Total cross-sections for neutrino-electron elastic scattering processes, in the Weinberg-Salam model, as function of $\sin^2\theta_w$.

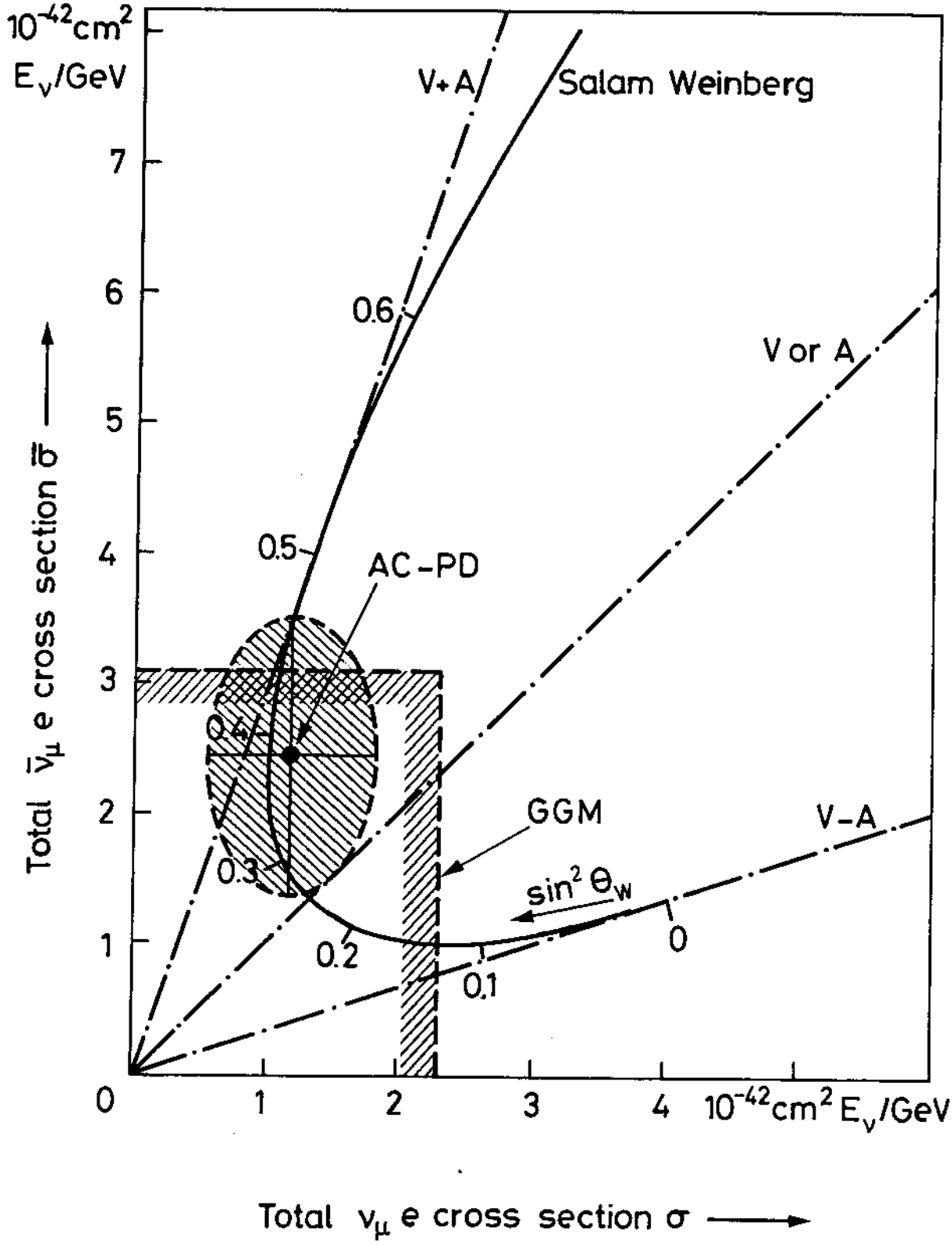

Fig. 21: $(\nu_\mu e)$ and $(\bar{\nu}_\mu e)$ total cross-sections (Aachen-Padova and GGM data). The straight lines denote V-A, V+A, and pure V or A interactions; the curve represents the prediction of the Weinberg-Salam model.

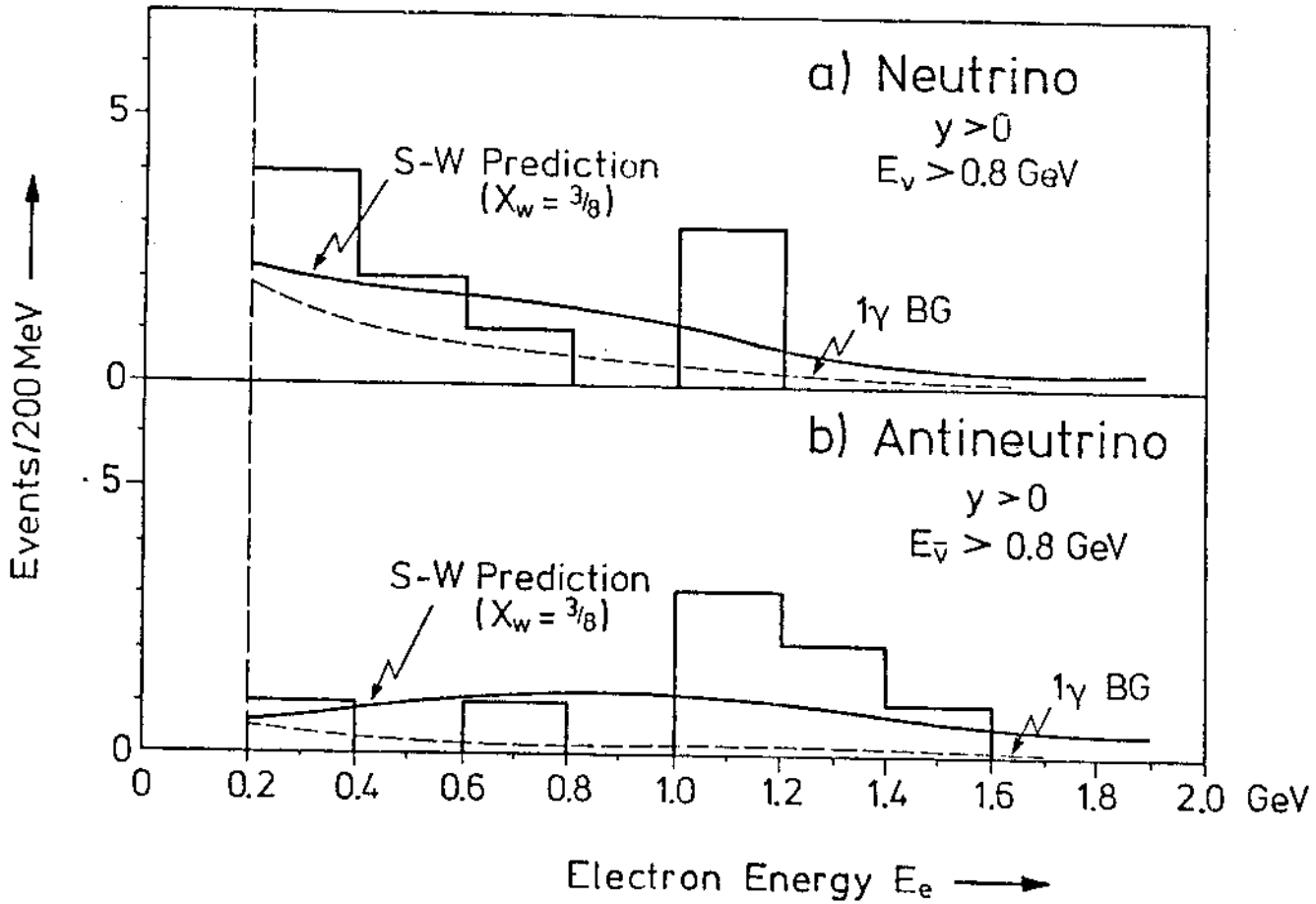

Fig. 22: Electron energy distributions for a) $\nu_\mu e$ and b) $\bar{\nu}_\mu e$ scattering (Aachen-Padova experiment). The full line is the sum of the expected distribution of the Weinberg-Salam model for $\sin^2\theta_w = 3/8 \simeq 0.38$, and background.

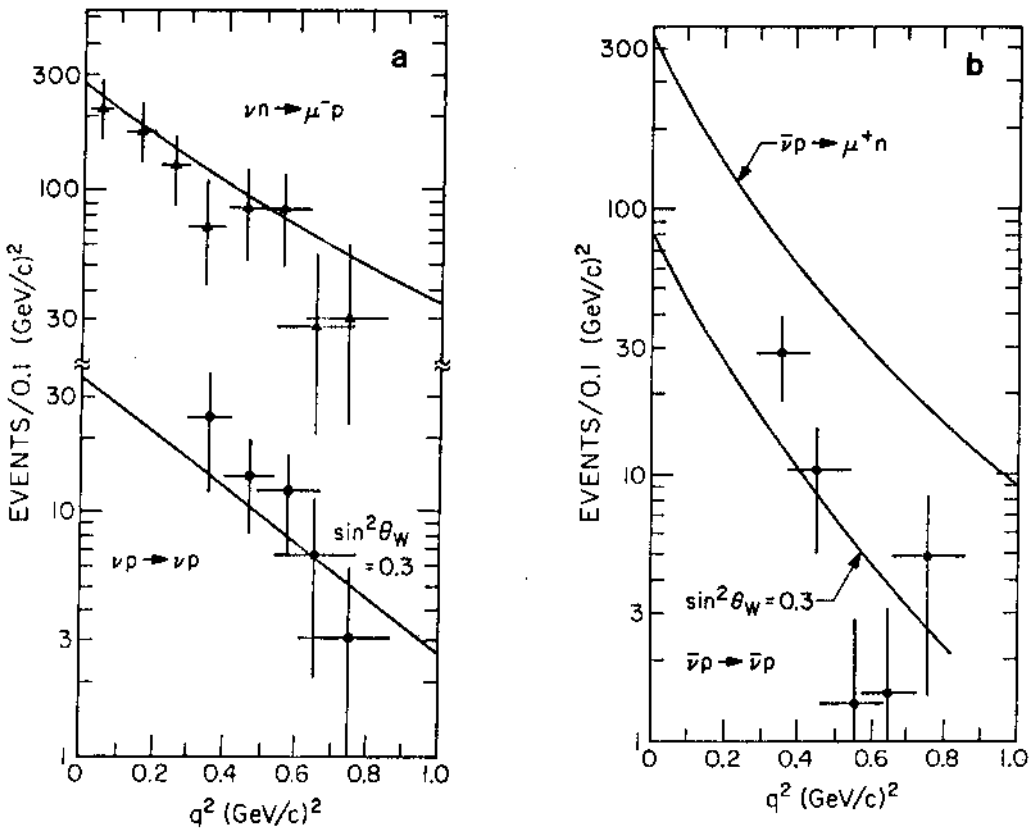

Fig. 23: $\nu_\mu p$ (a) and $\bar{\nu}_\mu p$ (b) scattering data versus Q^2 (HPW data).

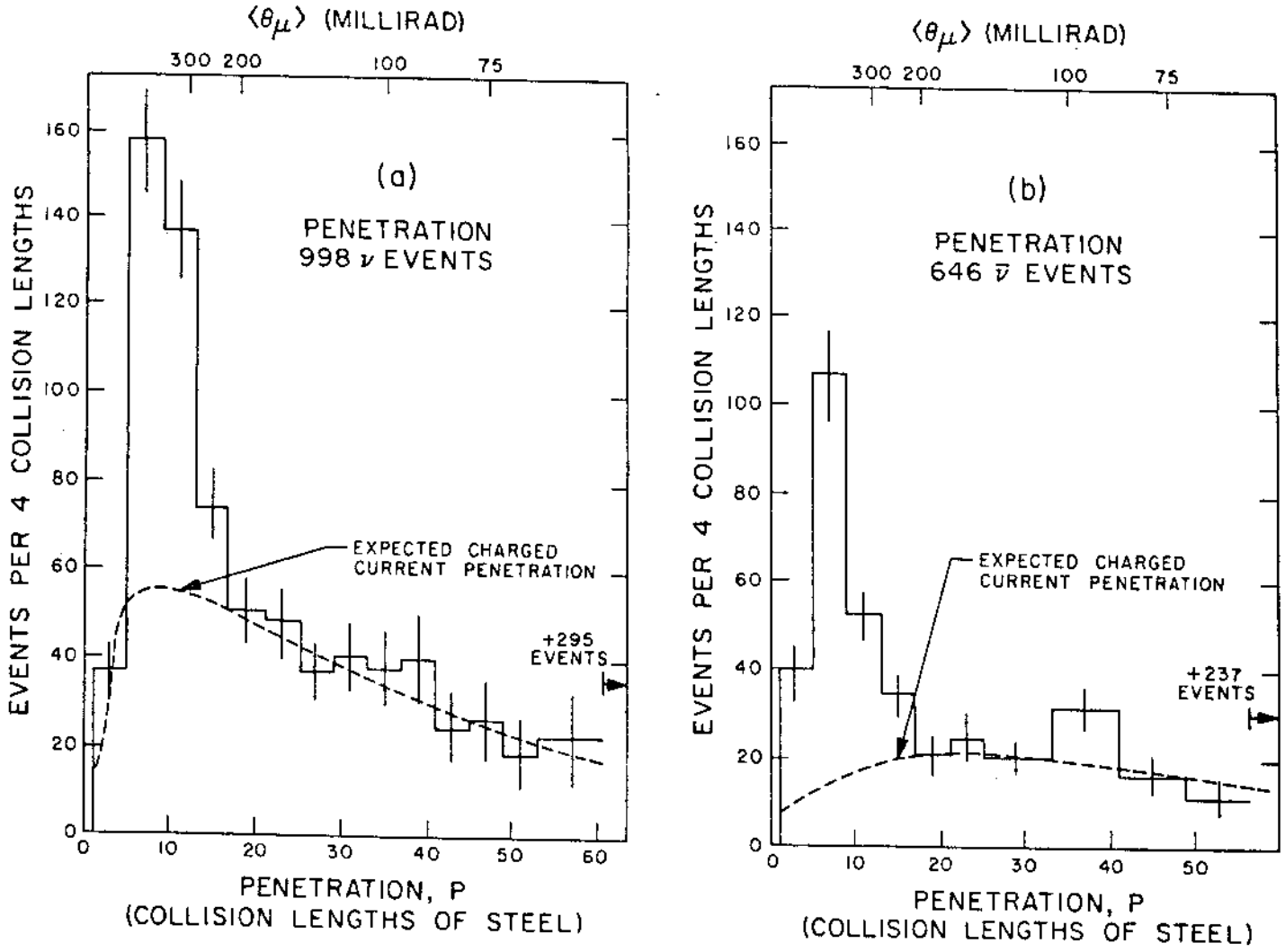

Fig. 24: Event length distribution of ν and $\bar{\nu}$ events in iron (CITF data). The collision length in iron is $\sim$ 15 cm.

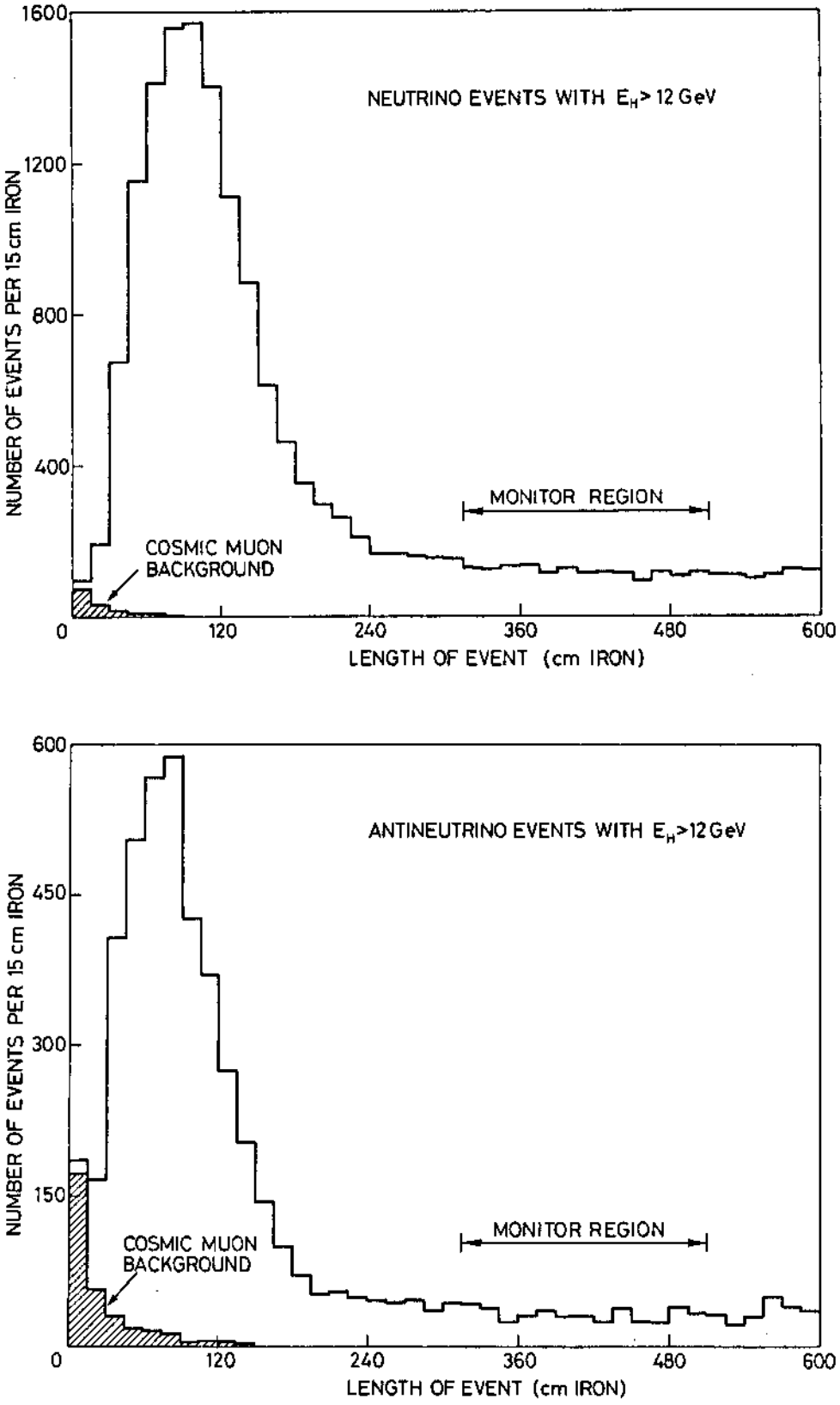

Fig. 25: Event length distribution of ν and $\bar{\nu}$ events in iron (CDHS data). The plot shows raw data, before cosmic and WBB background subtraction.

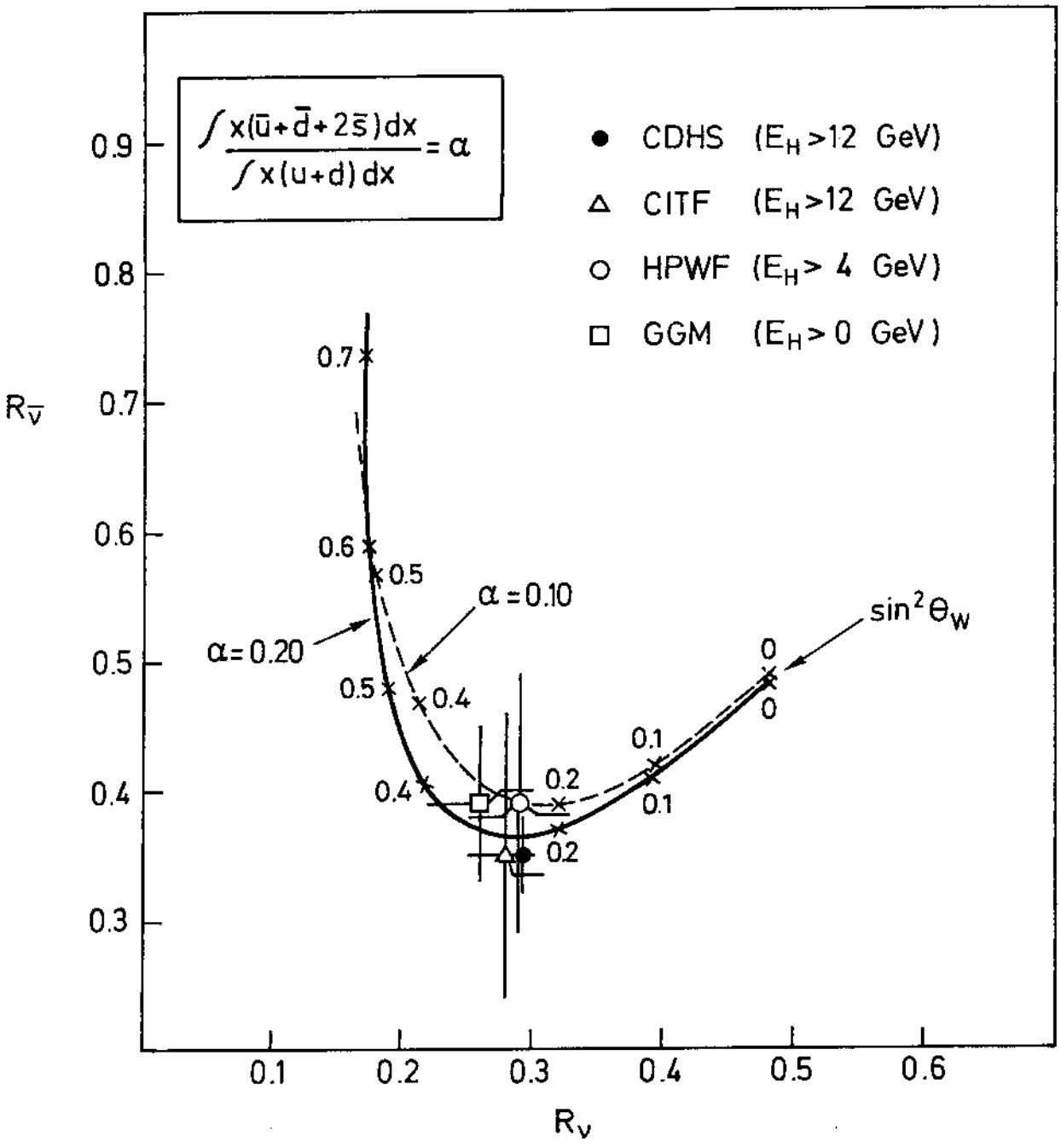

Fig. 26: Results for R_ν and $R_{\bar{\nu}}$ from different experiments. The two curves give the Weinberg-Salam prediction for the experimental conditions of the CDHS experiment (E_H > 12 GeV, iron target), for 10 and 20% relative amount of antiquark.

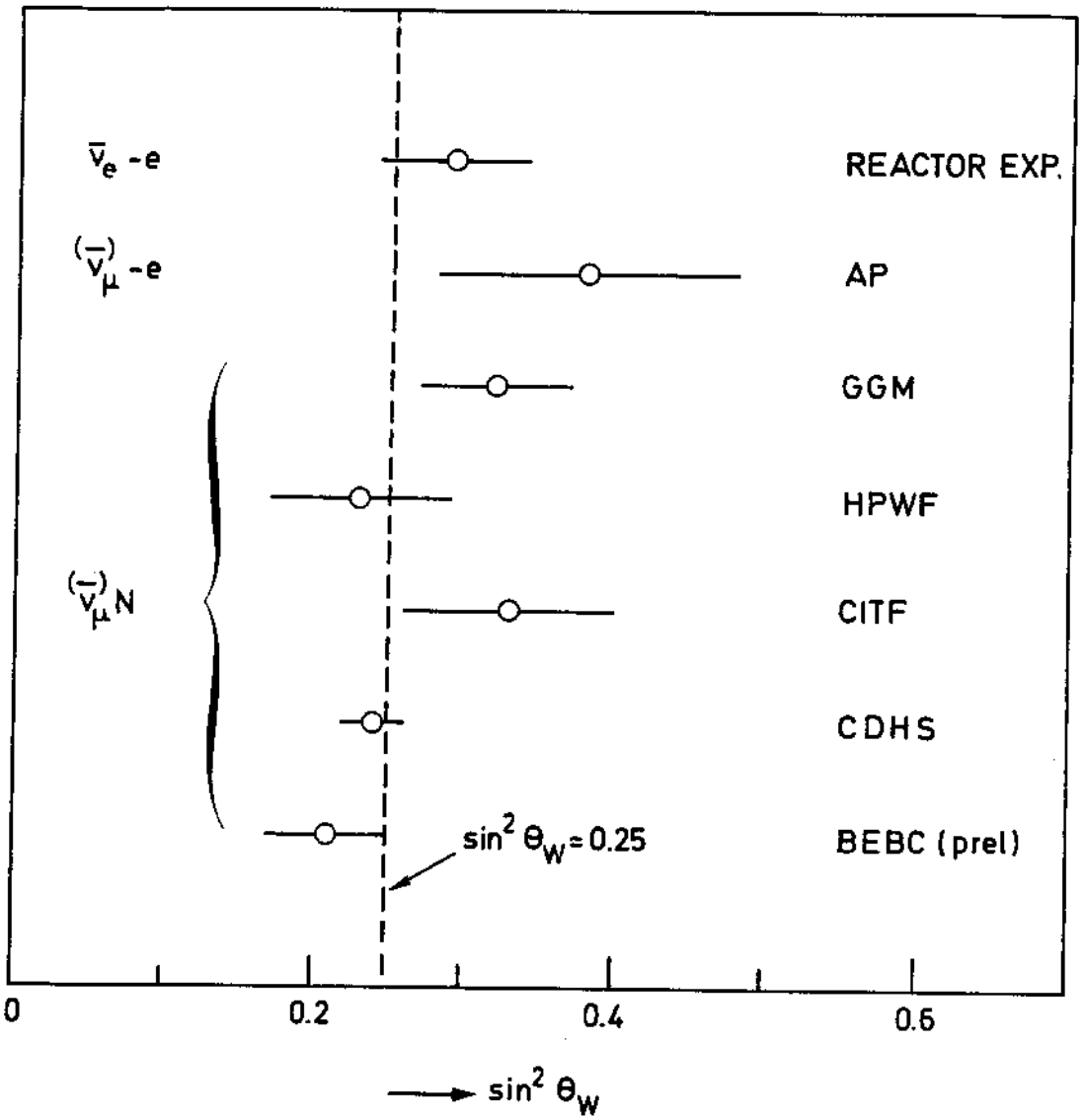

Fig. 27: Recent results of different experiments on $\sin^2\theta_w$.

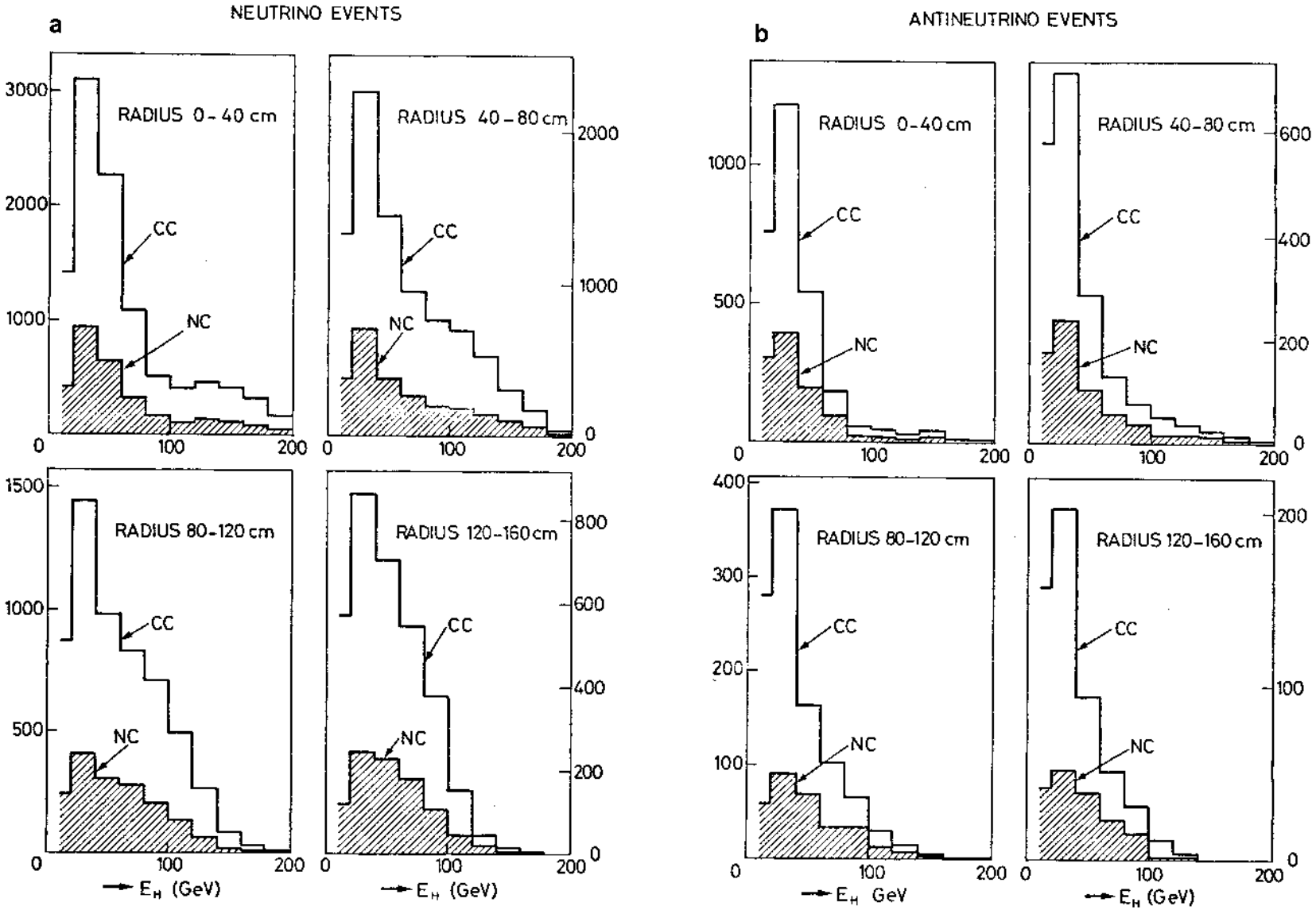

Fig. 28: Hadron energy distributions of NC and CC events for different radial bins (Fig. 28a for neutrinos, Fig. 28b for antineutrinos; CDHS data).

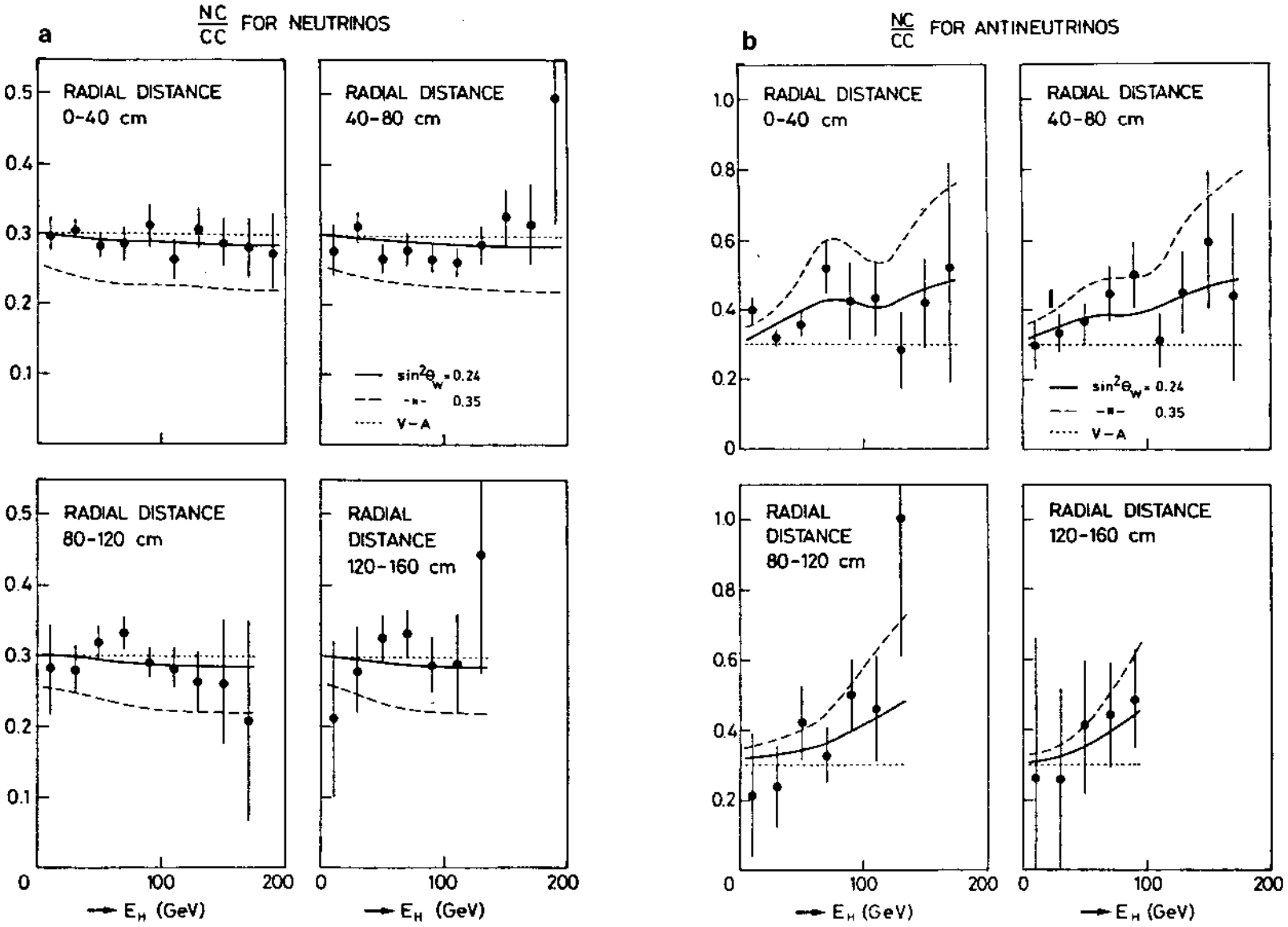

Fig. 29: Ratio of the NC to CC cross-sections as a function of the hadron energy, for different radial bins, for neutrinos (a) and antineutrinos (b). The lines represent the predictions of pure V-A coupling and of the Weinberg-Salam model (CDHS data).

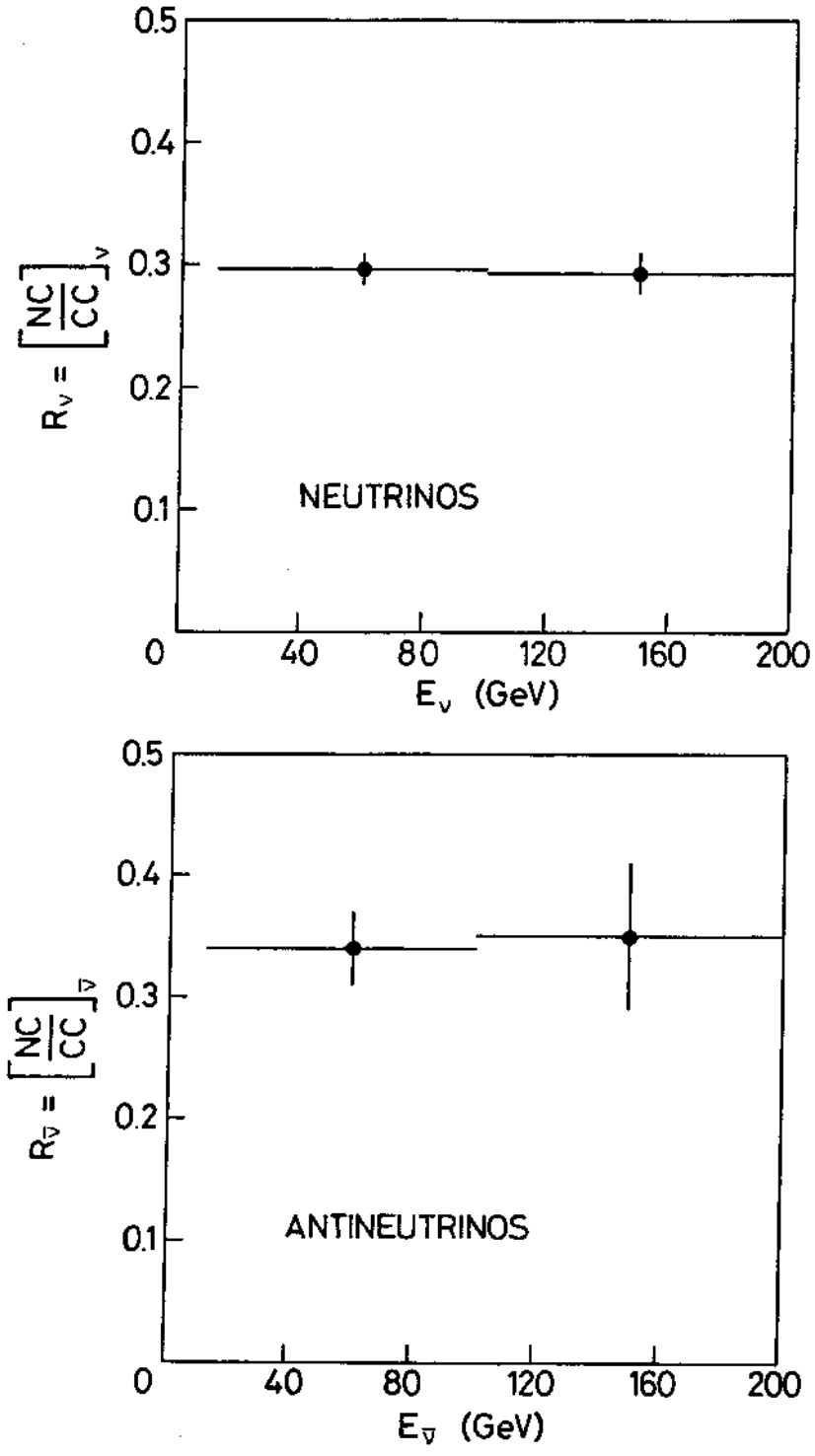

Fig. 30: R_ν and $R_{\bar{\nu}}$ versus neutrino energy (CDHS data).

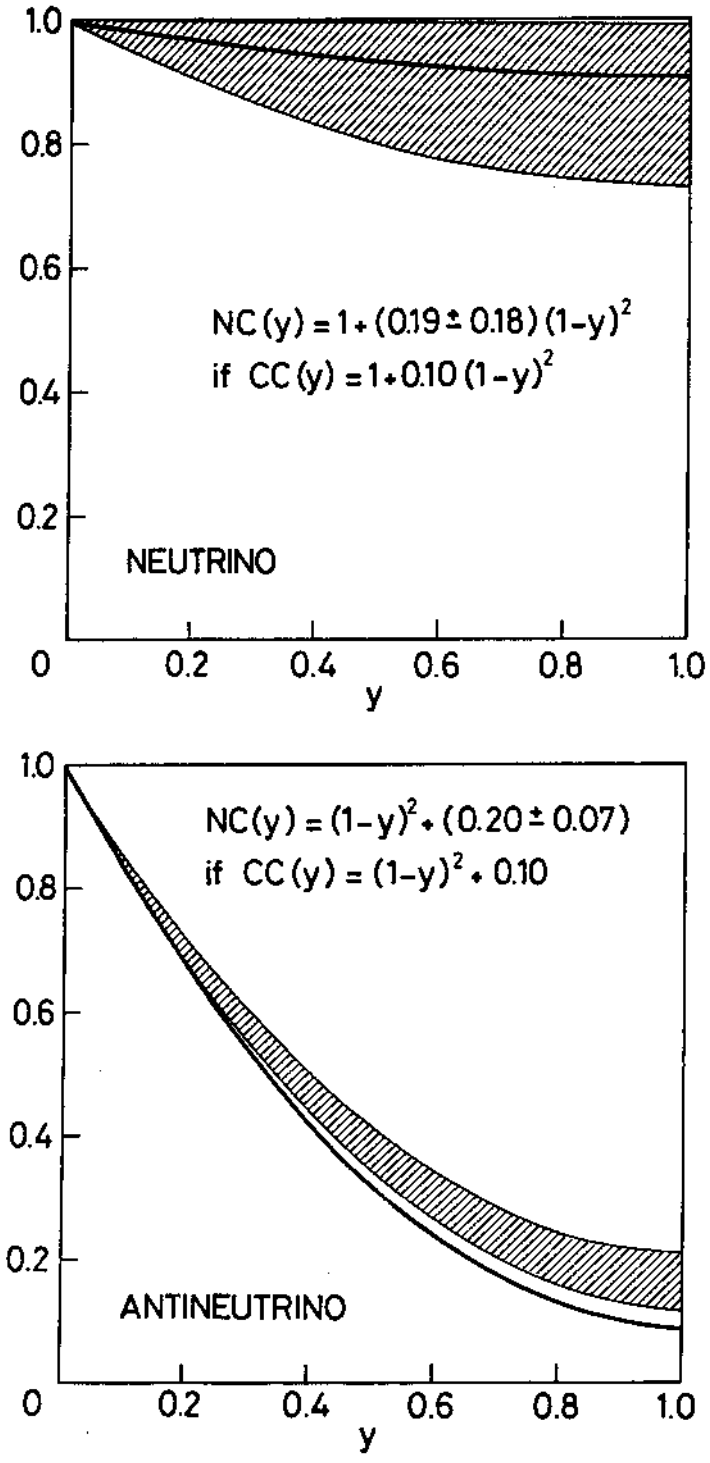

Fig. 31: Illustration of the fitted shape of the NC y-distribution, with reference to an assumed shape of the CC y-distribution. The shaded area includes the $\pm 1\sigma$ domain (CDHS data). ν and $\bar{\nu}$ data have been fitted separately.

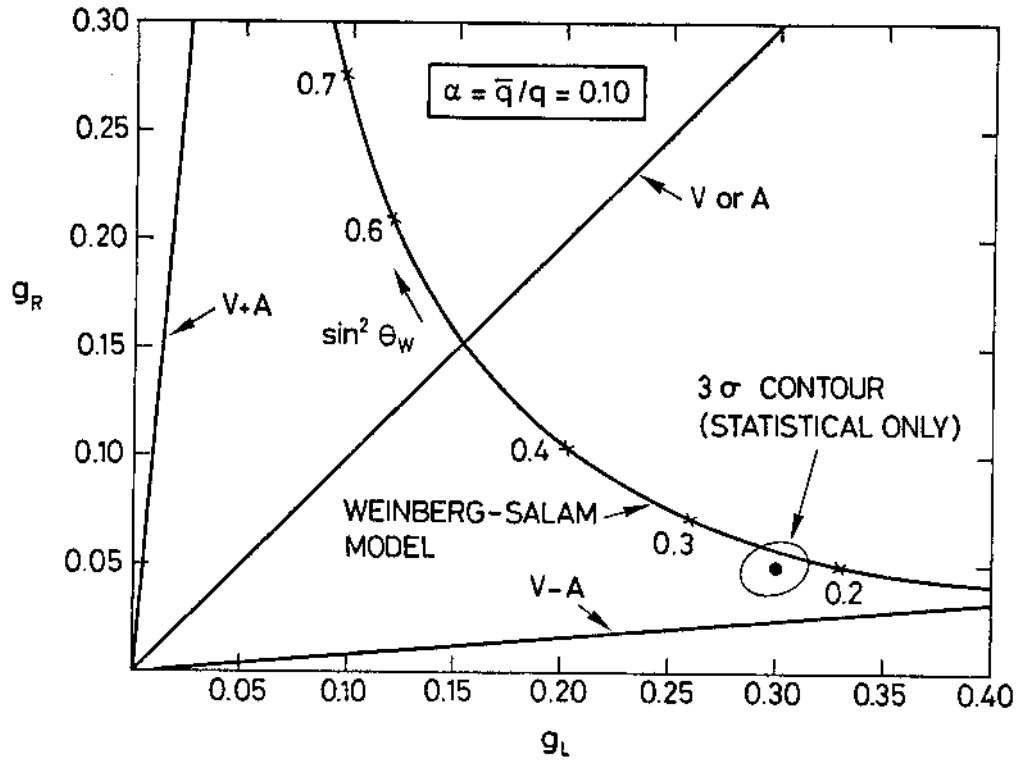

Fig. 32: Comparison of model predictions and the CDHS result on g_L and g_R. The relative amount of the sea is assumed to be 0.10.

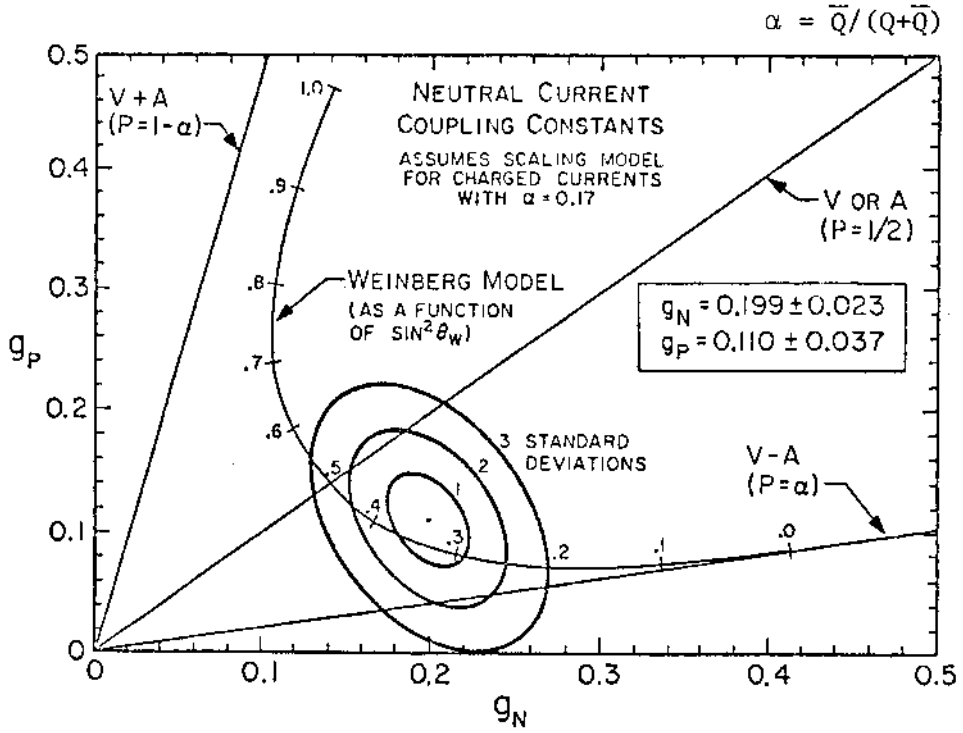

Fig. 33: Comparison of model predictions and the CITF result on g_N and g_P (same as g_L and g_R of Fig. 32). The relative amount of the sea is 0.17 as measured by CITF.

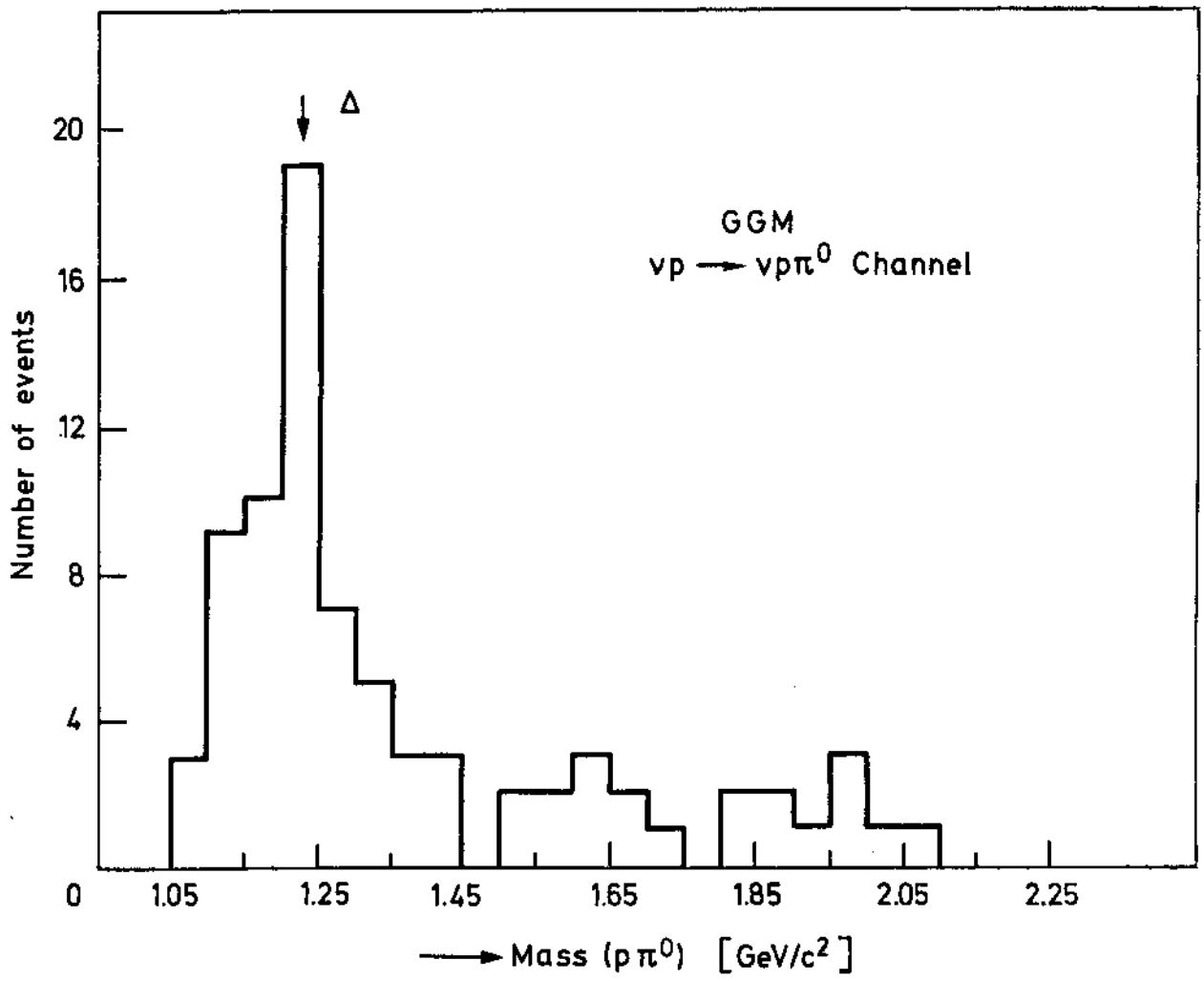

Fig. 34: Spectrum of invariant ($p\pi^0$) masses in the NC reaction $\nu p \to \nu p\pi^0$ (GGM data).

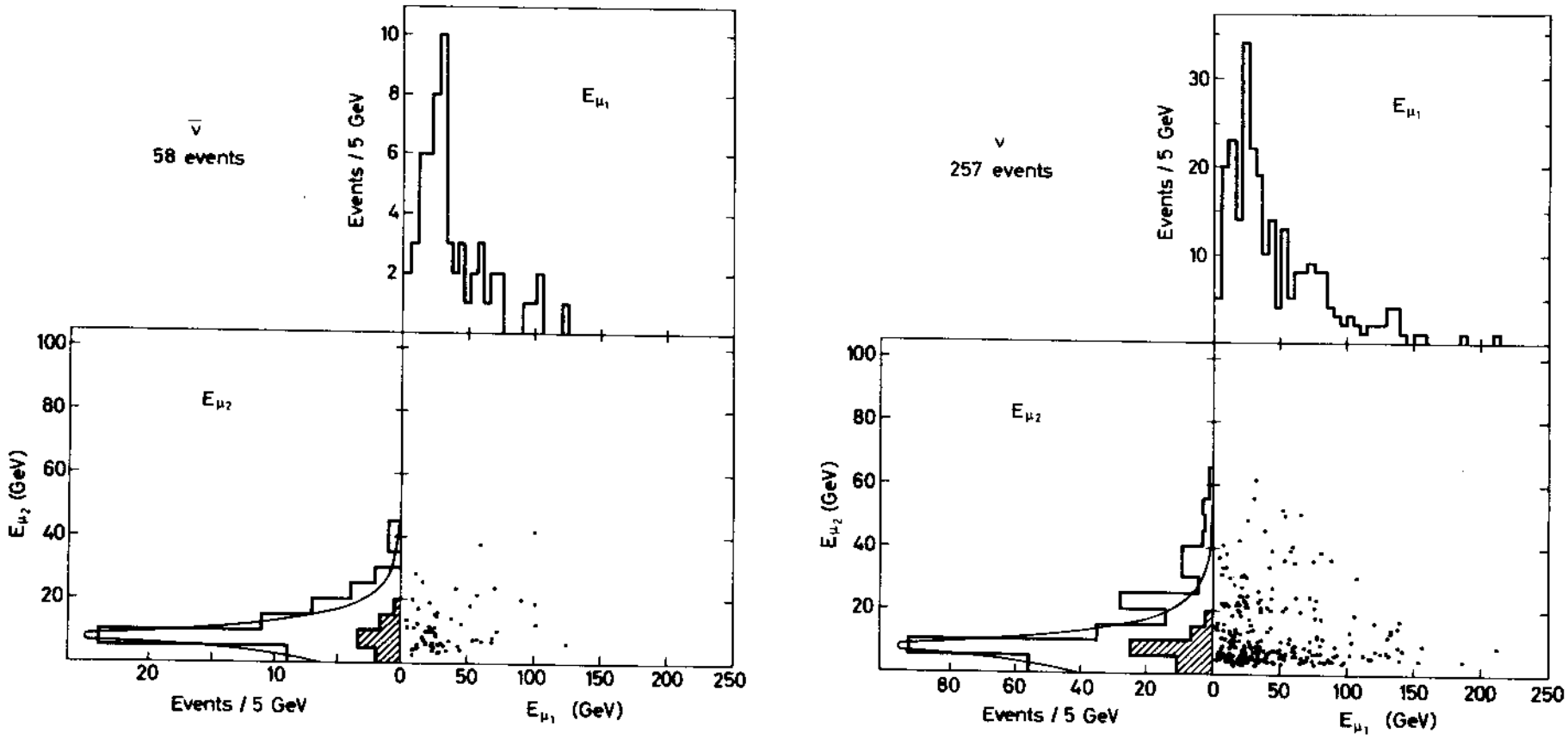

Fig. 35: Scatter plot of opposite-sign 2μ events, with projections of $E_{\mu 1}$ and $E_{\mu 2}$, for ν and $\bar{\nu}$ events. In the $E_{\mu 2}$ projection, $\pi(K) \rightarrow \mu$ background is shown as hatched area, together with the charm model prediction (CDHS data).

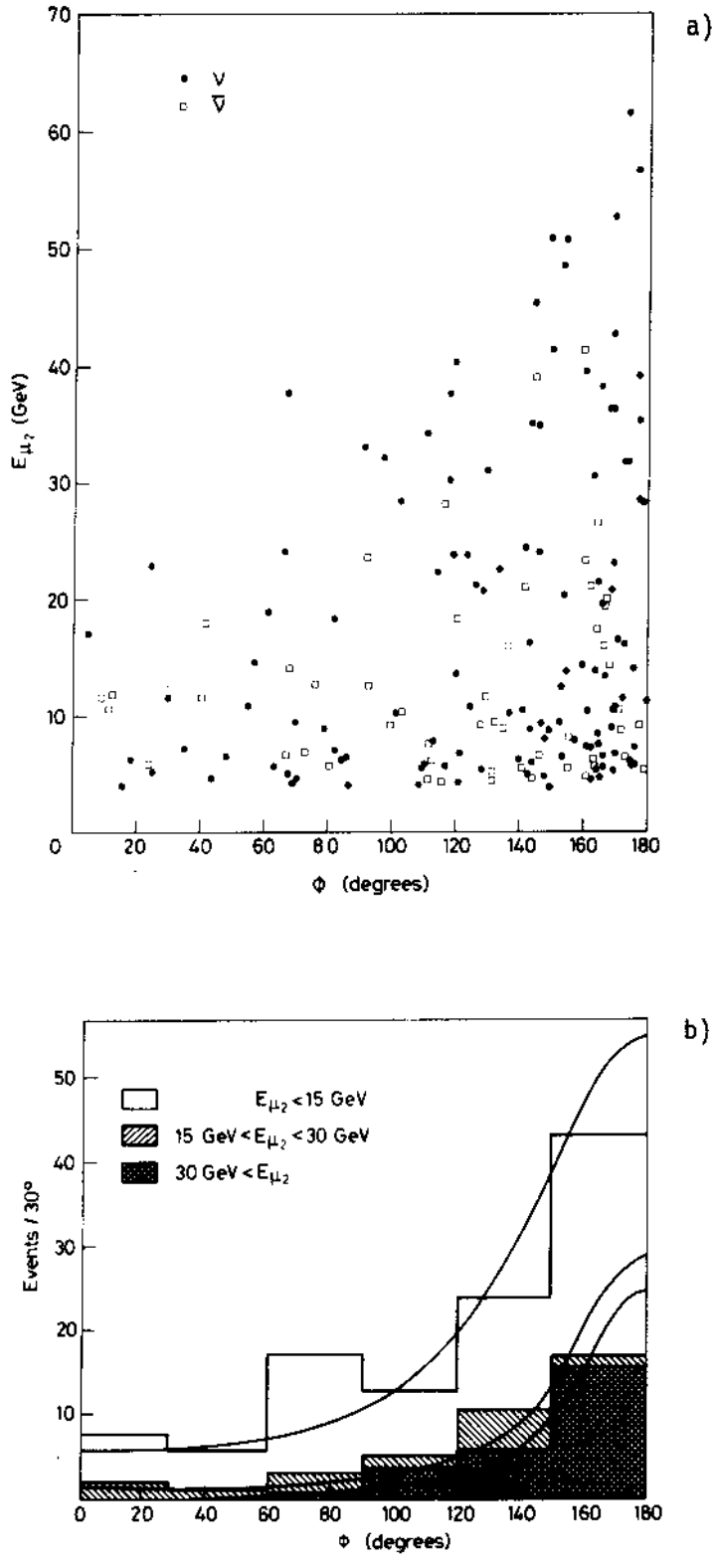

Fig. 36: Scatter plot of the azimuthal angle difference $\Delta\phi$ and $E_{\mu 2}$ (a), and projection (b). The predictions of a charm model are shown in the projections (CDHS data).

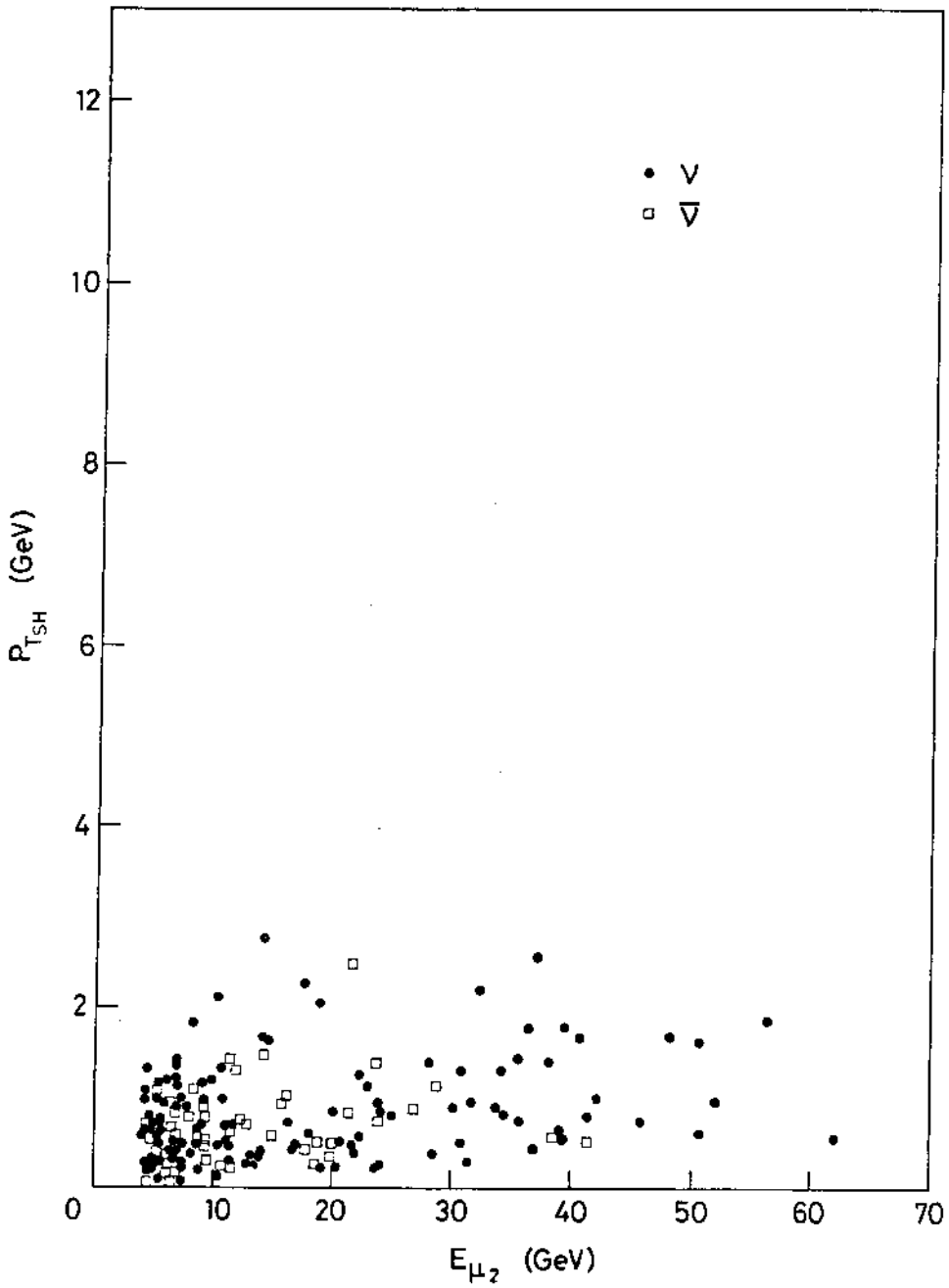

Fig. 37: Scatter plot of the p_T of the second muon with respect to the direction of the hadron shower, versus the energy of the second muon (CDHS data).

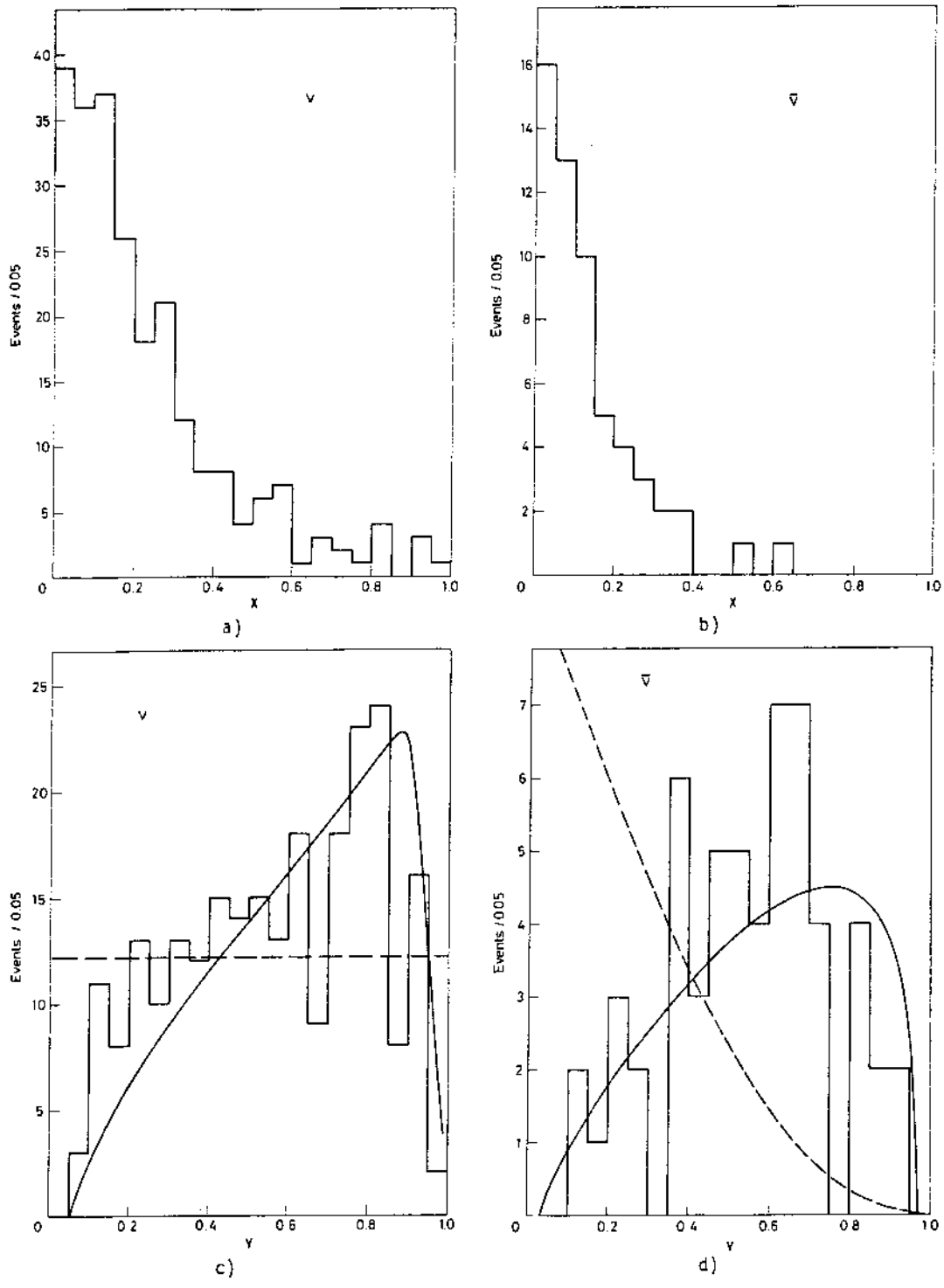

Fig. 38: x- and y-distribution for ν and $\bar{\nu}$ opposite-sign 2μ events. The expectations for a flat y-distribution as predicted by the charm model are shown (CDHS data).

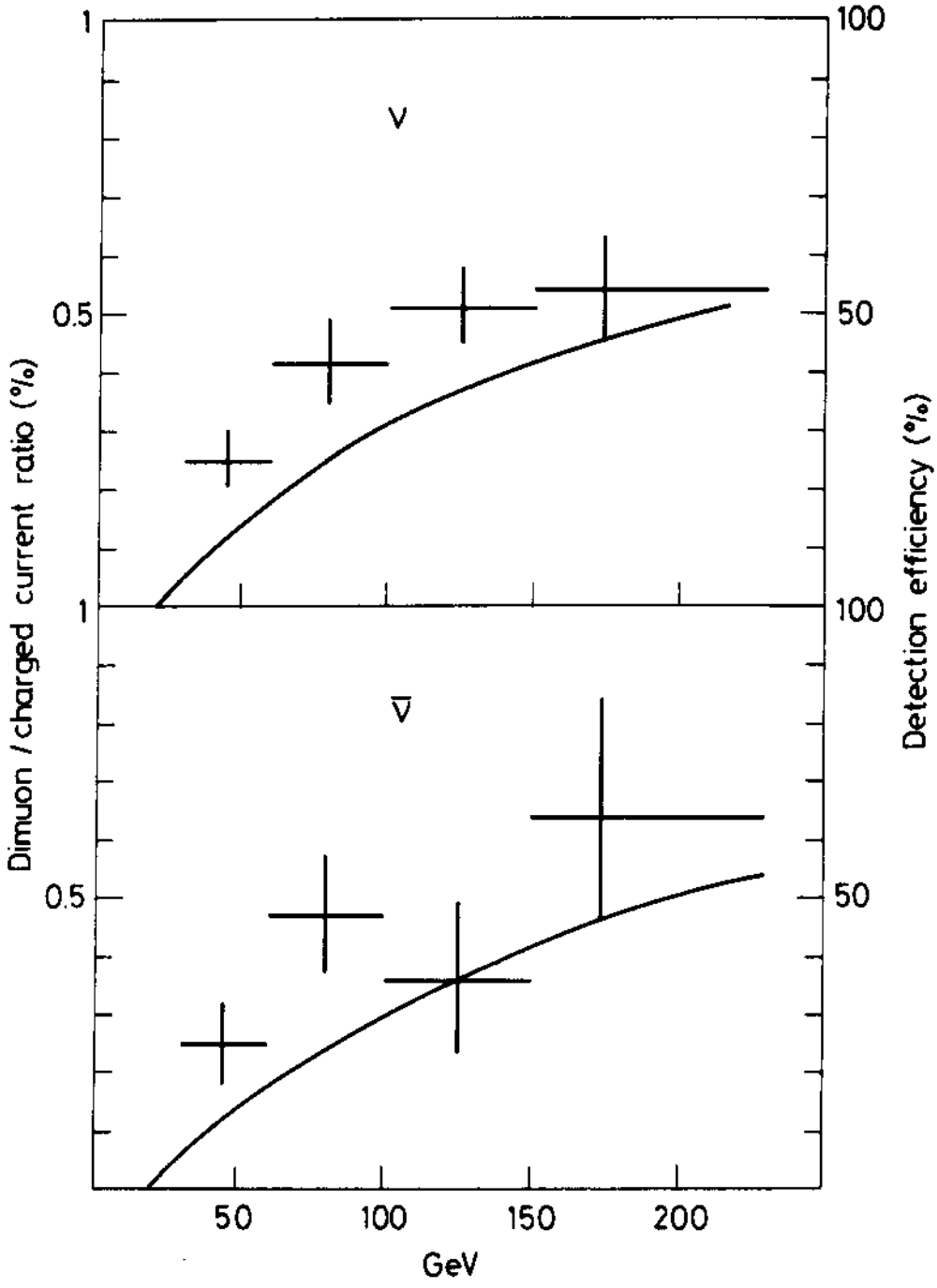

Fig. 39: The ratio of the observed opposite-sign 2μ rates to single muon CC rates, versus neutrino energy. The full lines denote the calculated efficiencies in a charm model (CDHS data).

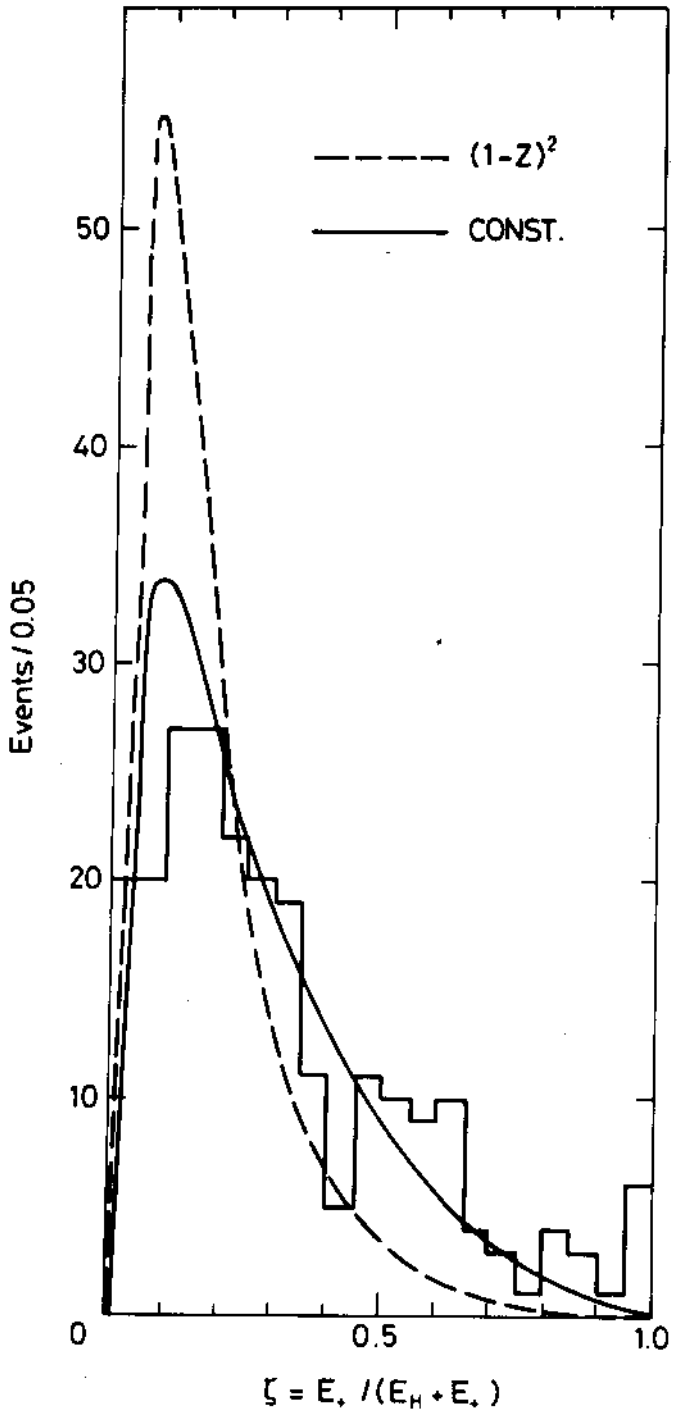

Fig. 40: $E_+/(E_H + E_+)$ distribution of ν-induced opposite-sign 2μ events. The predictions of a charm model with different fragmentation functions are superimposed (Odorico, Ref. 53; data from CDHS).

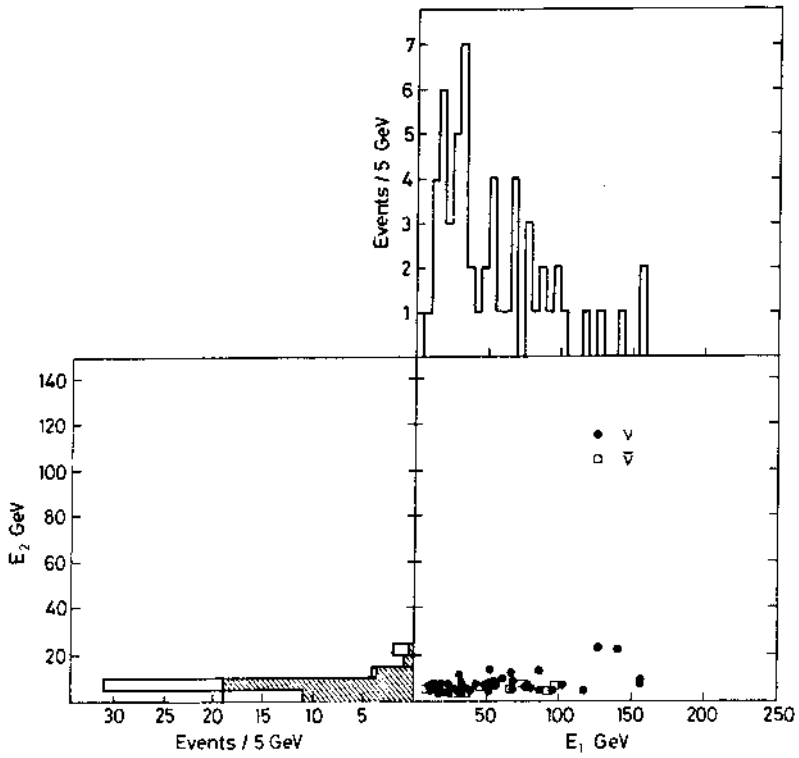

Fig. 41: Scatter plot of like-sign 2μ events, with projections of $E_{\mu 1}$ and $E_{\mu 2}$, for ν and $\bar{\nu}$ events. In the $E_{\mu 2}$ projection $\pi(K) \rightarrow \mu$ background is shown as hatched area (CDHS data).

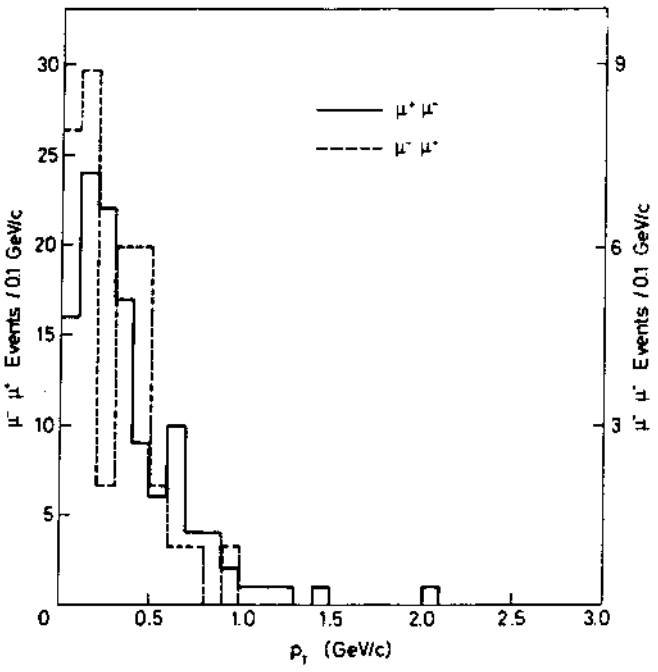

Fig. 42: p_T distribution for like-sign 2μ events (CDHS data).

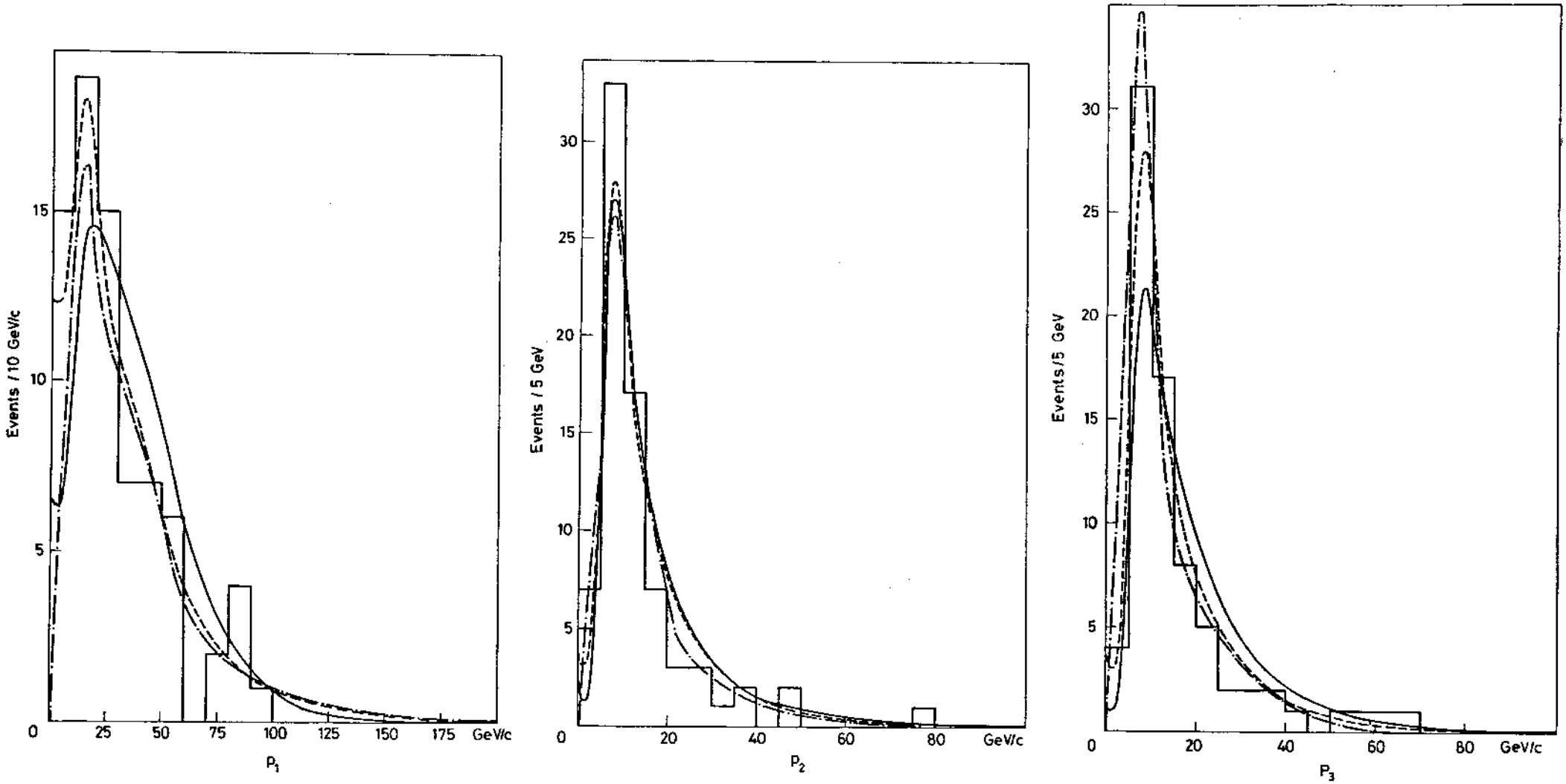

Fig. 43: Momentum distribution of all three muons of 3μ events (CDHS data).

Here and in all subsequent plots up to Fig. 50 the smooth lines give the expected distributions (normalized to the number of observed events) for:

----- = hadronic pair production
-•-•- = internal bremsstrahlung
——— = heavy lepton cascade (M_{L^-} = 9 GeV, M_{L^0} = 1.5 GeV)
••••• = heavy quark cascade

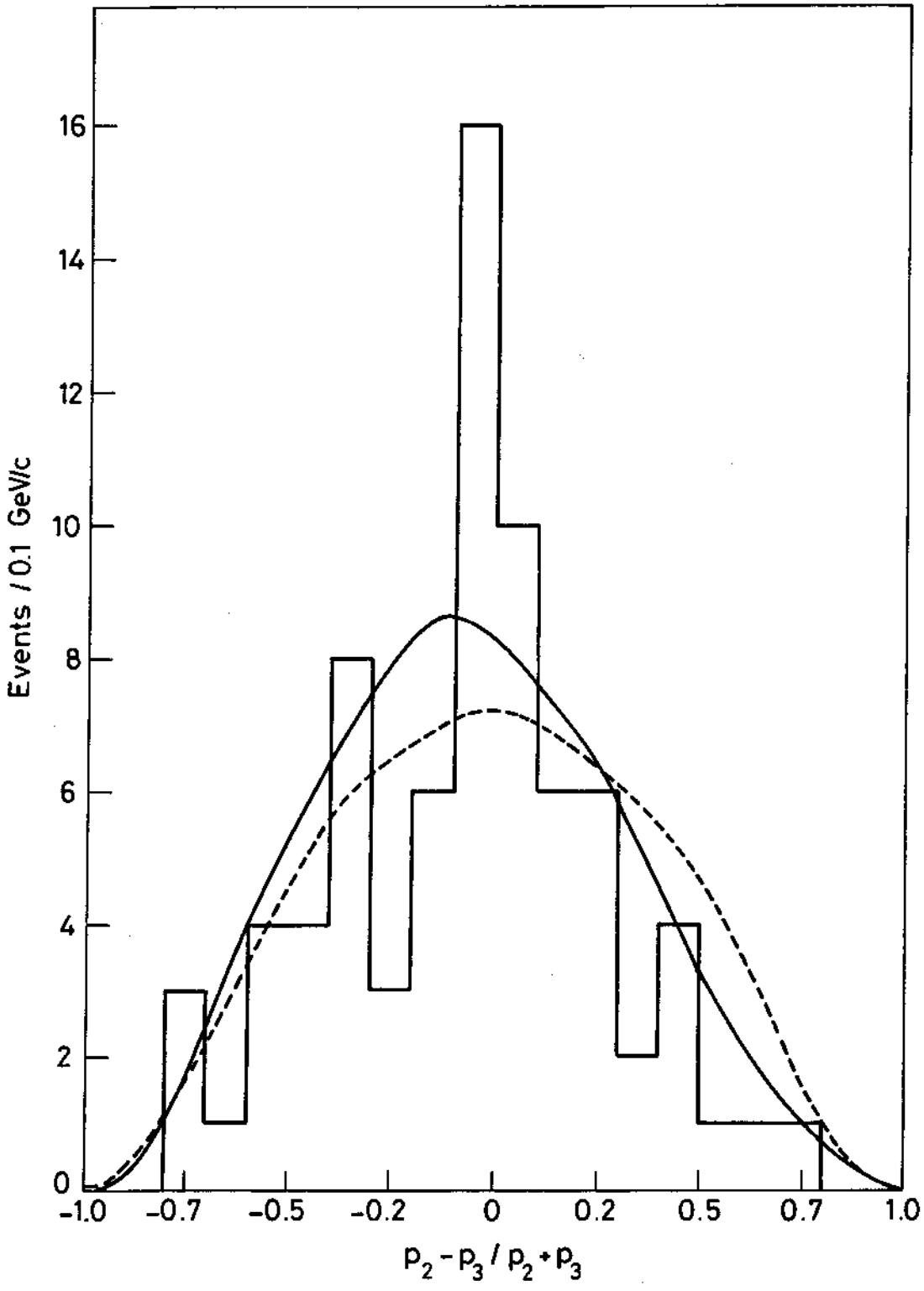

Fig. 44: Momentum asymmetry of the two non-leading muons (CDHS data).

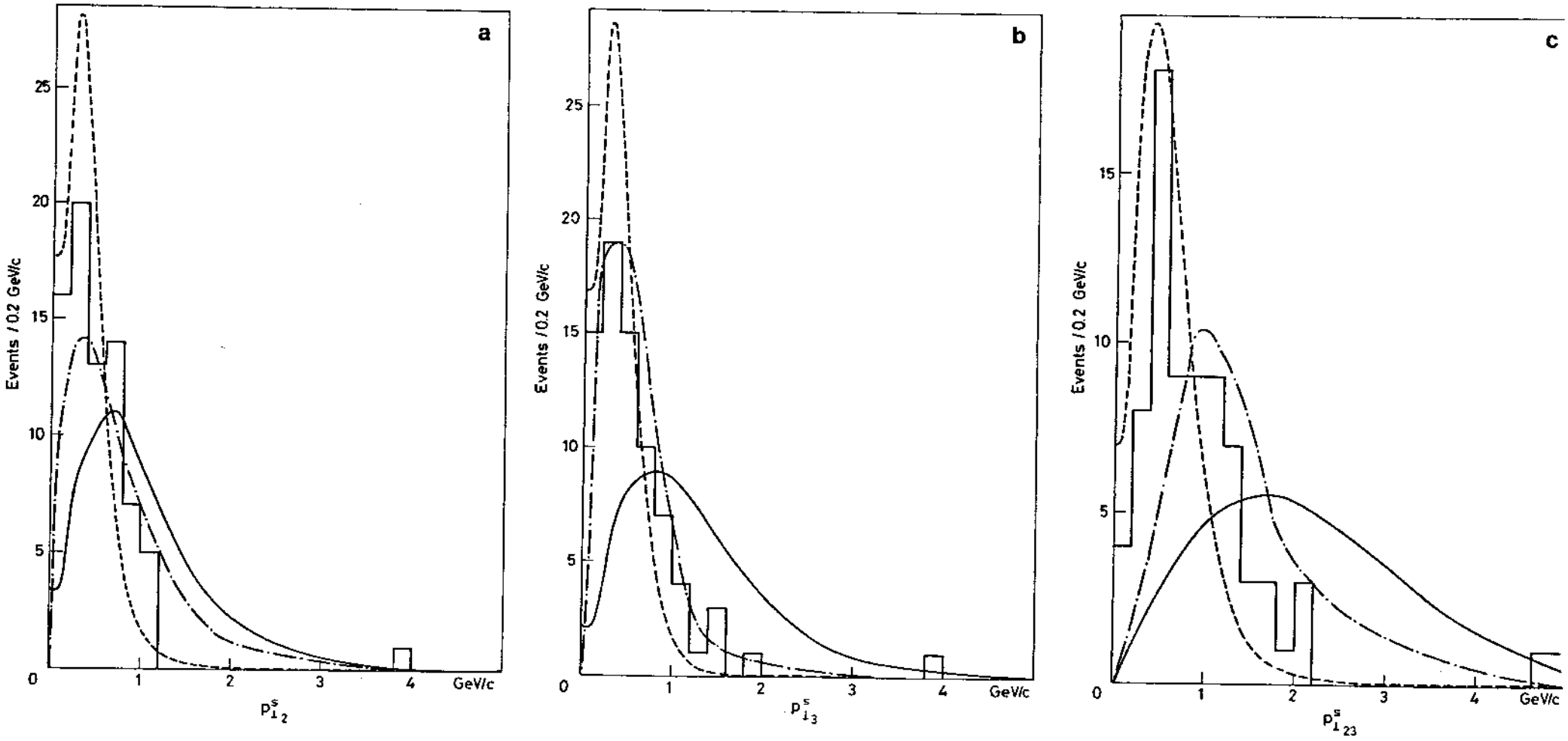

Fig. 45: p_T distribution of the two non-leading muons, and of their vectorial sum, with respect to the direction of the hadron shower (CDHS data).

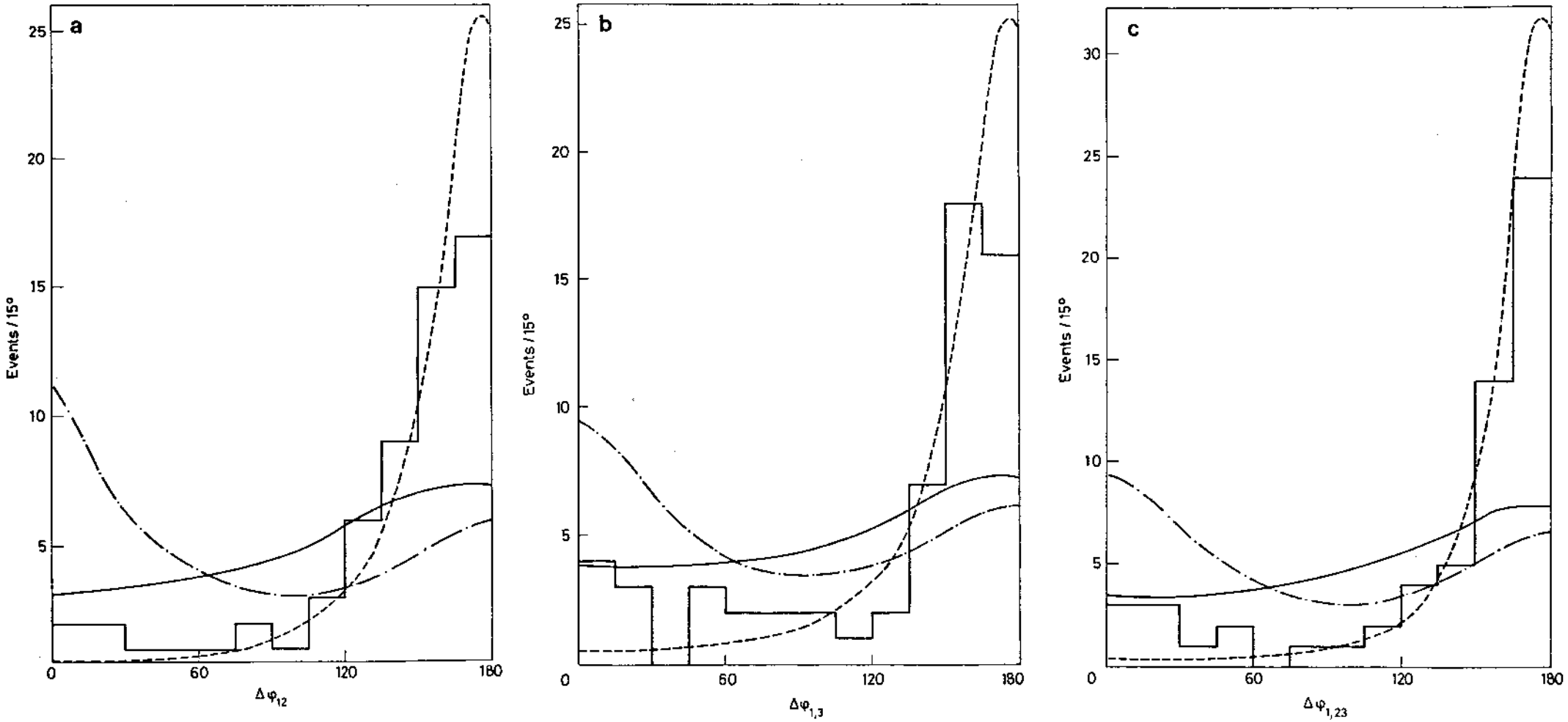

Fig. 46: Difference $\Delta\phi$ in the azimuthal angles of the projections of the muons on the plane perpendicular to the incident neutrino, between the leading muon (μ_1) and both non-leading muons, and their vectorial sum (CDHS data).

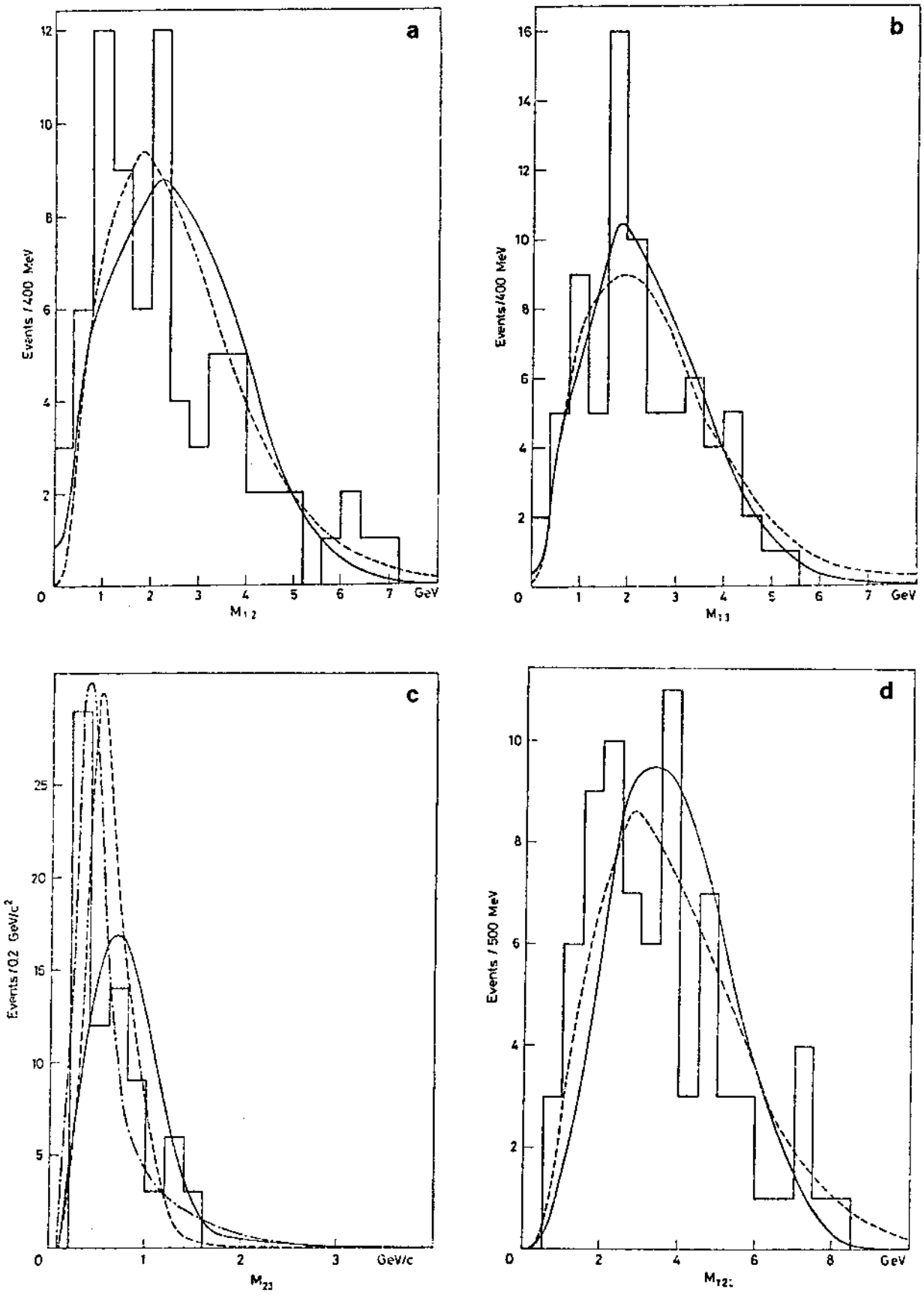

Fig. 47: Mass distributions for all three dimuon masses, and for the 3μ mass (CDHS data).

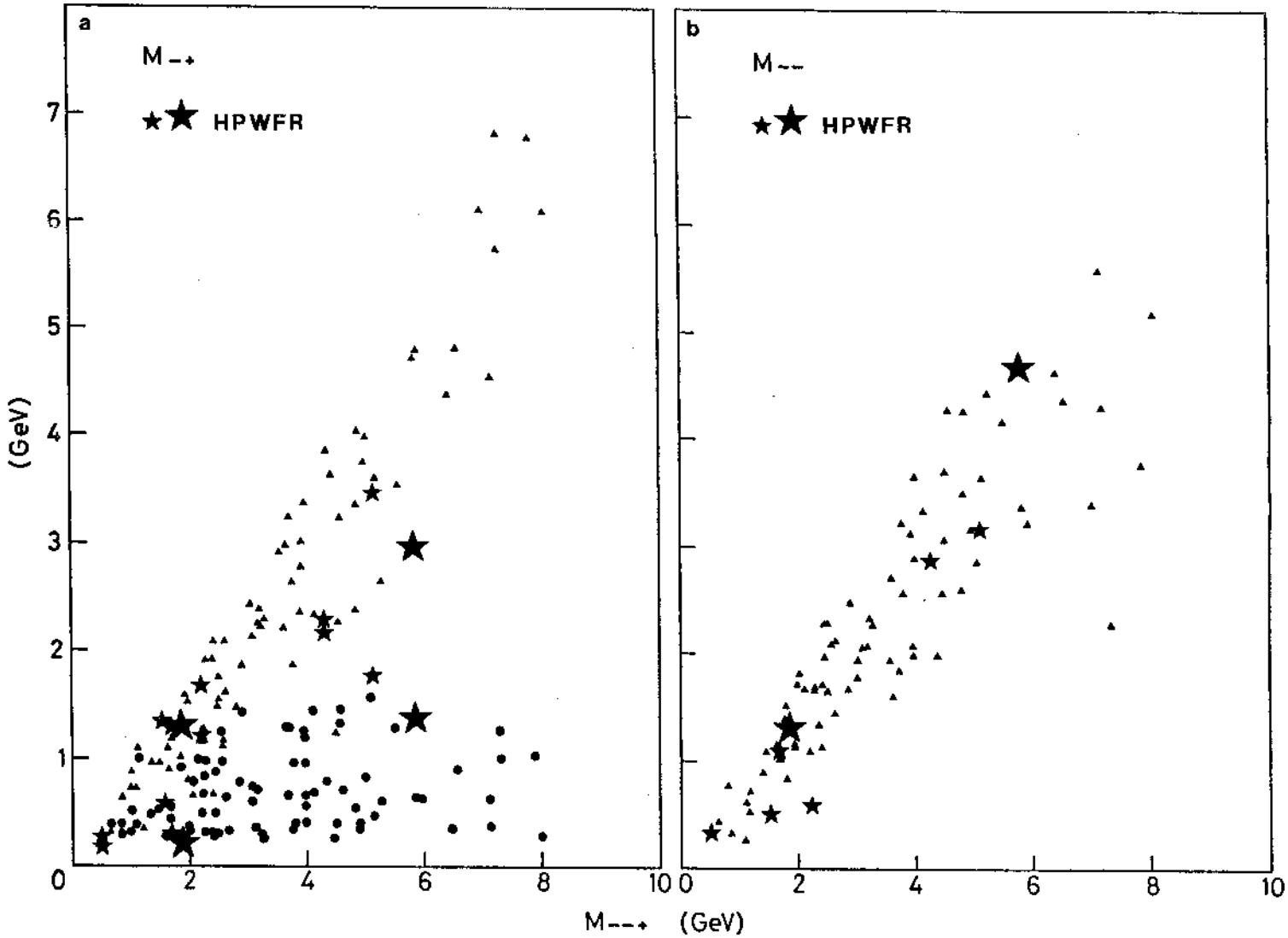

Fig. 48: Scatter plot of dimuon masses versus 3μ mass (CDHS data): a) $m(\mu_1\mu_3)$ and $m(\mu_2\mu_3)$ versus 3μ mass; b) $m(\mu_1\mu_2)$ versus 3μ-mass. The eight HPWFR events which satisfy the CDHS cuts are also shown (including the two events with unusual characteristics).

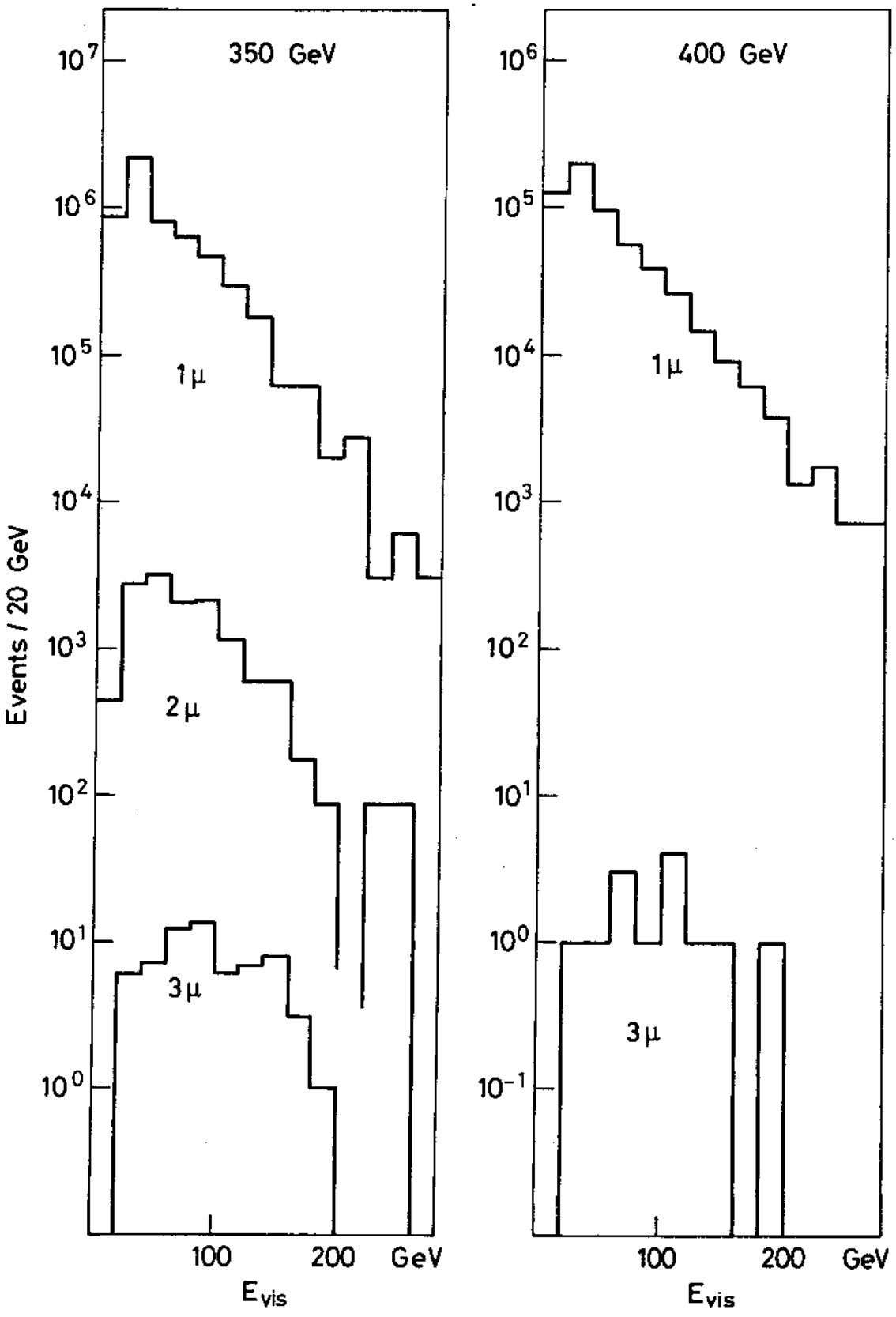

Fig. 49: Spectrum of visible energy for single-μ CC, opposite-sign 2μ and 3μ events (CDHS data).

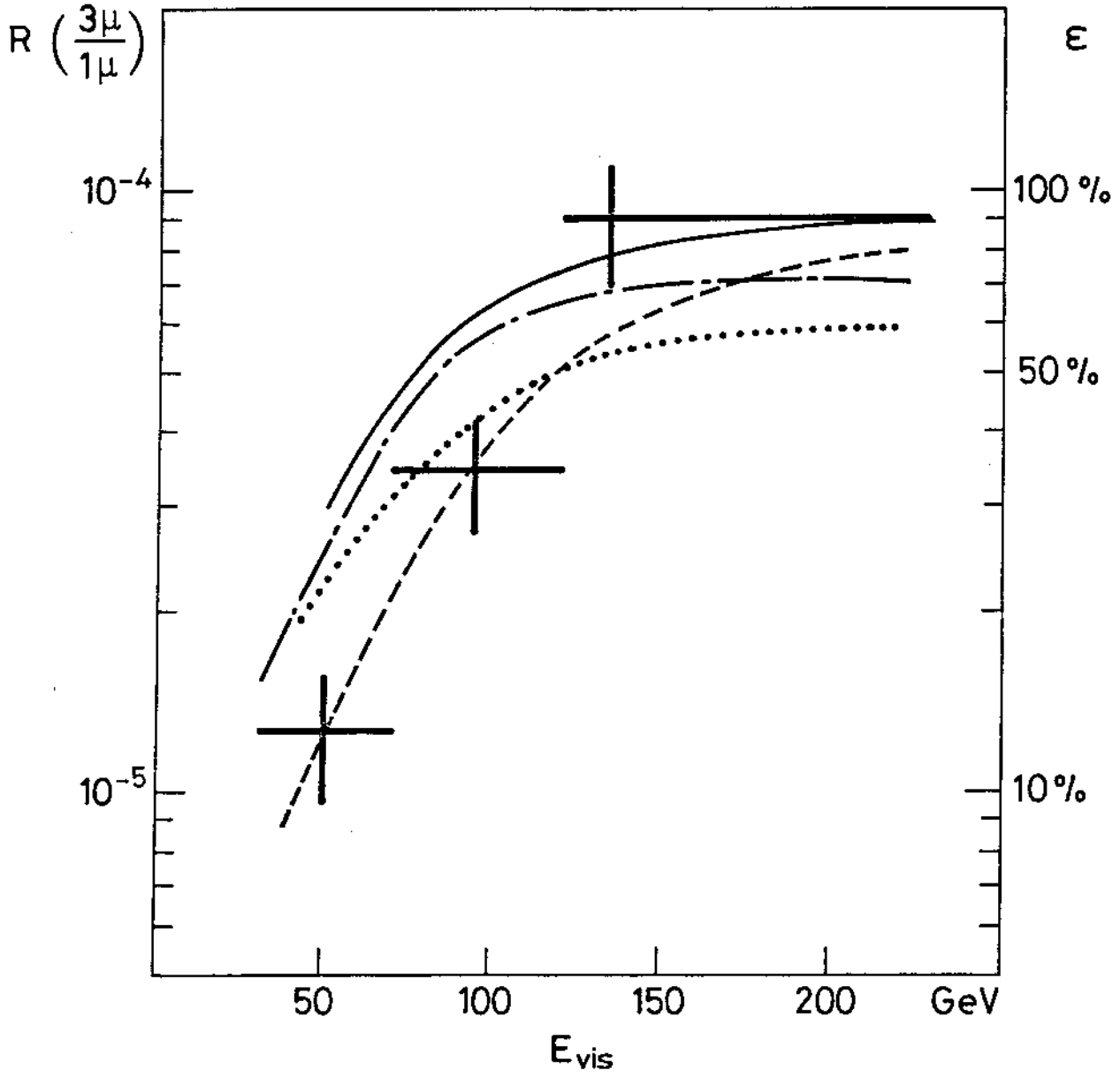

Fig. 50: 3μ rate compared to single-μ CC rate as a function of visible energy. The π(K) → μ background is subtracted. The lines give the 3μ detection efficiency for various 3μ production models (CDHS data).

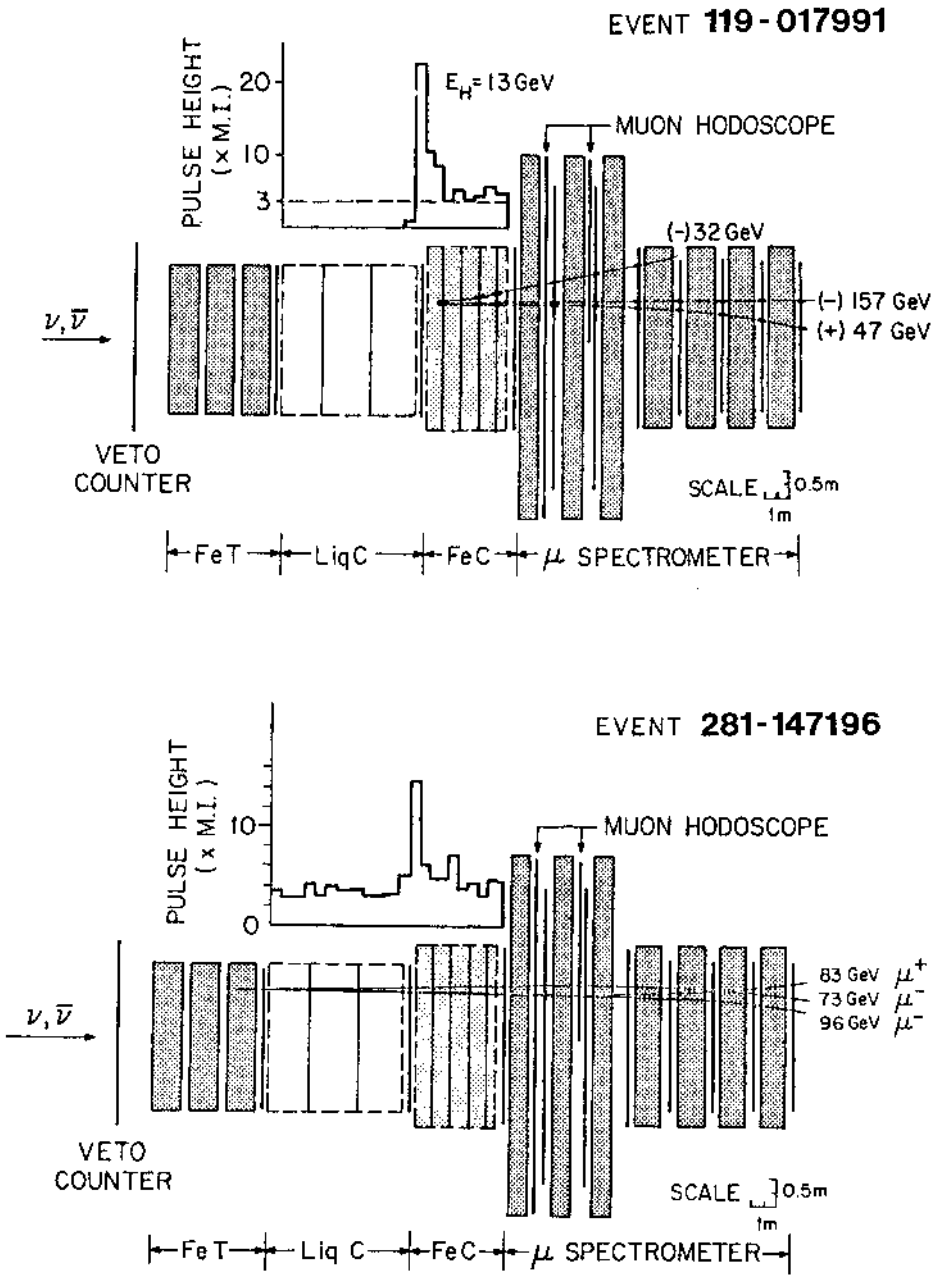

Fig. 51: Two 3μ events with unusual characteristics superimposed on the HPWFR detector.

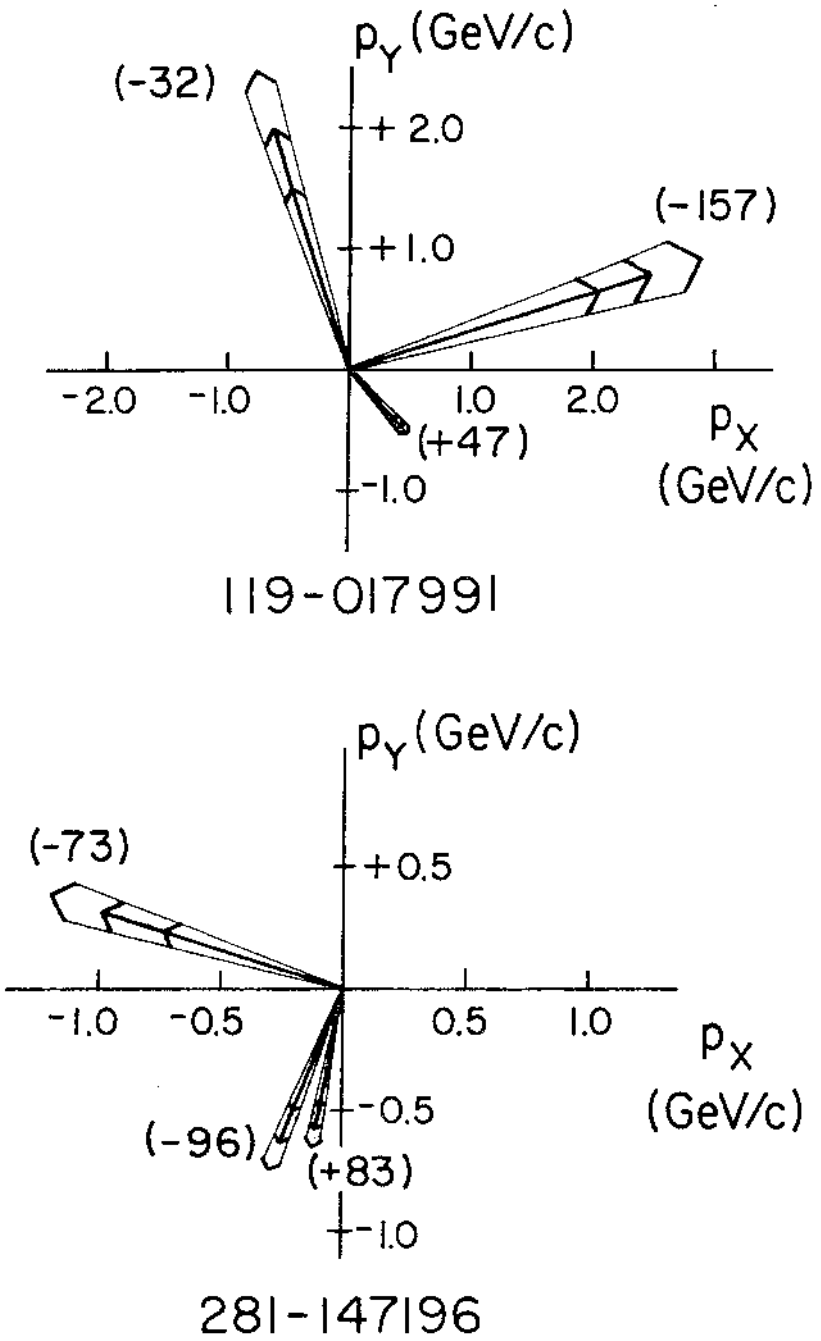

Fig. 52: Transverse momentum components of the two 3μ events shown in Fig. 51. The z-axis is along the incident neutrino direction. The dark arrow heads and central lines indicate the measured values of p_T. The shaded areas indicate the measurement errors. The numbers in parentheses are the muon charge and total momentum in GeV/c.

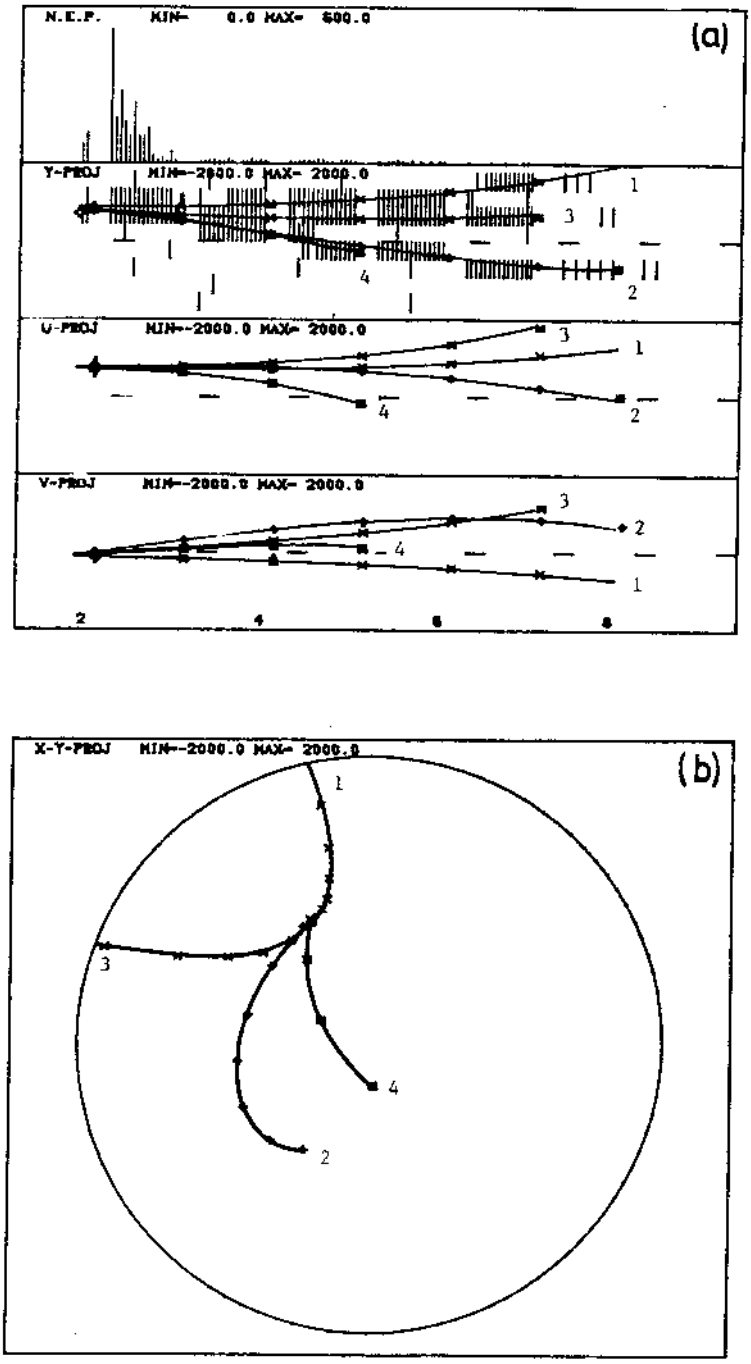

Fig. 53: 4μ event recorded by the CDHS group: a) side view, b) front view.

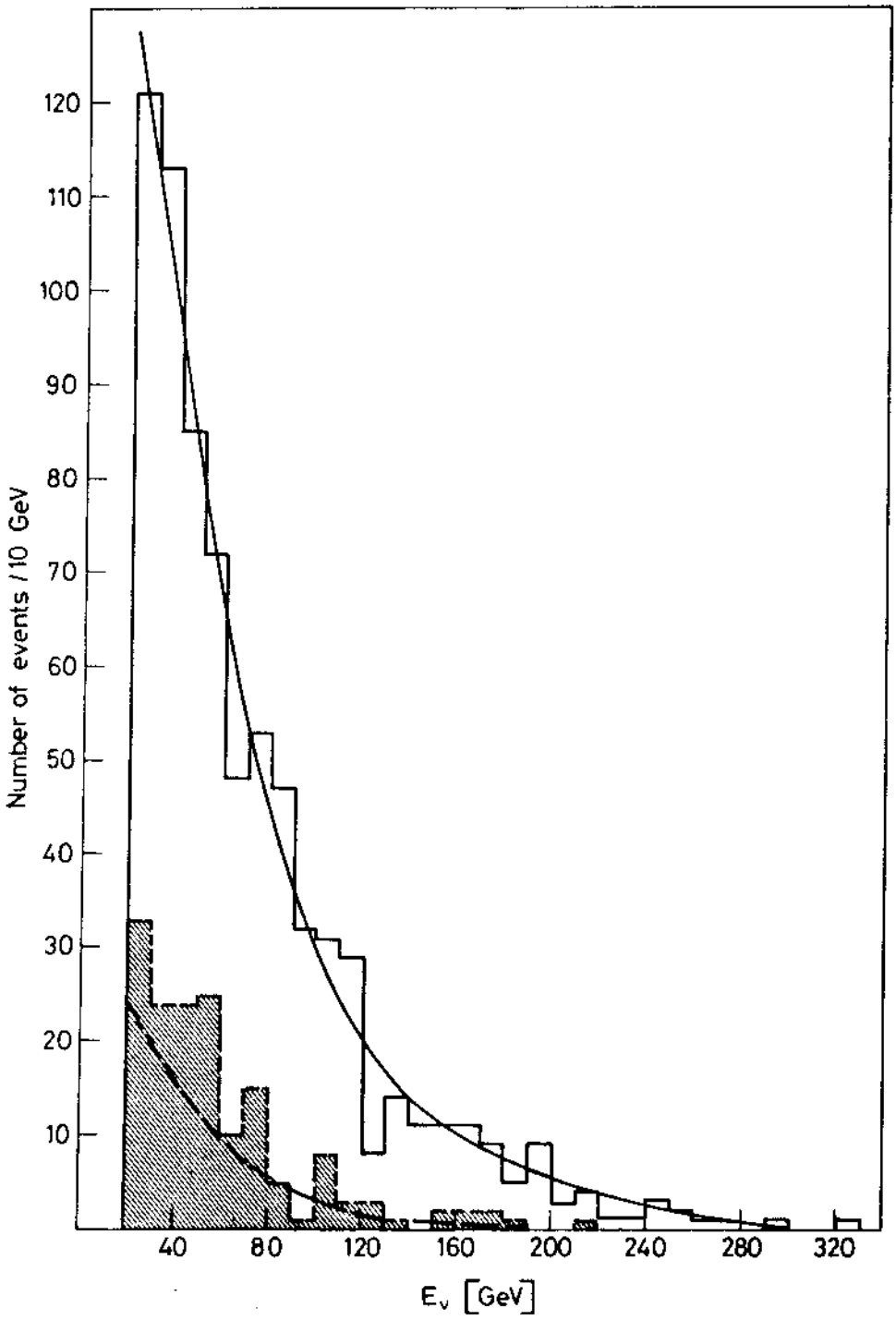

Fig. 54: Spectra of total visible energy for μ^- events (upper histogram) and μ^+ events (shaded histogram). The expectations from π and K decay are shown, normalized to the total number of μ^- events (CDHS data).